NTNU – Trondheim
Norwegian University of
Science and Technology

Dynamic Ssimulation Of Dart Anchor Installation

Daniel L Landhaug

Marine Technology (2-year)
Submission date: June 2015
Supervisor: Carl Martin Larsen, IMT
Co-supervisor: Peter Sandvik, MARINTEK

Norwegian University of Science and Technology
Department of Marine Technology

NTNU Trondheim
Norwegian University of Science and Technology
Faculty of Engineering Science and Technology
Department of MarineTechnology

M.Sc. thesis 2015

for

Daniel Landhaug

DYNAMIC SIMULATION OF DART ANCHOR INSTALLATION

Dart – or torpedo - anchors are installed by releasing the anchor unit from an installation wire at a convenient elevation above the sea bottom. The anchor unit must gain a sufficient speed to obtain a necessary penetration into the bottom, but it is also important that the installation wire has an acceptable behaviour after dropping of the anchor. If the line is long and the anchor heavy, there will be a large amount of elastic energy in the line that may lead to a tangled mass of the line after dropping the anchor. A dynamic simulation of the system is therefore needed to plan this operation for varying water depth.

The purpose of this thesis work is to simulate the free fall of the anchor including the anchor line. This is a continuation of the pre-project, where the dynamics of the lifting line after releasing the anchor was simulated. The purpose now is to find the speed of the dart anchor when hitting the sea bottom, and also the orientation of the dart.

The work may be carried out in steps as follows:

1. Literature study in addition to what was done in the pre-project. Data for needed velocity (kinetic energy) to obtain sufficient penetration should be found, and preferably also required hit angle. The penetration phase needs not to be analysed.

2. Define a case study and simulate and report results from the study.

3. Simulate cases with current in order to identify how current may influence the position of the anchor when hitting the sea floor and also orientation of the dart when hitting the sea floor.

The work may show to be more extensive than anticipated. Some topics may therefore be left out after discussion with the supervisor without any negative influence on the grading.

The candidate should in her/his report give a personal contribution to the solution of the problem formulated in this text. All assumptions and conclusions must be supported by mathematical models and/or references to physical effects in a logical manner.

The candidate should apply all available sources to find relevant literature and information on the actual problem.

The report should be well organised and give a clear presentation of the work and all conclusions. It is important that the text is well written and that tables and figures are used to support the verbal presentation. The report should be complete, but still as short as possible.

The final report must contain this text, an acknowledgement, summary, main body, conclusions and suggestions for further work, symbol list, references and appendices. All figures, tables and equations must be identified by numbers. References should be given by author name and year in the text, and presented alphabetically by name in the reference list. The report must be submitted in two copies unless otherwise has been agreed with the supervisor.

The supervisor may require that the candidate should give a written plan that describes the progress of the work after having received this text. The plan may contain a table of content for the report and also assumed use of computer resources.

From the report it should be possible to identify the work carried out by the candidate and what has been found in the available literature. It is important to give references to the original source for theories and experimental results.

The report must be signed by the candidate, include this text, appear as a paperback, and - if needed - have a separate enclosure (memory stick or DVD/ CD) with additional material.

Supervisor at NTNU is professor Carl M. Larsen

Trondheim, February 2015

Carl M. Larsen

Deadline: 10 June 2015

Abstract

Over the few last decades, numerous mooring concepts have been developed, one of these being the dart/ torpedo anchor. A torpedo anchor is shaped like an arrow and is equipped with tail fins to provide good directional and non-rotational stability. The anchor is released from a predefined height above the seabed and penetrates into the soil using the kinetic energy accumulated during free fall. Hence, no external forces are required.

This thesis presents three torpedo anchor concepts:

- Deep Penetrating Anchor (DPA)
- OMNI-Max Anchor
- Petrobras' Torpedo Anchor

However, the thesis will focus on the Deep Penetrating Anchor concept. The scope of the thesis is to simulate a torpedo anchor installation, using data for an 80tonne DPA, and perform parameter studies on the complete model.

Two models (Model 1 and Model 2) are created in RIFLEX, which is a computer program developed for analysis of flexible marine riser systems and slender marine structures. Model 1 is used to find the static equilibrium position of the anchor, that is, the position of the anchor before it is dropped. Model 2 is used to investigate the dynamic behavior of the anchor and mooring line during free fall.

In order to verify if the RIFLEX model provides realistic results, the velocity and tilt angle when the anchor hits the seabed is compared to previous experimental test results and calculations. It is found that a touchdown velocity of 26m/sec agrees with the experimental results when dropped from approximately 70m. In addition to this, all observed tilt angles are within the design criteria of 5^{o}.

The effect on the free fall velocity and tilt angle of the anchor as well as the dynamic behavior of the chain loop (mooring line) is investigated in simulations

- With and without current
- With varying distances between the two installation vessels in 500m water depth
- With decreasing vertical chain length behind the anchor

The current only affects the static equilibrium position of the anchor and can be neglected during free fall. These observations applies to all of the water depths used throughout the simulations.

With increasing distance between the vessels, the anchor velocity decreases slightly, the tilt angle remains unaltered while the free fall velocity and the amount of curls present in the chain loop (mooring line) decreases.

The vertical chain length behind the anchor is decreased incrementally from 50m to 10m. Two water depths are considered, each with two different horizontal distances between the installation vessels. The results showed that there is a relatively small influence on the touchdown velocity when varying the vertical chain length and distance between the installation vessels, while the tilt angle of the anchor increases significantly with increasing distance between installation vessels for both water depths.

One recommendation is to investigate the soil penetration phase of the anchor, perform analyses including dynamic effects in the wire due to vessel motions and investigate the lateral drag coefficient of a vertical free falling chain.

Sammendrag

I løpet av de siste tiårene er det utviklet en rekke forankringskonsepter. Et av disse konseptene er dart-/torpedoankeret. En torpedoanker er formet som en pil, og er utstyrt med halefinner for å gi god retnings og rotasjonsstabilitet. Ankeret slippes fra en forhåndsdefinert høyde over havbunnen og borer seg ned i bunnen ved hjelp av den kinetiske energien som akkumuleres under fritt fall. Ankeret trenger ingen eksterne krefter for å fullføre installasjonen.

Denne masteroppgaven presenterer de tre følgende torpedoanker-konseptene:

- Deep Penetrating Anchor (DPA)
- OMNI-Max Anchor
- Petrobras 'Torpedo Anchor

Oppgaven vil i all hovedsak fokusere Deep Penetrating Anchor konseptet. Omfanget av oppgaven er å simulere en torpedoanker installasjon ved hjelp av inputdata for et 80 tonns DPA og utføre parameterstudier på den ferdige modellen.

Det er laget to modeller (Modell 1 og Modell 2) i RIFLEX. Dette er programvare utviklet for analyse av marine fleksible stigerørsystemer og slanke marine konstruksjoner. Modell 1 er brukt til å finne den statiske likevektsposisjonen til ankeret. Det vil si posisjonen som ankeret har før det faller mot havbunnen. Modell 2 brukes til å undersøke den dynamiske oppførselen til anker og ankerline under fritt fall.

For å verifisere om RIFLEX-modellen gir realistiske resultater, så er ankerets hastighet og helningsvinkel i det ankeret treffer havbunnen sammenlignet med resultater fra tidligere beregninger og eksperimentelle tester. Den dynamiske anker modellen oppnår en hastighet på 26m/s innen det treffer havbunnen. Denne hastigheten samsvarer med målinger fra tidligere tester der ankeret er sluppet fra 70m over havbunnen. I tillegg så er helningsvinklene innenfor designkriteriet på 5^0 for alle analysene.

Effekten på ankerets frifallshastighet og helningsvinkel, samt den dynamiske oppførselen til kjetting-halvbuen (i forankringslinen) som henger ved siden av ankeret, er undersøkt i følgende simuleringer

- Med og uten strøm
- Med varierende avstander mellom de to installasjonsfartøyene for et vanndyp på 500m
- Med varierende vertikal kjettinglengde bak ankeret

Strømmen i vannet påvirker bare den statiske likevektsposisjonen til ankeret og kan derfor neglisjeres ved fritt fall. Disse observasjonene gjelder alle vanndybder brukt i simuleringene.

Med økende avstand mellom installasjonsfartøyene, minsker hastigheten som ankeret har i det det treffer havbunnen noe. Ankerets helningsvinkel forblir uendret, mens frifallhastigheten til kjetting-halvbuen og mengden av krøllede partier i denne, reduseres.

Den vertikale kjettinglenden bak ankeret reduseres stegvis fra 50m til 10m. To vanndyp (500m og 1500m) er undersøkt, og to forskjellige horisontalavstander mellom installasjonsfartøyene er betraktet for hvert av vanndypene. Resultatene viste at landingshastigheten til ankeret endres lite som følge av varierende vertikal kjettinglengde og avstand mellom installasjonsfartøyene. Helningsvinkelen øker betydelig med økende avstand mellom installasjonsfartøyene. Dette gjelder for begge vanndypene.

Forslag til videre arbeid kan være å undersøke ankeres penetrasjonsfase av havbunnen, gjennomføre analyser der dynamiske effekter i installasjonswiren fra fartøyenes bevegelser tas hensyn til, og undersøke verdien til den laterale dragkoeffisienten for i en frittfallende kjettinglenke i vann.

Preface

This report is a result of my master thesis work in marine hydrodynamics at the Department of Marine Technology at The Norwegian Institute of Science and Technology, NTNU. The master thesis has been written during the spring of 2015 and is a continuation of the project thesis written in the autumn 2014.

I find marine operations very interesting. Therefore, I wanted a topic combining my field of specialization with some marine operation. The topic was given to me by my supervisor Carl Martin Larsen in cooperation with Peter Sandvik at MARINTEK. The thesis work has given me great knowledge about torpedo anchors, how to split up and simplify a complex system and how use RILFEX for analysis of slender structures. It has been very time-consuming to create the RIFLEX tasks for the analyses.

There have been many contributors to this thesis. I would like to express my gratitude to my supervisor Carl Marin Larsen for great guidance and dedication during both the project and master thesis. I have gained a lot of knowledge during our conversations. A special thanks is also directed to Jon Tore Lieng from Deep Sea Anchors for providing me with useful and necessary information about the anchor system. I would also like to thank Kjell Larsen for great guidance about mooring systems, Arifian Agusta for RIFLEX guidance, Sigmund Søgnesand for sharing his English skills and all my friends in the office for a great year together, good discussions and motivation. I would like to thank my girlfriend Trine Holm for motivating me and all our great times together throughout this semester.

Finally, a special thanks is directed to my parents Åge and Anita Landhaug for their love and support throughout my life.

Trondheim, June 10, 2015

Daniel Litlekalsøy Landhaug

Table of Contents

List of Figures

List of Tables

Notation

Abbreviations

AHV	Anchor Handling Vessel
AHTS	Anchor Handling Tug Supply Vessel (Same as AHV)
ALS	Accidental Limit State
API	American Petroleum Instituite
COB	Center of Buoyancy
COG	Center of Gravity
CSV	Construction Support Vessel
DOF	Degree of Freedom
DNV	Det Norske Veritas
DPA	Deep Penetrating Anchor
DSV	Diving Support Vessel
FEM	Finite Element Model
FPSO	Floating Production, Storage and Offloading Vessel
MBL	Minimum Breaking load
MODU	Mobile Offshore Drilling Unit
ULS	Ultimate Limit State

The variables are described as they are used.

1 Introduction

1.1 Background and motivation

The oil and gas industry is constantly seeking new and improved solutions to maximize production in future developments and existing fields. Discoveries of easily accessible oil and gas reservoirs are becoming increasingly seldom. The current trend line is that future developments are in deeper water depths and in harsher weather conditions, which introduces several technological challenges. In order to be competitive during a period with unstable oil prices, the industry is pushed to find the best solution with respect to design and cost.

Floating units are commonly used while drilling, producing and storing hydrocarbons from offshore wells. In order to keep these floating units in a specific position, dynamic positioning systems and/or mooring are required. Over the few last decades, numerous mooring concepts have been developed, one of these being the dart/ torpedo anchor. Several companies design such anchors, and the designs varies from company to company.

Three different anchor concepts are presented in this thesis. A model of a torpedo anchor installation is then created, simulated, and run in RIFLEX, which is a computer program developed for analysis of flexible marine riser systems and marine slender structures. Simulations are conducted for varying water depths, and the behavior of the system is studied.

1.2 Scope of work

The working process can be summarized as follows:

- Literature study in addition to what was done in the pre-project
- Collect and calculate input data for the components in the torpedo anchor installation system
- Create RIFLEX models of the anchor system
- Define a case study and simulate and report results from the study
- Simulate cases with current in order to identify how current will influence the position of the anchor when hitting the sea floor and also orientation of the dart when hitting the sea floor
- Perform parameter studies using the RIFLEX models and report results

1.3 Outline of thesis

The thesis is organized as follows:

- **Chapter 2** gives a presentation of three different torpedo anchor concepts. The chapter explains how the torpedo anchors work.
- **Chapter 3** describes a torpedo anchor installation procedure. Important factors during planning are presented, and installation examples are given. It also summarizes a DPA installation performed at the Gjøa field in the North Sea.
- **Chapter 4** gives a short presentation of the computational tool RIFLEX used in the analyses, and how the program solves a nonlinear dynamic system.
- **Chapter 5** gives a description of the components in the RIFLEX model.
- **Chapter 6** describes how the two RIFLEX models are built up, how static equilibrium is found, where nodes are positioned and gives a presentation of the applied current profile.
- **Chapter 7** explains how input to the analyses are calculated in EXCEL and given to RIFLEX, and how output from RIFLEX are post-processed in EXCEL.
- **Chapter 8** describes and present results from case studies performed to check how the models are working.
- **Chapter 9, 10** and **11** presents and discuss results from parameter variations.
- **Chapter 12** gives a discussion of particular results and comment on choices made during the thesis work. Errors discovered in the calculations are also mentioned.
- **Chapter 13** summarizes the main findings and gives recommendations for further work

2 Torpedo Anchor Concepts

2.1 Deep Penetrating Anchor - DPA

This section is based on the project thesis. The following information is found in Deep Sea Anchors (2010) and Jon Tore Lieng, Tjelta, and Skaugset (2010). The Deep Penetrating Anchor is a new anchor type built on the same principle as the arrow used in the game Dart. A general description of the DPA concept is given in Jon Tore Lieng et al. (2010):

> *"The Deep Penetrating Anchor (DPA™) is an alternative anchor concept to present day solutions that offer cost saving potential in offshore mooring where soft clay seabed sediments are present…»*

The anchor is released from a convenient height above seabed and penetrates into the soil by utilizing the large kinetic energy made available during free fall. The aerodynamic shape and large weight of the anchor result in a high anchor speed during free fall. Since kinetic energy is proportional to velocity squared, the high anchor speed generates a large amount of kinetic energy as the speed increases. No external forces are acting on the anchor. It is driven by the gravitational force.

The anchor is equipped with tail fins to provide good directional and non-rotational stability. This gives a precise horizontal landing and a vertical configuration of the anchor in the soil. The anchor cannot be tilted in the soil. This reduces its loading capacity. According to Deep Sea Anchors, the horizontal accuracy is about 1.5 meters. The DPA is illustrated in Figure 2-1.

Figure 2-1: DPA - Deep Penetrating Anchor (Deep Sea Anchors, 2010).

The anchor is lowered to the determined drop position and held in place by an installation wire. This wire is shown in Figure 2-2 and Figure 2-3. The upper wire end is connected to a tugger winch or crane on board the Anchor Handling Vessel (AHV) used for the operation, while the upper end of the mooring line is held in place over the stern roller.

When the water depth increases, it is necessary to feed out more wire. A wire exposed to tension will try rotate. This is due to the torsional moment which is established by the spiral wound when the installation wire is loaded (Jon Tore Lieng, Kavli, Hove, & Tjelta, 2000). This effect becomes more significant when the wire length increases. To counteract this behavior, a swivel is inserted in the lower wire end. The anchor orientation can then be stabilized by the connection to the permanent mooring line while the wire is rotated (Jon Tore Lieng et al., 2000).

The anchor can be installed both with and without the presence of the permanent mooring line. If the anchor is to be installed in deep waters with the mooring line connected during installation, two vessels may be used. Then, one vessel is holding the installation wire and thus the weight of the anchor while the other vessel deals with the mooring line. This is the case in Figure 2-3.

If anchor installation is performed without the permanent mooring line, only one vessel is required for the operation. This is called pre-lay. The permanent mooring line is then connected to the bottom chain at a later time. This installation configuration may give a more successful

result with respect to the tilt angle since the vertical chain is not affected by any chain loop. Better verticality of the anchor will in turn lead to a higher system holding capacity. However, with this configuration it is not possible to control the behavior of the chain after the anchor has started to penetrate the seabed. The chain could get curled in the soil. Having the mooring line connected during installation, makes it is to some grade possible to control the chain behavior by shortening the length of the mooring line. This increases the axial tension. Shortening the line prevents it from lying in a pile on the seabed.

Initiation of anchor drop is conducted by a release unit. This unit is connected to the lower end of the installation wire. It detaches the wire from the mooring line. The unit is triggered by an acoustic signal from the ROV observing the operation. At this time, the anchor is free to fall towards the seabed. The release unit is described more in detail in Section 5.6.

As seen in Figure 2-3, the anchor is connected to a vertical chain segment. This is the bottom chain. The lower part of the chain dips into the ground with the anchor while the upper part lies on the seabed after installation. It is important that the chain segment is long enough to prevent the upper end from dipping into the ground when the anchor is fully penetrated. In addition, the chain must be long enough to prevent an eventual fiber insert from touching the seabed in operating condition.

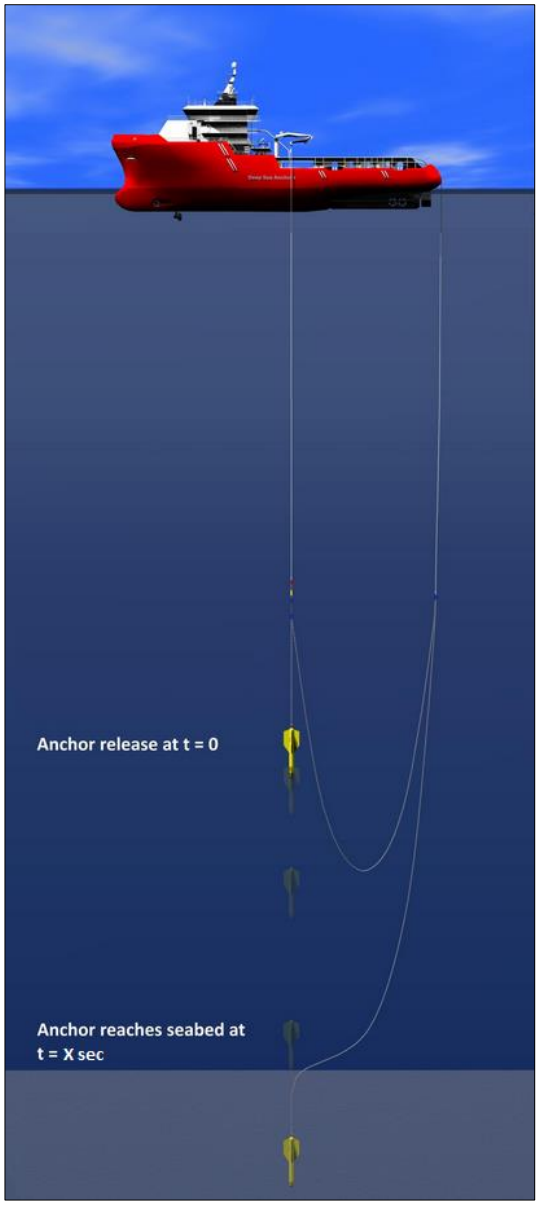

Figure 2-2: Configuration of the DPA before anchor drop (Deep Sea Anchors, 2010).

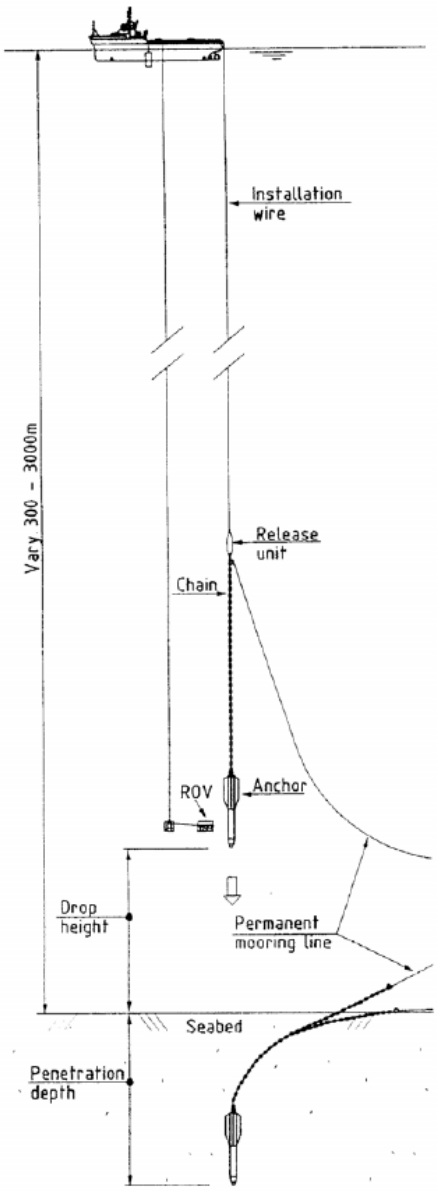

Figure 2-3: Principle of anchor drop configuration (Deep Sea Anchors, 2009).

The bottom chain may have two configurations when anchor drop is initiated. The entire length of the chain segment can be vertical as seen in Figure 2-4 a) or the vertical extension of the chain, a, can be shortened so that the mooring line loop next to the anchor partly consists of chain. This is shown in Figure 2-4 b). The bottom chain is further explained in Chapter 5.

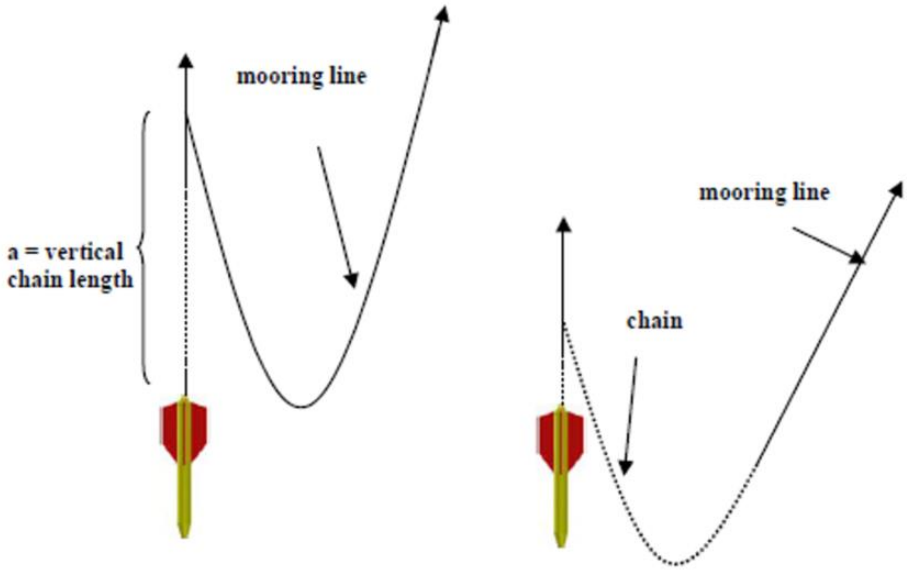

Figure 2-4: (a) Drop configuration I and (b drop configuration II (Deep Sea Anchors, 2009).

The DPA concept can be used for a wide range of water depths. It can be utilized for both deepwater (500m-1500m) and ultra-deepwater (≥1500m) (Global Perspectives Deep & Ultra-deepwater Technology & Projects Report, 2008).

2.1.1 Advantages of DPA

This section is based on the project thesis. According to Deep Sea Anchors (2010), there are several advantages with the DPA^{TM} compared to already well-established concepts. Some advantages are listed in this section.

1. Hydrodynamic forces

The small cross-section of the anchor ensures low drag forces. This is beneficial when the anchor is lowered through the splash zone. Drag forces are also significant in the calculation of anchor drop velocity and determined drop height. Low drag forces, reduces the required drop height. For the anchor to achieve the necessary seabed penetration, a certain amount of kinetic energy is required at the time instant it hits the seabed. By comparing two free falling low and high drag components, the low drag component requires less initial potential energy compared to the high drag component to achieve the same amount of kinetic energy at the time instant they hits the seabed. Hence, the component with low drag resistance can be released with a lower elevation above the seabed. It is then assumed that both components are accelerating so that terminal velocity is not achieved. Terminal velocity is explained as the highest attainable velocity for an object falling through some substance (e.g. air or water). The velocity is then of

such a magnitude so that the drag forces, which is a function of the velocity, equals the driving force (NASA, 2015).

Further, the reduced drop height increases the horizontal precision of the touch…..down point. If the anchor is tilted and falls in the direction of the tilt angle, a small drop height gives less offset compared to a larger drop height. However, the horizontal accuracy of a DPA landing is already sufficient, which was confirmed by the installation at the Gjøa field, described in Section 3.3.

2. No external energy required for installation

Gravity is the only force needed to install a Deep Penetrating anchor. It is fully driven by its own weight. Hence, the need for additional equipment and manpower is reduced. The only external equipment required is an ROV used for line observation and initiation of anchor drop.

On the contrary, during a suction anchor installation the water inside the anchor must be pumped out to create a pressure difference so that the anchor is sucked into the ground. This operation requires external energy and umbilicals to run the pump skid (D. Hagen, E. Andenæs, G. M. Korstad, & Aker Marine Contractors AS, 1998). The weight of the anchor contributes to the installation driving force but is alone not sufficient to provide desired seabed penetration.

Installation of traditional drag embedded anchors also requires external energy. These anchors are dragged into the soil by the AHV. This operation is not necessary for a Dart anchor installation. Observation by ROV is also required for a drag embedded anchor installation.

3. Greater weather window than comparable suction anchor solutions

A critical phase of a subsea installation is immersing equipment and constructions through the splash zone. A structure is in this phase generally exposed to large hydrodynamic forces such as added mass, drag and slamming forces. The larger the cross-section area, the larger the hydrodynamic forces. Hence, the small DPA cross-section gives significantly lower hydrodynamic forces than for e.g. a suction anchor there the cross section is much larger. Therefore, the dynamic motions in the splash zone are limited and installation in more harsh weather is feasible (Jon Tore Lieng et al., 2000).

4. No orientation requirements, i.e. can be loaded in any direction

The mooring line is connected to the back tip of the DPA, and the chain is free to rotate in any direction. This implies that the anchor can be loaded in any direction. The torpedo anchor in Figure 2-5 exemplifies this.

On the contrary, for a suction anchor the loading direction is limited. It can, as the DPA, withstand both horizontal and vertical forces, but the orientation of the anchor is determined. This is due to the location of the pad-eye connecting the anchor to the mooring line (see Figure 2-5). The pad-eye is located at the rotational neutral plane along the vertical side of the anchor, and must be directed towards the moored structure. The loading direction is limited to +/- 5 degrees. If the angle is larger the loading will create a moment trying to rotate and tilt the anchor. This can result in failure. This problem shows the benefit of having the mooring line connection point located at the back tip.

A traditional drag embedment anchor is designed only to withstand horizontal forces, and due to its geometry, it must be installed in the expected direction of the loading.

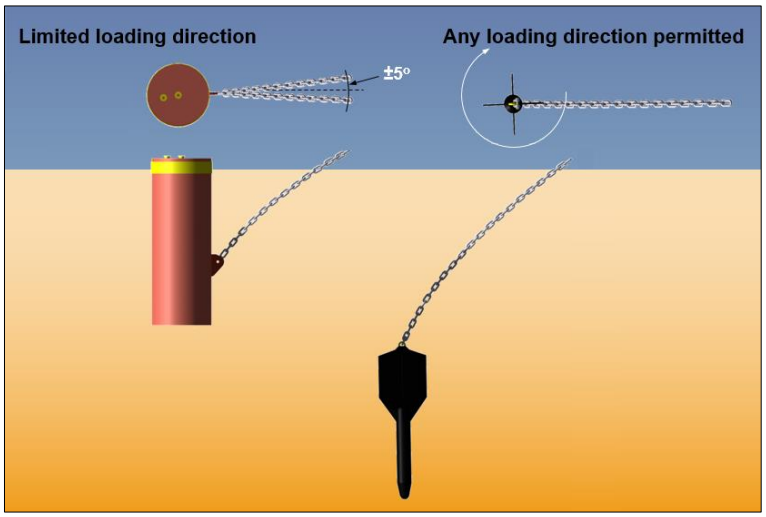

Figure 2-5: Loading direction limitation on a suction anchor (left) and a DPA (right) (Jon Tore Lieng, 2014a).

5. Precise horizontal positioning

The DPA is heavy and the center of gravity (COG) is located towards the tip. The anchor is also equipped with tail fins. The combination of these three factors gives the anchor a great directional stability during drop.

6. Quick installation

The simple installation setup makes the DPA easy to install. Installation may therefore be executed by nearly any offshore vessel by either using the moonpool, stern roller or a crane. Examples are Anchor Handling Tug Supply Vessels (AHTS), Construction Support Vessels (CSV), Crane Vessels, Diving Support Vessels (DSV) or Offshore Barges. Installation examples are explained in Section 3.2.

7. **More cost-effective with respect to fabrication and marine operations than comparable alternative solutions**

The main reasons for the DPA to be cost effective are:

- The installation procedure for a DPA is, in general, less time consuming than a suction anchor installation. In addition, the increased acceptable weather window reduces "downtime" of the DPA installation. This gives a positive effect on operational costs.
- The possibility to employ smaller vessels makes installation cheaper.
- Simple geometry makes the fabrication easier and thus less expensive compared to other systems.

8. **Applicable for taut leg mooring**

Taut leg mooring is explained more in detail in Chapter 5. The DPA can withstand both horizontal and vertical forces. In ultra-deepwater the weight of the mooring lines becomes a limiting factor (Vryhof, 2010). Taut leg mooring consisting of synthetic ropes is therefore preferred due to its significantly reduced weight. Torpedo anchors are relatively easy to install regardless of water depth and is therefore a good alternative to existing soft soil solutions for taut leg mooring in ultra-deep waters. One of the challenges with deep waters is the rubber-band-effect in the wire after anchor release. This effect is studied more in detail in the project thesis.

9. **Small footprint**

The footprint of the DPA is much smaller than comparable concepts such as suction anchors, which require a relatively large diameter in order to obtain the embedment pressure under control (Wilde, 2009).

Drag-embedded plate anchors may be used for the same purpose but only if the location and depth are not critical. Since the drag-embedded plate anchors are dragged into the soil, which leaves a large footprint, they are not suitable for fields with large amounts of subsea infrastructure (Wilde, 2009). Here, DPAs are more applicable.

2.2 OMNI-Max™ Anchor

The following information is found in Shelton (2007) and Delmar Systems Inc. (2011). After the hurricanes Ivan, Katrina and Rita in 2004 and 2005, there was a great interest in improving existing or developing new standards and technologies for mooring of Mobile Offshore Drilling Units (MODUs) in the Gulf of Mexico. Due to the requirement for improved reliability in mooring systems, the company Delmar Systems, Inc. located in Houston, Texas has developed the OMNI-Max™ Anchor concept shown in Figure 2-6. The anchor is gravity-installed just as the DPA, but geometry, size and weight are somewhat different.

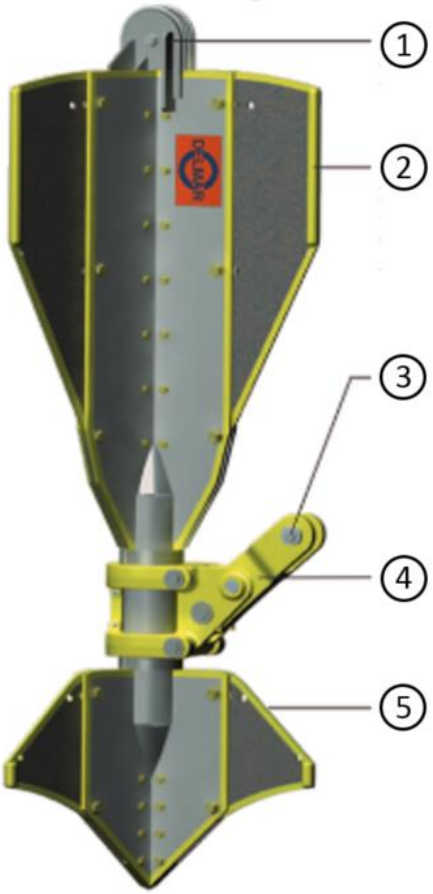

Figure 2-6: OMNI-Max Anchor (Delmar Systems Inc., 2011).

The installation/recovery wire is attached to the pad-eye placed at the top of the anchor (No. 1 in the figure). The mooring line is connected to the omni-directional mooring arm (No. 3) placed between the upper fins (No. 2) and lower fins (No. 5). The mooring arm is free to rotate 360° around the anchor axis, which makes the anchor capable of being loaded in any direction, just like the DPA. The fluke fins are adjustable in order to give optimal performance for the given soil and loading condition. They are bolted to the anchor main frame. The overall anchor

size and steel requirements are determined using Finite Element Analyses (FEA) of design loads and typical soil conditions in the Gulf of Mexico in combination with model tests.

The OMNI-Max Anchor is designed for large mooring capacity at high uplift angles in soft soil conditions just as the DPA. However, the principle of how to achieve this capacity is different. The omni-directional mooring arm is *"…strategically placed more towards the OMNI-Max tip in order to create the optimal moment-arm to generate the anchor "keying" and diving behavior as the mooring line load increases"* (Shelton, 2007). Keying is the name of a process where the anchor dive into the soil and rotates it in such a way so that it exhibit its maximum surface area normal to the loading direction (Christophe, Kien H., & Samy, 2009). This gives maximum holding capacity. The mooring arm is designed so that the mooring load is in-line with the arm for an anchor uplift angle of 40° (the angle between the load and anchor center axis). This angle is typical for normal operating tensions and conditions. For normal conditions, the size of the top and bottom fins together with the site-specific soil properties generates sufficient capacity for the anchor to remain in the vertical position. This is shown in Figure 2-7 a). When a storm arrives, the axial tension in the mooring line and the uplift angle increases (No. 1 in figure b). Then, the anchor starts to rotate towards the load until equilibrium is established. At this point, the resistance on the lower and upper fins are equal. If the storm intensifies (see Figure 2-7 c) and the capacity established in Figure b) is exceeded, the anchor will rotate further and become more perpendicular to the load (No. 3). The anchor will then start to dive deeper into the soil where the soil strength increases. It will dive until the soil strength is sufficient to generate required holding capacity (No. 2).

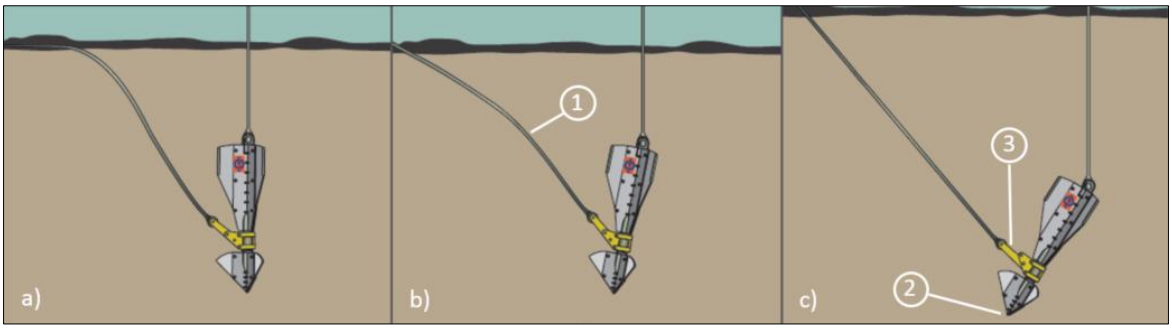

Figure 2-7: OMNI-Max Anchor behavior for increased tension (Delmar Systems Inc., 2011).

2.2.1 Advantages of OMNI-Max Anchor

The advantages of the OMNI-Max anchor and DPA are equal compared to a suction anchor. It is more interesting to look at the differences between a DPA and an OMNI-Max Anchor.

The DPA considered in this thesis is 13m in length and maximum 4m in diameter with a dry weight of 80tonnes. A corresponding OMNI-Max anchor is approximately 9.7m in length, 3m in width and height and has a dry weight of 38tonnes. "The significant difference in weight and length *"...offers logistical cost savings by allowing more anchors to fit on the AHV deck for each run to location during pre-setting operations"* (Shelton, 2007). The smaller size and less material use also makes the OMNI-Max cheaper to produce with respect to material costs compared to a DPA. However, the geometry of the OMNI-Max anchor is more complex, and complexity increases the production costs.

The OMNI-Max anchor is released from a determined drop height, which is based on predicted tip penetration. This is the same procedure as for the DPA. The difference between the two concepts is the elevation above the seabed. The OMNI-Max rigging is designed for drop heights up to 45m while the DPA must be released from >50m above mud line to achieve the terminal velocity. The DPA drop height is typically in the range 50-70 m.

"The OMNI-Max Anchor does not require the use of an A-frame for over-boarding during deployment or recovery" (Delmar Systems Inc., 2011). The use of an A-frame is necessary for DPA over-boarding over the stern roller. It is advantageous not having to install any additional equipment on the vessel used for the operation. In Figure 2-8, an over-board operation of an OMNI-Max Anchor is shown. In the right side of Figure 2-8 the fiber rope shown on the left side of the figure is tensioned.

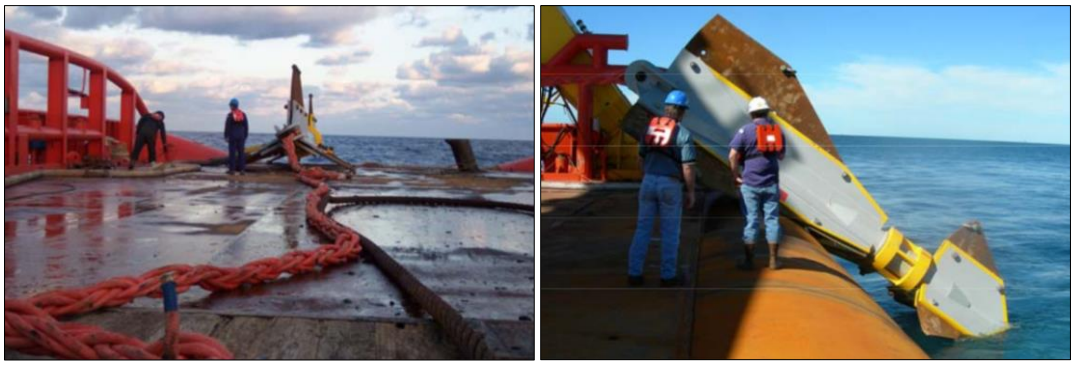

Figure 2-8: OMNI-Max Anchor Over-boarding (Shelton, 2007)

2.3 Petrobras anchor

The information presented in this section is found in Wilde (2009). The third anchor concept presented in this thesis is the Torpedo Anchor developed by Petrobras Brasileiro SA. Petrobras is a Brazilian Oil Company and one of the world's largest within its field. The company has since 1996 installed more than 1,000 torpedo piles/anchors for anchoring of deepwater flowlines and facilities of the Brazilian coast. The intention of the Torpedo anchors were to be an inexpensive, easily installed anchor for riser flowlines. The concept met their expectations and Petrobras realized that these anchors could be applicable for mooring of mobile offshore structures such as MODUs and floating production, storage and offloading vessels (FPSO). During the 1990s, taut leg mooring systems with synthetic fiber inserts started to replace the traditional chain and chain-wire mooring systems. This created a need for vertical load-capable anchors, which gave room for the Torpedo anchor. Petrobras started testing in 1999, and the concept has developed from that point.

The Torpedo anchor is suitable for the same mooring applications as DPA and OMNI-Max anchors. They work best in the same soil conditions as suction and plate anchors, which is soft to medium clay soils. The arguments for using the Torpedo anchor is an easy installation, low-cost fabrication and small footprint.

In order to get a precise landing and prevent unacceptable tilt angles after seafloor penetration, the anchor is, just as the DPA, ballasted in the front section. Lead is used near the tip, and iron cast is used in the section above the lead. If needed, a section filled with concrete may be used above the iron cast.

The shape is quite similar to the DPA. The anchor body is circular, the tip is conical and fins are inserted in the rear section. The size of the fins depends on the field of application. A small anchor needs small fins, which is just large enough to prevent the anchor from rolling on the AHV deck. Larger anchors, used for mooring of MODUs and FPSOs, are equipped with large fins.

The anchor is normally deployed over the stern roller of the AHV. The smaller anchors are typically released from >100m above the seafloor while larger anchors can be released closer to the seabed (~30 m). The height is chosen so that terminal velocity is reached before the anchor hits the seabed. This is to ensure maximum kinetic energy and therefore maximum penetration depth. This gives the highest load capacity. The penetration depth, measured between the mudline and top of the anchor, is typically 9-15 m.

The Torpedo anchor design is presented in Figure 2-9 together with the DPA. The fins on the Petrobras Torpedo anchor are extracted over a larger part of the total anchor length compared to the DPA. The cross-sectional geometry is somewhat different in the front and back tip sections.

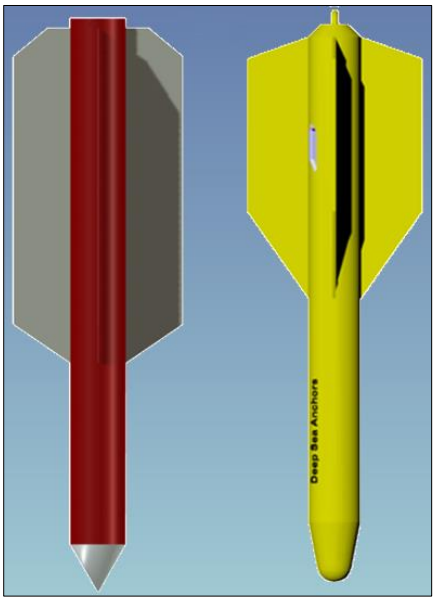

Figure 2-9: Petrobras' Torpedo Anchor (left) vs. Deep Sea Anchor's DPA (Right) (Jon Tore Lieng, 2014a).

3 DPA Installation procedure

This chapter is based on the project thesis. The installation of a DPA can be separated into two steps. First, the operation is planned in detail. Essential information must be gathered, analyses are carried out and different installation scenarios considered. When all preparations are completed, installation is executed.

3.1 Planning the Operation

The following information is found in (Deep Sea Anchors, 2009). The operational planning is divided into several parts. This section gives a brief presentation of important parameters that affects the system, what to think of during the design phase and explain the concept in general.

3.1.1 Soil investigations

Site-specific soil information is required in order to design the anchor system. These data are obtained from a soil investigation. Samples of the soil are gathered from several borings at the location and tested in laboratories. Based on these tests, it is possible to determine soil characteristics, which is further used to model of the real soil condition. The tests can determine whether the ground is soft, medium or hard, and the composition of e.g. clay, gravel, rock, etc. Based on the soil characteristics, together with anchor geometry and kinetic energy, it is possible to estimate the penetration depth of the anchor. The anchor tip penetration must be larger in a soft soil in order to obtain the same holding capacity as for an anchor in a harder soil. The undrained shear strength, S_u of the soil is one of the most important parameters for this calculation. S_u represents the shear strength of intact clay. The parameter is used for penetration and anchor capacity analyses described in the following sub-sections. The parameter will not be discussed more in detail.

3.1.2 Chain Loads at Seabed

To ensure that maximum loading conditions of the system are not exceeded, it is required to calculate of maximum design forces in the system. A mooring system is designed to withstand different loading conditions, as described in standards developed by e.g. Det Norske Veritas (DNV) and American Petroleum Institute (API). The two most severe loading conditions are the ultimate limit state (ULS) and accidental limit state (ALS). The ultimate limit state corresponds to the maximum load carrying resistance. Designing for ULS, will ensure that the system has adequate strength to withstand load effects imposed by extreme environmental

actions (DNV, 2013b). The accidental limit state corresponds to "…*damage to components due to an accidental event or operational failure*" (DNV, 2004). Designing for this limit state will ensure that the system has adequate capacity – redundancy- even after some failure in the structure.

The characteristic loads (maximum loads) for a DPA system design in the two loading states mentioned above may be found using a DNV standard named *Design of Offshore Steel Structures*, DNV OS-C101, (DNV, 2004). New revisions of the DNV standards are updated when required. The standard mentioned above was used for the design of the two anchors installed at the Gjøa field in the North Sea, explained in Section 3.3. Later, updated revisions of this standard have been made available.

A common requirement for mooring lines is to have a certain length of chain resting on the sea floor at all times. For mooring lines connected to drag embedded anchors this is an absolute requirement. For mooring systems using DPAs, it is also quite favourable. To have a chain resting on the seabed at all times ensures a minimum of vertical forces on the DPA. This is due to the horizontal chain configuration before it dips down towards the anchor. Another positive effect is the friction force acting along the chain. The submerged chain weight multiplied with the friction coefficient and length of horizontal chain on the seabed presents a friction force between the chain and soil. This friction force reduces the tension on the anchor when the moored structure is moving and pulls the mooring line. A typical value of the friction coefficient is $\mu = 0.5$. The length of chain resting at the sea bottom is calculated by catenary equations using the characteristic loads explained above. If the anchor is to be used for taut leg mooring it is important to keep the vertical load component at a reasonable level so that the anchor is not dragged out of the soil.

"During normal operation the mooring lines will be pre-tensioned…" (Deep Sea Anchors, 2009). Hence, it is necessary to calculate how large pre-tension the system can withstand before the design criteria are exceeded. On the contrary, a sufficiently high pre-tension can be used as input and the anchor system is designed accordingly.

3.1.3 Anchor velocity during drop phase

A sufficient seabed penetration is needed to achieve the required holding capacity. The anchor tip penetration depends on the amount of kinetic energy the anchor has gained at the time instant it hits the ground, in addition to soil parameters such undrained shear strength explained in Section 3.1.1. The kinetic energy attained during free fall depends on drop height, anchor

weight, anchor geometry (pressure resistance), drag forces, tension in the mooring line and friction forces between the anchor surface and the surrounding water. The kinetic energy is proportional to velocity squared. Based on these relations and dependencies, the vertical force balance on the anchor may be expressed as

$$m\ddot{z} = mg - D - B - T \tag{3-1}$$

where m is the submerged mass, $\ddot{z}$ is the vertical acceleration (positive downwards), g is the gravitational acceleration, D is the drag force, B is the buoyancy and T is the friction force on the anchor line. The drag force D consist of pressure and friction drag. Formulas for each component can be found in (Deep Sea Anchors, 2009). Figure 3-1 shows the selected coordinate system and definitions of the force components in equation (3-1).

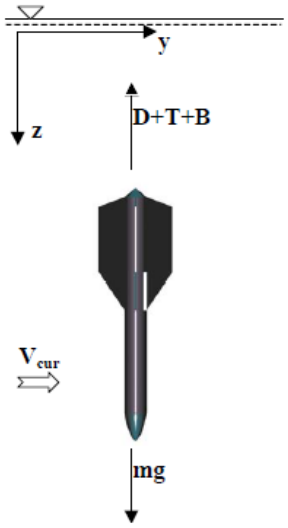

Figure 3-1: Coordinate system and definition of forces acting on the anchor (Deep Sea Anchors, 2009).

Based on the force equilibrium given in Equation (3-1) it is possible to compute the touchdown velocity as a function of drop height.

3.1.4 Anchor Penetration

As already mentioned, calculation of anchor penetration is important for determining the holding capacity of the system. The anchor penetration can be determined by using a finite element approach based on a method first formulated by True (1975). The method was used to determine the seabed undrained shear strength by analyzing soil failure around a penetrometer. A penetrometer used for seabed soil investigation is a torpedo-shaped vehicle that is dropped into the soil in the same way as a DPA.

The analysis model is based on force equilibrium on an advancing anchor. This equilibrium equation can be expressed as

$$M \cdot a = W - B - F_{BE} - F_{AD} - F_H \quad (3\text{-}2)$$

where

M = Anchor mass
a = Acceleration
W = Weight of anchor in air
B = Anchor buoyancy
FBE = Bearing component force
FAD = Side adhesion force
FH = Fluid drag force

The bearing component force and the inertial side adhesion force includes soil strength parameters. The adhesion force accounts for the reduced side resistance due to separation or reduced contact force on the sides of the anchor as it penetrates down in into the seabed. The fluid drag force F_H is calculated with the standard expression for a hydrodynamic force given in Equation (3-3). A more detailed description of the components in (3-2) can be found in Deep Sea Anchors (2009).

$$F_H = \frac{1}{2}\rho C_D A_f v^2 \quad (3\text{-}3)$$

ρ is the density of the surrounding fluid, C_D is the drag coefficient, A_f is the area and v is the anchor velocity.

The anchor penetration is controlled by the strength characteristics of the soil (Jon Tore Lieng et al., 2010). The soil model in the finite element model (FEM) are described by parameters such as soil undrained shear strength, soil sensitivity, wall adhesion factor, soil weight density, deformation parameters and friction angle. Values for these parameters are found during a soil investigation. A full list and formulas are given in (Deep Sea Anchors, 2009).

3.1.5 Chain embedment

To calculate the horizontal and vertical anchor capacity, it is necessary to know how the soil affects the chain segment going from the dipdown point to the anchor. The chain configuration inside the soil is calculated in addition to the chain tension at the anchor point. To make this calculation accurate, the chain is divided into a series of finite elements. The chain element is assumed to be a curved bar element with zero bending stiffness. The characteristic loads (ULS and ALS) in addition to the pre-tension are used in the calculation. An average undrained shear

strength profile is typically applied. Figure 3-2 gives an example of typical output from such an analysis. The figure shows required chain length from the dipdown point to the anchor as a function of the penetration depth and applied load. If the load acting on the chain is higher than the soil resistance around the chain, it will cut through the soil and its configuration changes. In Figure 3-2, it can be seen that the ULS condition is the critical one, requiring a chain length of approximately 90 meters. The bottom chain segment must have a sufficient length to guarantee the fiber from dipping into the ground. This is because fiber ropes, which often is the next segment of the mooring line, shall in general never be in contact with the seabed. Sand, mud and rocks can wear out the fiber rope, and result in line failure.

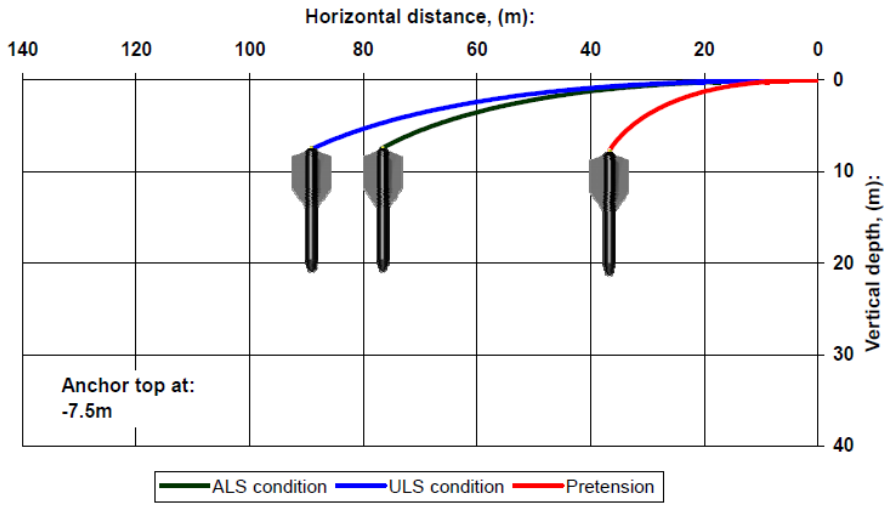

Figure 3-2: Required chain length from dipdown point to anchor. Average undrained shear strength profile is applied (Deep Sea Anchors, 2009).

3.1.6 Static- Vertical and Horizontal Anchor Capacity

Since the DPA design is quite similar to piles, the pullout capacity (vertical capacity) may be determined in the same manner as for tension loaded piles. Both static short-term capacity and static long-term capacity is calculated. API has created a recommended practice which can be used for estimation of the static vertical- and horizontal short-term capacity (API, 1993).

The static short-term horizontal capacity is determined by "the ultimate soil resistance". This parameter depends on the soils type of failure mode. For a fully submerged anchor, the failure mode will be that the soil is moving around the anchor as the horizontal force is pulling it sideways. In this calculation, it is important to remember that the DPA geometry is not a pure cylindrical pile. The upper half of the DPA is equipped with flukes. Hence, the geometry in this region can be considered to have a rough square cross-section. This is shown in Figure 3-3. Depending on the load direction (green arrow), the cross-section area varies. To be on the

conservative side, the smallest cross-section area is chosen. This will be the cross-section of the anchor seen from the direction of where the green arrow. According to the Geotechnical Design report from the installation at Gjøa, the upper part of the anchor alone, considered as a rough square, increases the ultimate capacity of approximately 20% due to the additional resistance at the side walls.

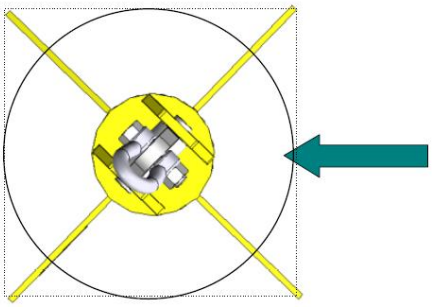

Figure 3-3: Top-view of the DPA (Deep Sea Anchors, 2009).

The holding capacity of the anchor increases for a certain time after the anchor is installed. This is called consolidation time. The safety factor of the system is proportional to the holding capacity, and will therefore also increase. A brief explanation of this is the following. When the anchor penetrates the seabed, the intact clay is remolded. The shear forces between the anchor wall and the surrounding clay are therefore decreased. During the consolidation phase, these shear forces will again increase as the density of the clay which is compressed toward the anchor wall increases. After the consolidation, the full undrained shear strength is regained. Due to the consolidation effect, the anchor should not be loaded to the ultimate strength before the consolidation is complete. For the Installation at Gjøa, the anchors were estimated to attain 90% of their maximum pullout capacity after approximately 30 weeks, and 90% of the horizontal capacity was attained after less than 20 weeks.

The static long term vertical capacity can be estimated based on Janbu's method (Janbu, 1973). The intention is to design the anchors for a long service life, and it is therefore important to know how large loads the system is able to resist in the long term. Important forces determining this capacity is the soil friction resistance and the submerged weight of the anchor.

The long-term horizontal response must also be calculated. This is probably the most important factor. The calculation is based on a procedure by Grande, (Grande, 1976). The horizontal displacement and rotation of the anchor is calculated for different soil profiles, penetration depths and tension loads.

3.2 Installation

There are several installation methods available for the torpedo anchors. As mentioned, they can be installed both with and without the permanent mooring line. One or two ships can be utilized, and the lines can be pre-laid or connected directly to the floating unit. The anchors can be lowered into the water through the vessels moonpool (Figure 3-4), deployed over the stern roller (Figure 3-5), immersed by a winch in the ships side (Figure 3-6) or by a crane. At Gjøa, the anchors were installed using the moonpool. DPA installation over the stern roller is typically conducted in combination with a stern mounted A-frame. This is shown in Figure 3-5.

Figure 3-4: DPA lifted through a moonpool (Deep Sea Anchors & Statoil, 2009).

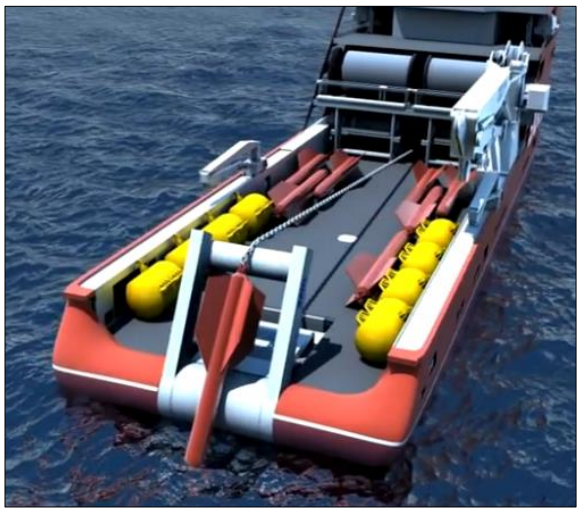

Figure 3-5: DPA entering the water by use of stern mounted A-frame and skidding winches (Deep Sea Anchors, 2010).

3.2.1 DPA installation – Example 1

Example 1 gives a step by step procedure for a DPA installation using the tugger winch, stern mounted A-frame and the vessel crane. The anchor is here installed with only one vessel.

Installation procedure:

1. Move DPA to the vessel's stern. Top end is pointing towards tugger winch
2. Connect one en of mooring chain to bearing on DPA, and the other end to the tugger winch
3. Lift stern mounted A-frame and feed out chain from the winch. Anchor will slide over stern roller into the water. Lower the A- frame when entire DPA is in the water
4. Feed out wanted length of bottom chain (vertical chain segment in drop configuration (see Figure 2-3)
5. Connect lower end of release unit to mooring chain

6. Connect upper end of release unit to installation wire on tugger winch
7. Connect upper end of bottom chain to crane wire
8. Rotate crane sideways until the top end of mooring chain hangs freely over starboard or port side of the vessel.
9. Lower anchor to desired drop height by feeding out installation wire and crane wire holding the mooring chain
10. Inspect mooring line and anchor with ROV. Is configuration as expected?
11. If yes: ROV sends out acoustic signal that opens the release unit
12. Inspect chain at seabed with ROV. All ok?
13. If yes: Installation is complete

The bottom chain is then connected to a buoy, for later pickup and connection to the permanent mooring line. If the anchor is installed with the permanent mooring line, it is preferable to have it stored on another vessel (Jon Tore Lieng et al., 2000).

3.2.2 DPA installation – Example 2

Anchor installation can also be conducted using the offshore vessel Type 183 MV "Lone", shown in Figure 3-6. This ship is owned by SAL Heavy Lift, a company specializing in sea transport of heavy lift and project cargo (SAL Heavy Lift, 2014). The installation technique described in this section is based on the promotion video made by SAL Heavy Lift (2013). The vessel is designed for anchor installation up to 2,000m depth.

The anchors are stored in a rack in order to save space, and the vessel can handle up to 44 penetration anchors with all associated equipment such as chain, fiber segment and buoyancy modules. MV "Lone" is equipped with two heavy lift 1000 metric ton cranes, and two winches for lowering the anchor and mooring line to the designated drop height above the seabed. The numbered items in the figure are explained in Table 3-1.

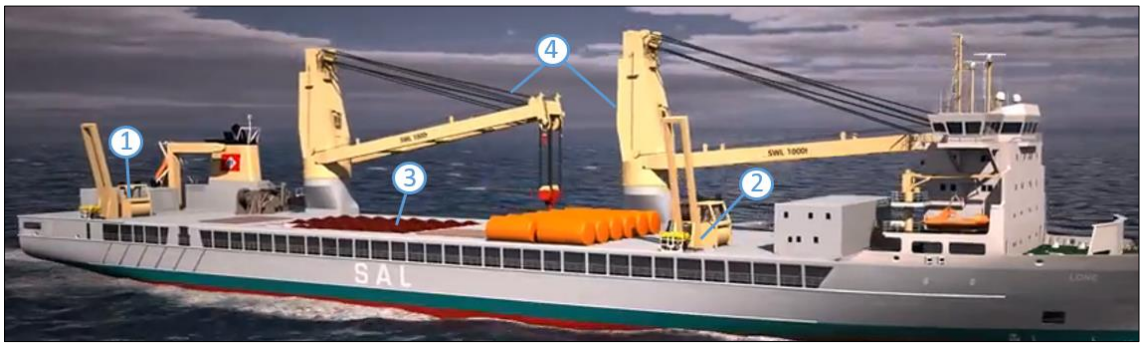

Figure 3-6: Heavy lift MV "Lone" equipped for DPA installation (SAL Heavy Lift, 2013).

Table 3-1: Explanation of Numbered Items in Figure 3-6.

Number	Component
1	Aft Winch
2	Fore Winch
3	Rack stowage of anchors
4	Cranes fore and aft

With this installation method, the bottom chain consists of two segments. This is done to simplify the installation. The Installation wire is fed out from aft winch and fiber rope from the fore winch.

Installation procedure:

1. Activate DP system to ensure exact working position.
2. Connect aft crane to the first bottom chain segment.
3. Connect chain segment to anchor stored in the rack.
4. Lift anchor off the rack and temporary store it at hang-off point near the aft winch
5. Connect wire from aft winch to the upper end of first chain segment. The hang-off point is now carrying the load.
6. Feed out a certain length of permanent fiber rope from fore winch and fasten it to the side-rail on the vessel.
7. Pick up second bottom chain segment and connect upper end to fiber rope on vessel rail.
8. Transfer load from the rail to the crane by releasing fiber rope from the rail.
9. Move chain and fiber rope to hang-off position
10. Connect lower end of second chain segment to upper end of lower chain segment
11. Transfer load from hang-off point to winch by releasing the chain from hang-off point and feed out wire from the crane until the anchor is hanging right beneath aft winch. The anchor is now hanging freely in the water from the aft winch.
12. Lower the anchor to designated drop height, and feed out fiber rope from fore winch.
13. Inspect mooring line and anchor. Is configuration as expected?
14. If yes: Open release unit with acoustic signal from ROV
15. Inspect chain at seabed with ROV. All ok?
16. If yes: Installation is complete

3.2.3 Measurement of installation parameters

It is important to collect logged data between the time of anchor release and the point where seabed penetration is completed (zero anchor velocity). The data of interest is anchor position, tilt angle, touchdown velocity, terminal velocity (if it is achived) and penetration depth. These data are essential to determine whether the installation was successful or not. As mentioned, the penetration depth must be sufficient to obtain required holding capacity, and the tilt angle cannot be more than five degrees.

The essential data are obtained by a measuring device (bottle) mounted in the rear end on the outside of the anchor. The small bottle is recovered by the ROV after completed seabed penetration. A thin wire is laid from the bottle to the seabed surface along the chain segment behind the anchor. The ROV hooks up the retrieval wire from the AHV with the bottle wire. The bottle is dragged out of the soil and hoisted to the surface by the winch on board the vessel. The operation is shown in Figure 3-7.

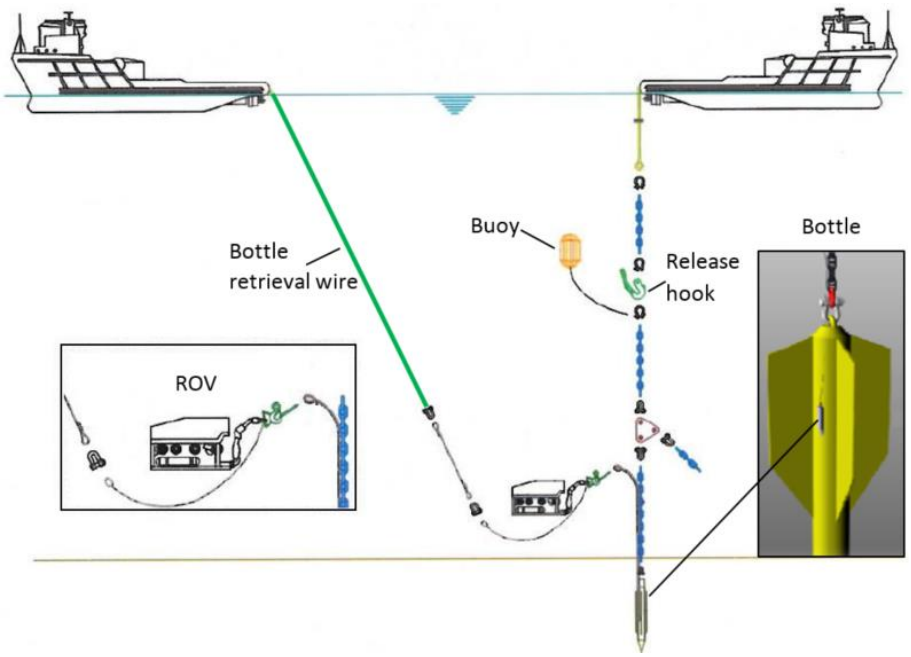

Figure 3-7: Retrieval of instrumentation on DPA. (Jon Tore Lieng et al., 2010) and (Hasselø & Petrobras, 2005).

3.2.4 OMNI-Max Anchor Installation Procedure

The procedure is found in Delmar Systems Inc. (2011). The installation procedure can be separated into six steps. The steps are visualized in Figure 3-8. It should be noted that the figures are not to scale.

1. Anchor is lowered into the water over the stern roller on AHF. The bottom part of the permanent mooring line hangs freely in the water.
2. ROV is launched to inspect the rigging when the anchor is in the water.
3. Anchor is lowered over the proposed touchdown position of the male subsea connector stand. ROV verifies the water depth and re-inspect the rigging.
4. AHV pays out wire and lower the rigging until subsea connector stand lies on the seabed (at proposed touchdown position). AHV moves towards the proposed anchor drop location while the ROV observes the mooring line, which is laid out on the seabed. This step allows for pre-alignment of the mooring arm.
5. AHV finishes wire pay-out, position itself at the drop location and adjust the vertical position of the anchor to the determined drop height. ROV verifies that the mooring arm has correct orientation, then verifies the drop height. Hereafter, ROV observes release hook from a safe distance. Anchor drop coordinates are recorded from the surface position. ROV sends out an acoustic signal, which opens the release hook. Anchor is then free to fall.
6. ROV verifies anchor penetration depth, by inspecting depth markings provided on the part of installation/retrieval wire that follows the anchor into the soil. The anchor is now successfully installed and ready for attachment to the permanent mooring line and floating unit.

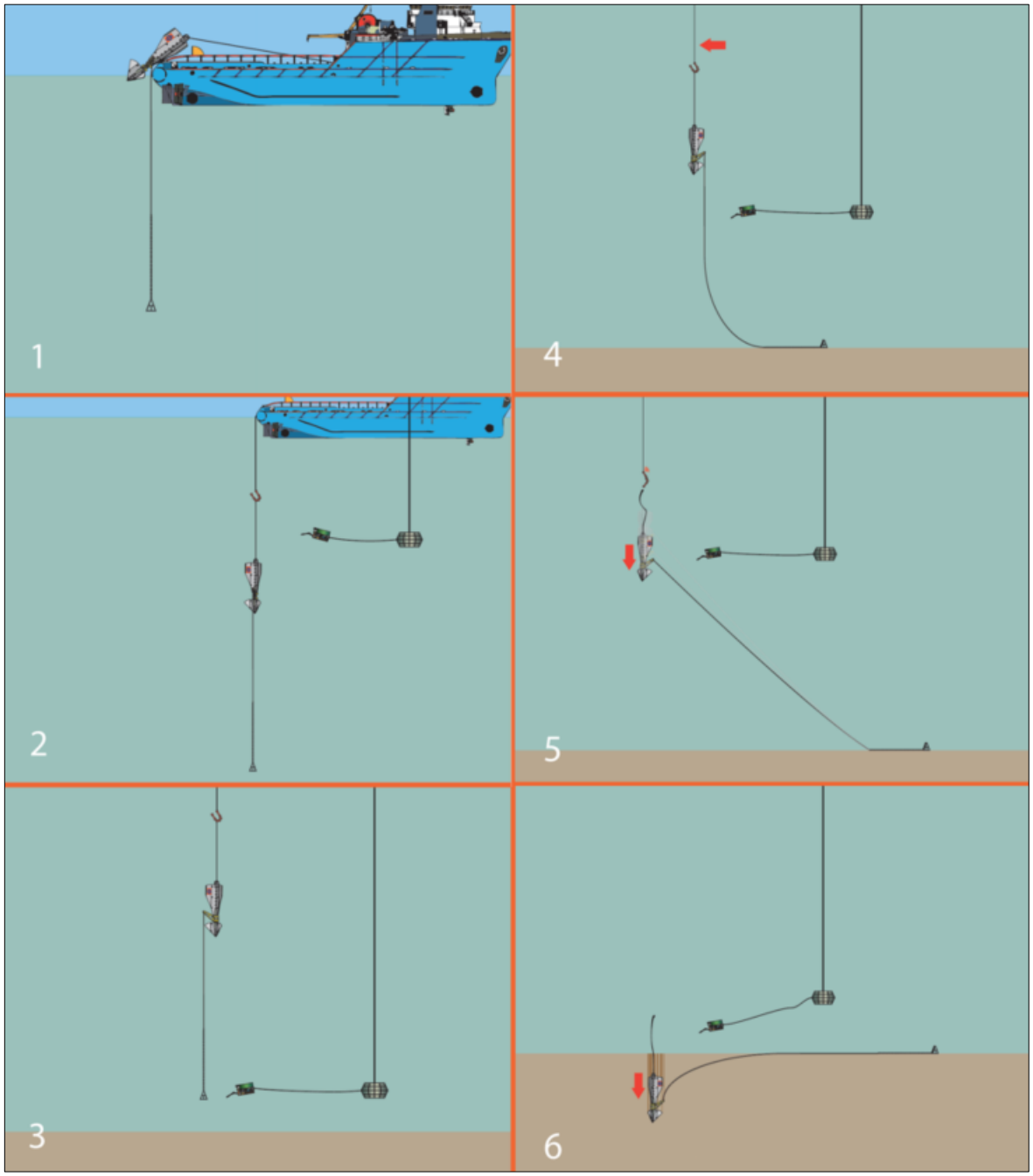

Figure 3-8: Installation of an OMNI-Max Anchor (Delmar Systems Inc., 2011).

3.3 DPA Installation at the Gjøa Field

The following information is found in Jon Tore Lieng et al. (2010) and Deep Sea Anchors (2009). The development of the DPA started with promising results from initial theoretical investigations. Therefore, model testing in the scale 1:25 were conducted. The results from this test were good. Thereafter, testing in the Trondheimsfjord (2003) and at the Troll field (2008) were performed with anchors in the 1:3 scale, and as a last concept verification, two full size Deep Penetrating Anchors were installed at the Gjøa field in the North Sea off the West coast of Norway in the middle of August 2009.

The main goal of this project was *"…to demonstrate to the industry that the practical application of the DPA technology is a viable alternative to today's anchoring solutions*" (Jon Tore Lieng et al., 2010). The two anchors are presented in Figure 3-9. They had a dry weight of approximately 80tonnes, were 13m in length, had a shaft diameter of 1.2m and was equipped with four meters wide tail fins (max diameter). The anchors were designed for a pull-out capacity of 700tonnes, which was more than required for the drilling rig present at that time. In this way, the anchors could be used for a larger rig at a later time. The water depth at the location was 360 meters. If the project turned out to be successful, the DPA system would be qualified as an alternative to existing anchoring solutions used in areas with soft clay seabed sediments.

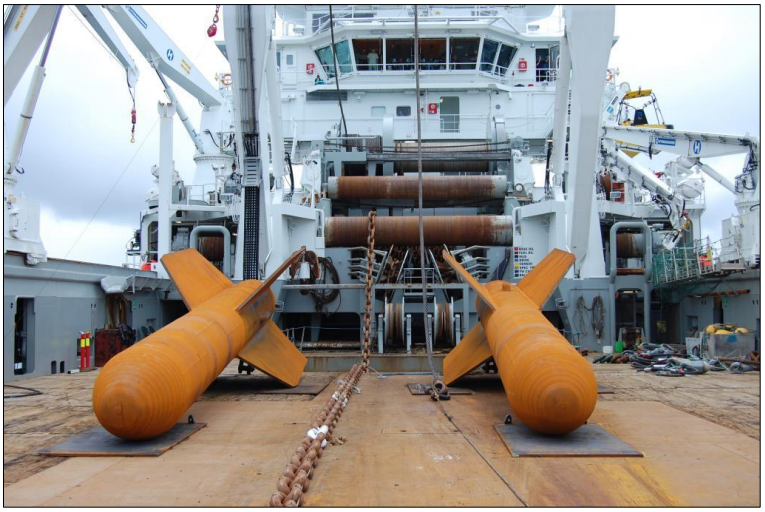

Figure 3-9: Full-scale 75tonne DPAs on board the AHF M/SEC Island Vanguard (Deep Sea Anchors, 2010).

The anchors were installed with a tilt angle of less than two degrees, and the success criterion was maximum five degrees. The horizontal offset relative to the release point was within a two-meter radius for both anchors. This confirmed that DPA installations could be repeated with high precision.

A geotechnical analysis of the soil sediment showed variation in the soil conditions for the two installation locations. The pullout capacity of the anchor is dependent on the soil conditions at the specific location. As mentioned in Section 3.1.1, the softer the soil, the larger tip penetration is needed to achieve the same pullout capacity. Therefore, different anchor tip penetrations for the two anchors were required. Assuming a touchdown velocity of 25m/sec, the tip penetrations for the two respective soil conditions were calculated to 20.5m and 25.5m. These values were obtained from an in-house software tool.

The anchors were dropped from approximately 50m and 75m. After installation, the results showed an actual tip penetration of 24.5m and 31 mm, respectively. The anchors reached a velocity of 24.5m/sec and 27m/sec at the time instant they hit the seabed. This indicated good agreement between predicted and acquired anchor velocity and penetration, with predicted penetration on the conservative side.

It was concluded that anchor installation was successfully executed with respect to tilt angle, horizontal accuracy and tip penetration depth. The DPA concept was after this installation awarded with a certificate of Proven in Principle by DNV.

4 Computational Tools

This chapter is based on the project thesis. This chapter gives a brief presentation of the software used for analyses conducted in this thesis. The software SIMA/RIFLEX is used. A more detailed software description can be found in the SIMA and RIFLEX "User Guide" (MARINTEK, 2014d) and "RIFLEX theory manual" (MARINTEK, 2014a).

4.1 SIMA

SIMA is a simulation and analysis tool for marine operations and floating systems (MARINTEK, 2014c). It can be used in all steps of the analysis – from modeling to results. The software is built on nonlinear time domain analysis which makes it able to deal with advanced structures and operations.

SIMA is developed in co-operation between MARINTEK and Statoil. The motivation for developing this computer program was the need for a simulator so that marine operations could be investigated and trained on before they were executed. This could provide important information to e.g. quality assurance, feasibility evaluation, improve HSE performance, give familiarization to participants in the marine operation and what-if analysis (Statoil & Moxnes, 2011).

SIMA is the graphical interface for the two computer programs RIFLEX and SIMO. SIMO is used to analyze motions and station keeping of multibody systems. In this thesis, vessel motions are not considered, and the surface nodes are therefore assumed to be fixed. The focus is solely on RIFLEX calculations.

4.2 RIFLEX

All information in this section is found in the RIFLEX Theory Manual (MARINTEK, 2014a). The computer program is described as:

> *"RIFLEX is a computer program for static and dynamic analysis of flexible risers and other slender structures, such as mooring lines, fish cage systems, pipelines, umbilicals and also conventional steel risers"* (MARINTEK, 2014a).

The program consist of five modules which are able to communicate internally by the file system. These modules are presented in Figure 4-1 and the following text.

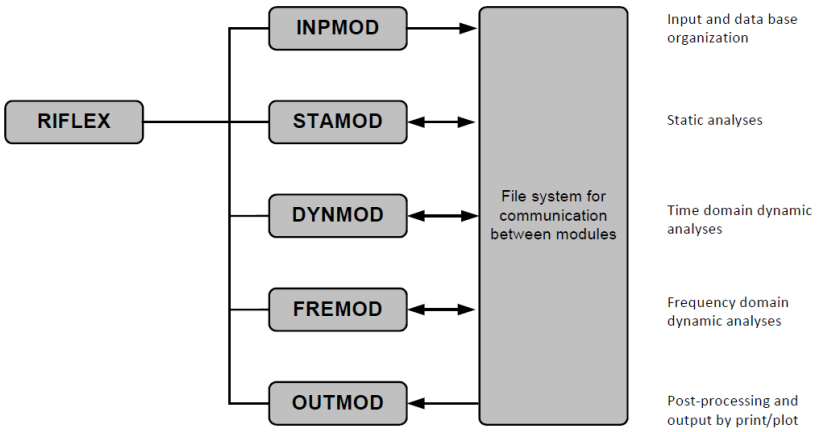

Figure 4-1: The structure of RIFLEX (MARINTEK, 2014a).

- **INPMOD** reads the input data and organizes them in a database for use by the other modules during the analyses. When this module has been run, the database is created, and it is not necessary to rerun it for every new analysis performed by the other modules.
- **STAMOD** performs a static analysis of the system and finds the static configuration. In the context of this report, STAMOD is used to find the position of the connection point between the installation wire and mooring line when all forces are applied. This static configuration corresponds to the initial configuration for the following dynamic analysis. STAMOD also generates the element mesh, the stressfree configuration and key data for the finite element analysis based on the input to INPMOD.
- **DYNMOD** conducts the time domain analyses based on the static configuration found in STAMOD, environmental data and motion data applied as forced displacements in the analysis. Dynamic response of the system is found after a succeeded run. Several dynamic analyses can be conducted without rerunning INPMOD and STAMOD. The output from DYNMOD is stored for further post-processing by the modules OUTMOD and PLOMOD. In addition to the dynamic response, natural frequencies and corresponding mode shapes can be calculated. The nonlinear time domain analysis used in RIFLEX is explained further in Section 4.3 and 4.4.
- **FREMOD** calculates the dynamic response in the frequency domain. This module is not used in this report.

- **OUTMOD** performs post-processing of selected results generated by STAMOD and DYNMOD. Plots can be stored in a separate file for graphic output in the PLOMOD module. It is also possible to export time series via a standardized file format for further post-processing in a statistical analysis program (STARTIMES).
- **PLOMOD** is not included in Figure 4-1. This module can be seen as a part of OUTMOD. The module gives a graphic presentation of the plots generated by OUTMOD. Animation of the dynamic behavior of the complete system is also available.

4.3 Nonlinear Dynamic Systems in general

This section is based on the project thesis. It gives a brief presentation of the nonlinear dynamic analysis applied in RIFLEX. A motivation for using nonlinear analysis is that according to Rama Rao (2014) "*A nonlinear analysis is needed if the loading produces significant changes in the stiffness*". This will be the case here.

The dynamic equilibrium equation for a multi-degree-of-freedom system can, in general, be written as

$$\boldsymbol{M}\ddot{\boldsymbol{x}} + \boldsymbol{C}\dot{\boldsymbol{x}} + \boldsymbol{K}\boldsymbol{x} = \boldsymbol{Q}(\boldsymbol{t}) \qquad (4\text{-}1)$$

where, $\boldsymbol{M}$ is the total mass matrix of the system, $\boldsymbol{C}$ is the damping matrix, $\boldsymbol{K}$ is the stiffness matrix and $\boldsymbol{Q}(\boldsymbol{t})$ is the external load vector. $\ddot{\boldsymbol{x}}$ is the acceleration vector, $\dot{\boldsymbol{x}}$ is the velocity vector, $\boldsymbol{x}$ is the displacement and/or rotation vector of the structure, depending on the degree of freedom considered, and $\boldsymbol{t}$ is the time. The solution of equation (4-1) can be given in time or frequency domain. Solving the dynamic motion equation in the frequency domain is only possible for a linear system, and is particularly useful for structures with a frequency-dependent mass, damping or stiffness matrix, or for a system with non-viscous damping (Langen & Sigbjörnsson, 1979). If the external load is a direct function of time, the natural option is to solve the equation in the time domain. This is the case in this thesis.

The real world is complex. It is not built on linear relations and is certainly not stationary. To describe a system in a realistic manner, nonlinear effects must, in many cases be taken into account.

The general dynamic equilibrium equation (4-1) can be written as

$$\boldsymbol{R}^I(\boldsymbol{r}, \ddot{\boldsymbol{r}}, \boldsymbol{t}) + \boldsymbol{R}^D(\boldsymbol{r}, \dot{\boldsymbol{r}}, \boldsymbol{t}) + \boldsymbol{R}^S(\boldsymbol{r}, \boldsymbol{t}) = \boldsymbol{R}^E(\boldsymbol{r}, \dot{\boldsymbol{r}}, \boldsymbol{t}) \qquad (4\text{-}2)$$

where $\boldsymbol{R}^I$, $\boldsymbol{R}^D$, $\boldsymbol{R}^S$ and are the inertia-, damping- and internal structural reaction force vectors. $\boldsymbol{R}^E$ is the external load vector, and $\boldsymbol{r}$, $\dot{\boldsymbol{r}}$, $\ddot{\boldsymbol{r}}$ and $\boldsymbol{t}$ are the structural displacement-, velocity-, acceleration- and time vectors.

The two main reasons for the differential equation (4-2) to be nonlinear is displacement dependencies in the inertia and damping forces, and coupling effect between external forces and structural displacement and velocity. There is also be a nonlinear relationship between internal forces and displacements (MARINTEK, 2014a).

According to Langen and Sigbjörnsson (1979), the most important nonlinear properties within structural engineering are divided into three main categories;

- Geometric nonlinearities
- Nonlinear material properties
- Nonlinear effects due to interaction between the structure and environment

The first category, geometric nonlinearities, is often related to large displacements and rotations. In addition, a stiffness nonlinearity directly connected to the axial tension in the structure is included in this category. Since the system degrees of freedom (DOFs) can be large, the geometry of the structure may change significantly.

The nonlinear material properties are often caused by elastic-plastic behavior which implies that stresses and strains are outside the elastic region. Hence, Hooke's law is invalid. For elastic-plastic materials, the strength is no longer a linear function of the applied loading.

The last category is fairly complex. An example of nonlinear effects between the structure and the environment is induced drag damping which occurs when a structure moves in water. As a result of the abovementioned nonlinearities, the mass, damping and stiffness matrices can change with time (Langen & Sigbjörnsson, 1979).

4.4 Solution of a Nonlinear Dynamic system

The following information is found in Langen and Sigbjörnsson (1979) and MARINTEK (2014a). Nonlinear systems can be solved with analytical (semi-analytical) and numerical methods. The numerical solving methods are based on stepwise integration. RIFLEX uses stepwise integration in the time domain. Hence, a brief explanation of this method is given.

By utilizing stepwise integration, the nonlinearities can be described properly. A drawback of this method is the large time consumption since the mass-, damping- and stiffness- matrices are updated at each time step, and the error is minimized with iteration.

The stepwise numerical integration of the dynamic equilibrium equation is based on the Newmark β-family and the Wilson θ-method, where the time step is constant through the whole analysis.

On incremental form, the dynamic equilibrium (4-2), can be written as

$$(\boldsymbol{R}^I_{t+\Delta t} - \boldsymbol{R}^I_t) + (\boldsymbol{R}^D_{t+\Delta t} - \boldsymbol{R}^D_t) + (\boldsymbol{R}^S_{t+\Delta t} - \boldsymbol{R}^S_t) = (\boldsymbol{R}^{\boldsymbol{E}}_{t+\Delta t} - \boldsymbol{R}^S_t) \tag{4-3}$$

In Equation (4-3), dynamic equilibrium is considered at two time steps a short time interval Δt apart. The increment in external loading is balanced by the increment in inertia-, damping- and structural reaction forces. To find a solution, the nonlinear equation must be linearized. Tangential mass-, damping- and stiffness matrices are introduced, with values gathered at the start of each time increment. This gives the following linearized incremental motion equation.

$$\boldsymbol{M}_t \Delta \ddot{\boldsymbol{r}}_t + \boldsymbol{C}_t \Delta \dot{\boldsymbol{r}}_t + \boldsymbol{K}_t \Delta \boldsymbol{r}_t = \Delta \boldsymbol{R}^E_t \tag{4-4}$$

where $\Delta \ddot{\boldsymbol{r}}_t$, $\Delta \dot{\boldsymbol{r}}_t$, $\Delta \boldsymbol{r}_t$ and $\Delta \boldsymbol{R}^E_t$ are the incremental acceleration-, velocity-, displacement- and external force vectors, respectively. The terms in the equation are defined as

$$\begin{aligned} \Delta \boldsymbol{r}_t &= \Delta \boldsymbol{r}_{t+\Delta t} - r_t \\ \Delta \dot{\boldsymbol{r}}_t &= \dot{\boldsymbol{r}}_{t+\Delta t} - \dot{r}_t \\ \Delta \ddot{\boldsymbol{r}}_t &= \ddot{\boldsymbol{r}}_{t+\Delta t} - \dot{r}_t \\ \Delta \boldsymbol{R}^E_t &= \boldsymbol{R}^E_{t+\Delta t} - \boldsymbol{R}^E_t \end{aligned} \tag{4-5}$$

A residual force vector $\delta \boldsymbol{R}^E_t$ is introduced as dynamic equilibrium is not satisfied at the end of the time step $t_k + \Delta t$ (k is the step number). This is a result of the nonlinear effects, and the fact that the tangential values are gathered at the start of the increment. The residual vector due to change in mass, damping and stiffness over the time step is given as

$$\delta \boldsymbol{R}^E_t = \boldsymbol{R}^{\boldsymbol{E}}_{t+\Delta t} - (\boldsymbol{R}^{\boldsymbol{I}}_{t+\Delta t} + \boldsymbol{R}^{\boldsymbol{D}}_{t+\Delta t} + \boldsymbol{R}^{\boldsymbol{S}}_{t+\Delta t}) \tag{4-6}$$

The residual force vector is added to the next time step. This is done to prevent error accumulation in the system. It will act as a correction. By inserting the residual force vector into Equation (4-4), the motion equation can then be written as

$$\boldsymbol{M}_t \Delta \ddot{\boldsymbol{r}}_t + \boldsymbol{C}_t \Delta \dot{\boldsymbol{r}}_t + \boldsymbol{K}_t \Delta \boldsymbol{r}_t = \Delta \boldsymbol{R}^E_{t+\Delta t} - (\boldsymbol{R}^{\boldsymbol{I}}_t + \boldsymbol{R}^{\boldsymbol{D}}_t + \boldsymbol{R}^{\boldsymbol{S}}_t) \tag{4-7}$$

The effect of the equilibrium correction is visualized in Figure 4-2. The Incremental method without equilibrium correction (Euler's method) is presented in the left figure and the error reduction as a result of equilibrium correction is shown in the right figure.

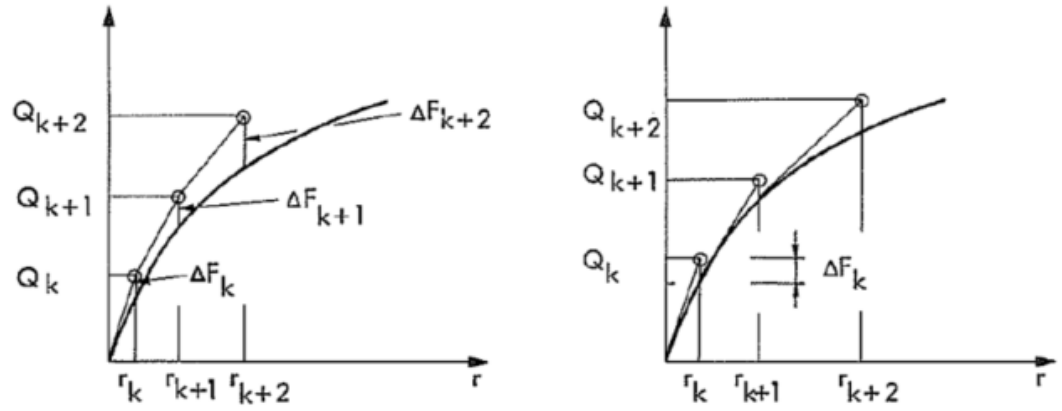

Figure 4-2: Comparison of Incremental method without equilibrium correction (left) and with eq. correction (right).

To find equilibrium between internal and external forces at the end of a time step, one must iterate on the error. In the applied iteration approach, tangential mass-, damping- and stiffness matrices are recalculated for each iteration cycle. This is called the Newton-Raphson iteration procedure (see Figure 4-2). This iteration makes the error as small as possible. In a slender system such as the one considered in this thesis, the global geometry experiences large changes during drop. This affects the mass-, damping- and stiffness matrices, due to the large variation in node positions. In addition, a lumped mass formulation cannot be utilized for a system submerged in water, since the added mass is anisotropic, meaning that it depends on the direction of the displacement (C. M. Larsen, 2015). Figure 4-3 illustrates the basic concept of an integrated load and equilibrium iteration, by visualizing how the iteration develops for two iteration steps. In a nonlinear analysis, the external force $\boldsymbol{R}$ (red line), likewise the internal forces $\boldsymbol{Kr}$ (blue line), is a function of the displacement $\boldsymbol{r}$. The slope of the tangent (green lines) represents the linear stiffness. The cross-over between the red and blue line is the equilibrium point. The iteration keeps the load at each time step on the right track as long as the time step is sufficiently small to provide a good starting point for the iteration.

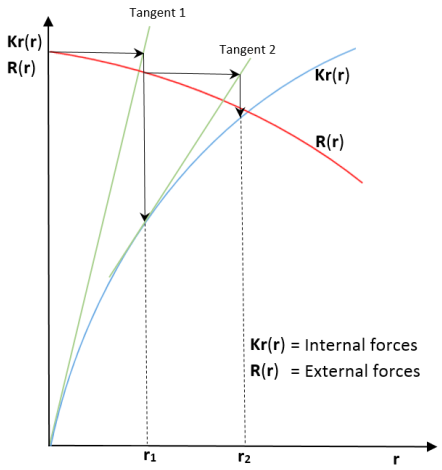

Figure 4-3: Integrated load and equilibrium iteration. Newton –Raphson method. (Larsen, 2014a).

A more detailed version of the solution procedure can be found in the "RIFLEX Theory manual" (MARINTEK, 2014a), and an even more comprehensive explanation can be found in Langen and Sigbjörnsson (1979).

5 Mooring system

The primary function of a mooring system is to keep the moored structure in position. This is to ensure that risers, umbilicals and subsea equipment are protected from damage (Kai-tung Ma et al., 2013). A large drift off may rip off risers and umbilicals which could lead to costly repairs and/or pollution of the environment if hydrocarbons are released.

5.1 Catenary vs. Taut Leg Mooring System

The following information is mainly found in dredgingengineering.com (2015) and Rigzone.com (2015). Catenary mooring becomes less efficient and less economical as the water depth increases, and in deep to ultra-deep waters the weight of the mooring line becomes a limiting factor. As a result, it not possible to use a pure chain catenary system, because the large weight of the lines gives a significant reduction in the payload of the moored structure. In worst case, the line can fail. To avoid these problems, synthetic fiber ropes are inserted into a portion of the lines. This reduces the submerged weight of the mooring line.

A catenary system and a taut leg system is shown in Figure 5-1. Taut leg mooring is often used in deep waters. Here, the lines arrive the seabed at an angle, while in a catenary system the lines arrives the seabed horizontally. In this way, the anchor must be able to withstand both horizontal and vertical forces in a taut leg mooring system, while it must only resist only horizontal forces in a catenary system.

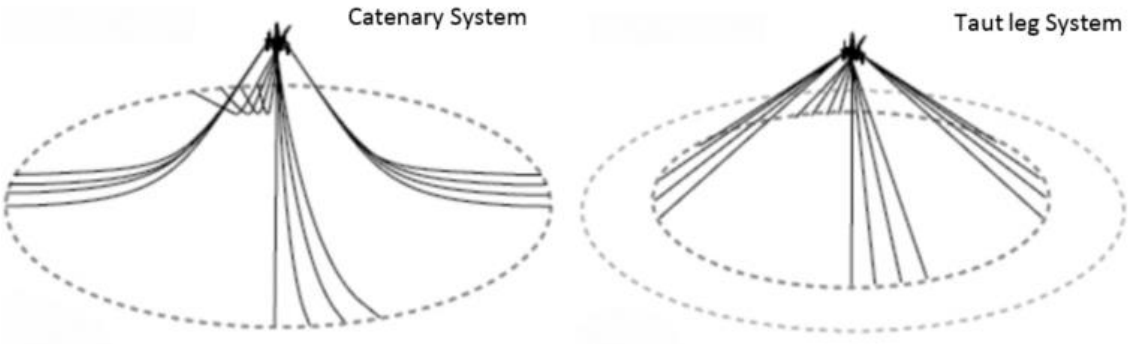

Figure 5-1: Catenary vs. taut leg mooring (dredgingengineering.com, 2015).

Taut leg mooring systems have several advantages compared to catenary systems. It can be seen in Figure 5-1 how the footprint of the taut leg system is significantly smaller due to the shorter lines. Therefore, this system is beneficial to use in locations where space is limited or special concerns must be accounted for due to subsea infrastructures such as modules, pipelines

and other mooring lines (Wilde, 2009). The loads are also better distributed between adjacent lines, which improves the efficiency of the system. The vertical load component on the vessel from the mooring system is much lower. This reduces the mooring system's impact on vessel payload (Wilde, 2009). The fiber inserts in a taut leg system give a much more elastic mooring system. The author has chosen to design the mooring lines for a taut leg mooring system.

Mooring lines can consist of one segment type or a combination of two or more different types. It can be pure chain or some combination of chain, fiber rope and wire. The configuration depends on water depth, and if the mooring line is crossing over pipelines on the seabed, subsea modules or other mooring lines. A mooring line is usually defined from the bottom end (anchor) to top end (moored structure). In deep water mooring, it is common to use three main segments. The first segment is the bottom chain, the second is a synthetic fiber rope and the upper part is chain or wire, depending on what the floating structure is equipped with. The reason for inserting a chain segment in the lower end of the mooring line is the good abrasion resistant properties of a steel chain (Kai-tung Ma et al., 2013). The touchdown point changes as the mooring line configuration varies between slacked and stretched due to the vessel motions. Therefore, it is necessary to use a material that can withstand continuous lift off, touchdown and dragging along the seabed.

According to K. Larsen (2015) the line lengths for a taut leg mooring system can be found as a function of the water depth. In Figure 5-2 the principle of a taut leg line and its governing parameters are shown. The angle between the seabed and the taut mooring line often ranges from 30^0- 45^0 (Rigzone.com, 2015). 45^0 is used in this thesis. When the water depth is known, it is straightforward to calculate the length of the hypotenuse, which approximately can be set equal to the total length of the mooring line. Regardless of the water depth, the bottom chain segment can be set to 150m (K. Larsen, 2015). At the upper end, the chain segment is set to 50m. The upper chain segment is often a part of the rig's own chain. This segment is therefore omitted in the RIFLEX model. The length of the fiber insert is found by subtracting the 200 meters of chain from the length of the hypotenuse. The expression for the fiber insert length is given in Equation (5-1). The bottom chain (150m) is assumed to go from the seabed and up towards the rig when calculating the fiber lengths.

$$L_{fiber} = \frac{h}{\sin 45^{\circ}} - 200\ [m] \tag{5-1}$$

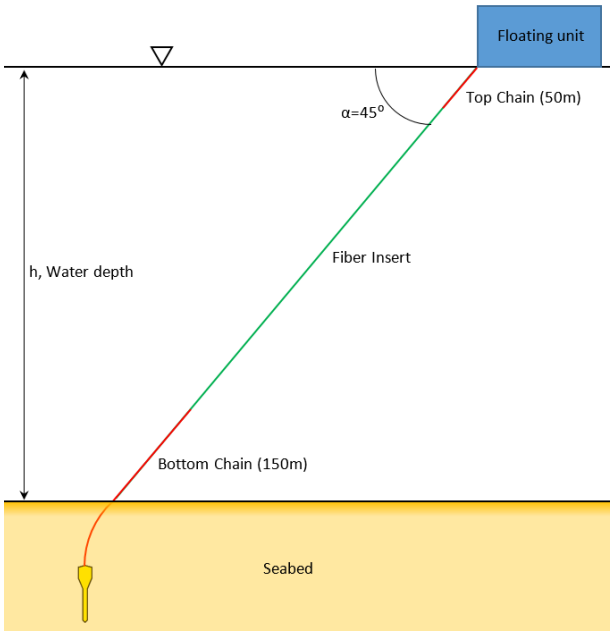

Figure 5-2: Taut leg mooring system. Determining fiber insert length. (K. Larsen, 2015).

If the fiber insert lengths calculated with Equation (5-1) are applied directly to the simulation model, the mooring lines will touch the seabed already before anchor drop is initiated. This is not wanted. Based on this, installation should not be carried out with the full length of the mooring line in the water. Consequently, the calculated length of the mooring line is reduced in the model so that the anchor installation is conducted with only the minimum required length. The segment lengths used in the analyses are given in the attached Excel file.

5.2 Anchor

The size of the anchors in a mooring system depends on the moored structure. A permanently moored structure requires larger anchors than e.g. a temporarily present drilling rig. Typical anchor sizes for permanently moored structures ranges from 80-100tonnes (K. Larsen, 2015). In this thesis, parameters for the two full-size anchors installed at the Gjøa field are used as a basis for the RIFLEX model. These anchors were designed for permanently moored structures in areas with soft clay seabed conditions (Jon T. Lieng, 2015). The anchor and its cross-section are presented in Figure 5-3 and Figure 5-4, respectively. Important anchor data are listed in Table 5-1.

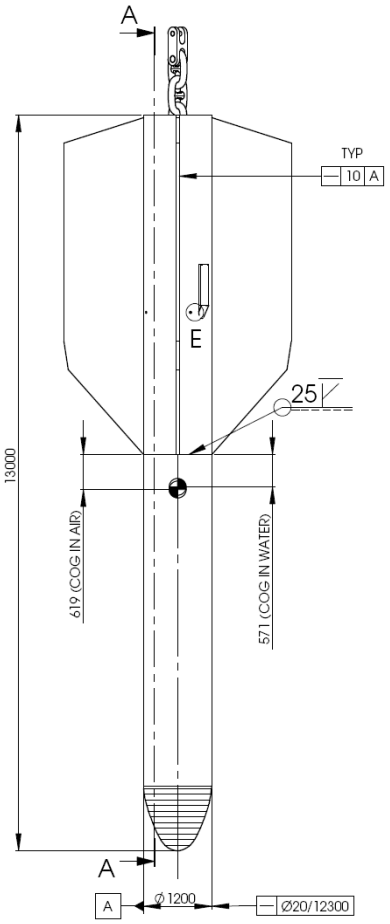

Figure 5-3: 80 tonnes DPA (Jon T. Lieng, 2015).

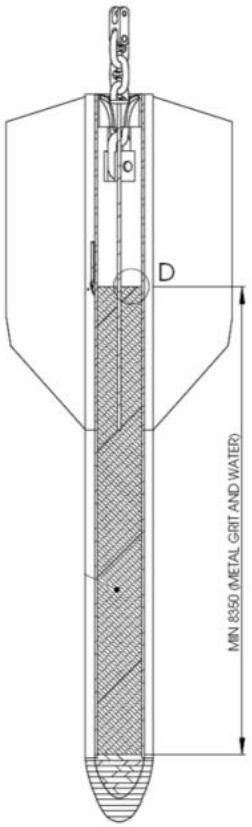

Figure 5-4: Cross-section through A-A of 80tonne DPA (Jon T. Lieng, 2015).

Table 5-1: Technical data for 80tonne DPA installed at the Gjøa field (Jon T. Lieng, 2015).

Parameter	Symbol	Value	Unit
Total length of anchor	L	13	m
Shaft diameter	D_{SHAFT}	1.2	m
Shaft wall thickness	t_{SHAFT}	0.03	m
Total wall area*	A_{WALL}	102.5	m^2
Total fin length	L_{FINS}	6	m
Max diameter fins section	D_{FINS}	4	m^2
Fin plate thickness	t_{FINS}	0.06	m
Total fin area	A_{FINS}	57.5	m^2
Total weight (air)	m	79407	kg
Submerged weight	w_{WATER}	65513	kg
Center of gravity**	COG	6.381	m

* Enclosed water volume is not included.

** Value is measured from the anchor tip.

As shown in Figure 5-4 the anchor is hollow. The grey cross-ruled area represents the filling material used to increase the weight of the anchor. At the Gjøa installation, steel grit with 35% porosity was used (Jon T. Lieng, 2015). The optimal anchor design is to use a solid steel cross-section. However, this is not feasible due to high steel prices. For that reason, a cheaper but still heavy filling material was used. Greater weight produce more kinetic energy for the same drop height. This gives a higher tip penetration, which results in increased capacity performance of the mooring system. The maximum possible touchdown velocity depends on the terminal velocity. This means that if the anchor is released from a height where terminal velocity is reached, the touchdown velocity will not increase further for higher drop elevation above the seafloor. By using a significantly heavy filling material (higher density than steel), the center of gravity (COG) is moved towards the tip. COG should be placed as close to the tip as possible. This increases the hydrodynamic stability, which is dominated by the distance between COG and COB.

If the anchor tilts during free fall, the resultant drag force can be decomposed into a lateral and tangential component. The lateral component acts normal to the anchor center axis, while the tangential component is parallel to the center axis. Figure 5-5 illustrates how the drag forces creates a restoring moment about the rotation point. The position of the rotation point is not constant, it is determined by COG and the sideways-acting force from the permanent mooring line. Drag forces acting on the back tip side of the rotation point creates a restoring moment. The longer the distance between the force and the rotation point, the higher is the restoring moment. On the contrary, a force applied on the tip side of the rotation point gives a tilting moment. The anchor weight will due to its magnitude create a significant restoring moment if COG is located on the tip side of the rotation point. If COG is located at the tip, the only force that will try to tilt the anchor is the lateral component from the mooring line, which is connected to the back tip of the anchor. The anchor model used in RIFLEX is described in detail in Section 6.1.

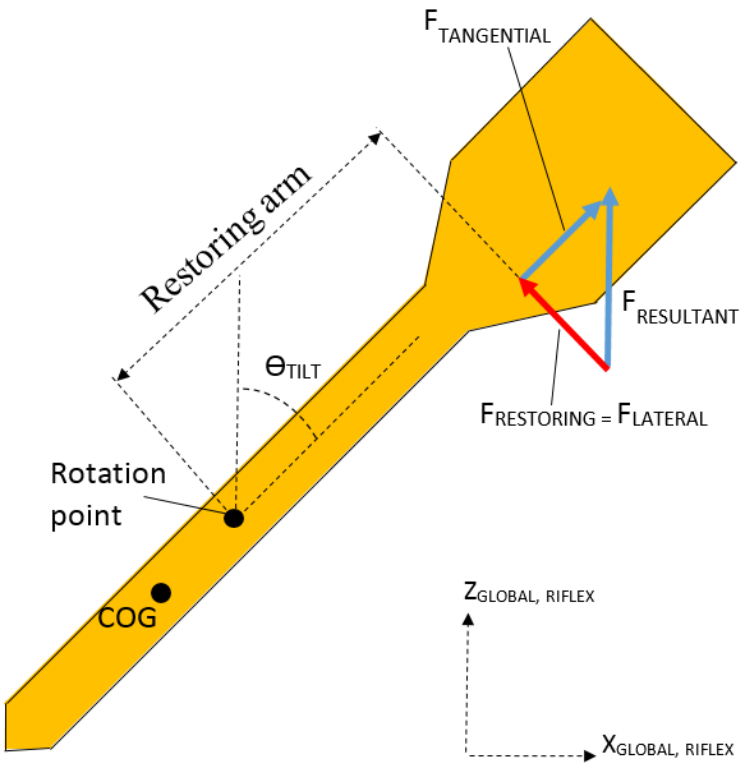

Figure 5-5: Restoring and tilting moment on a DPA.

5.3 Installation Wire

A rule of thumb used for lifting wires states that the wire must be strong enough to withstand at least three times the maximum design load. When selecting a wire for an offshore application, it is important to take dynamic contributions into account. The sea surface is dynamic due to variation in wind-, wave- and current forces. According to (K. Larsen, 2015) a common dynamic amplification factor is 1.3 for this application. The static load multiplied by 1.3 gives the probable highest dynamic load. This is a quasi-static consideration. The dynamic amplification factor indicates that the force in the wire can, due to dynamic system behavior, increase by approximately 30%. An anchor of 80tonnes may therefore give an effective load in the wire of up to 104tonnes.

There are several contributions to the maximum tension in the wire. The installation wire must be strong enough to withstand its own weight, the release unit, the anchor, the vertical chain segment behind the anchor and the weight of approximately 50% of the chain loop next to the anchor. The contributions from the wire and chain segment to the total load are the most significant ones. The total weight of the wire depends on its length, which is a function of water depth, anchor drop height and length of the vertical chain segment. The buoyancy for all elements is subtracted, in order to find the correct maximum top tension.

The installation wire parameters used in this thesis is based on the wire installed on the AHV applied for the DPA installation at the Gjøa field. According to Jon Tore Lieng (2014b), M/S Island Vanguard was at that time equipped with a CLASS 6x37 Steel Core wire, designed after the API 9A – 1995 standard. The nominal diameter was 76 mm. The cross-section of such a wire is presented in Figure 5-6. Each strand (circular bundle of thinner wires) has 18 outer wires. Hence, the total construction consists of 108 outer wires.

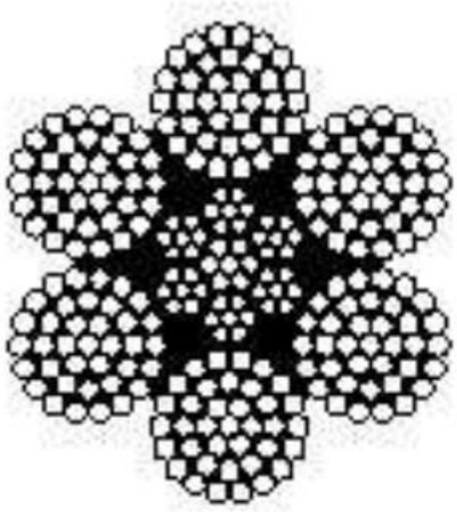

Figure 5-6: Typical cross-section of a steel core class 6x37 wire (American Petroleum Institute, 2011).

At Gjøa, the water depth at the location where the anchors were to be installed was approximately 370m at maximum. In this thesis, water depths up to 3000m are considered. To check whether the selected wire is strong enough for deep-water applications, a simple calculation of the maximum load in the wire is conducted. The result is compared to the minimum breaking strength. The water depth is set to 3000m. The length of the wire is set equal to the water depth. The wire cross-section is assumed to be homogeneous and fully circular, which gives a conservative weight-estimate. The simplified cross-section also increases the buoyancy of the wire, but this effect is negligible since the density of steel is approximately 7.65 times higher than for seawater. Input and output for the calculation are given in Table 5-2.

Table 5-2: Simple calculation of maximum load in installation wire.

Input			
Parameter	**Symbol**	**Value**	**Unit**
Diameter wire	D	76	mm
Length wire	L_{WIRE}	3000	m
Submerged weight wire	W_{WIRE}	30.96	kg/m
Length of chain segments	L_{CHAIN}	50	m
Submerged weight chain	$\mu_{CHAIN,AIR}$	384.54	kg/m
Submerged weight anchor	W_{ANCHOR}	65513	kg
Wire Minimum Breaking load	MBL	516	tonnes
Output			
Total weight wire topside	$W_{TOPSIDE}$	262	tonnes
Safety Margin	W_{MARGIN}	254	tonnes
Calculated safety factor	SF	1.97	--

In Table 5-2, the safety factor is calculated to 1.97 for the water depth of 3000 meters. This is slightly lower than the thumbs rule, which states that the minimum breaking load (MBL) should be at least three times the maximum applied load. However, a safety factor of 1.97 states that the wire is capable of holding roughly twice the weight considered. In a real life operation, a wire with higher capacity would probably be chosen due to strict safety factor requirements. To make a good comparison between the analyses for the different water depths, the wire parameters are kept constant. If the safety factor for the wire is sufficiently high at the deepest water considered, it is definitely high enough for operations in shallower water. As the water depth decreases, the safety factor increases. Shorter wire, constant cross-section and constant load results in a higher safety factor. When the water depth is ≤767 meters, the safety factor reaches a value of 3. The length of the chain loop is then assumed constant.

Technical parameters for wires designed after the API standard can be found with the following formulas.

The axial stiffness of the wire is, according to MARIN (2003), expressed as

$$E_{eff}A = E_{eff}C\frac{\pi}{4}d^2\ [kN] \qquad (5\text{-}2)$$

where E_{EFF} is the effective modulus of elasticity, A is the cross-section area, C is a reduction constant and d is the diameter.

The modulus of elasticity for steel is approximately 210 GPa. However, this value is not used for the wire. The reason for this is that a wire consists of several small diameter steel cables that are braided around each other. Braiding these steel cables together results in property

changes of the wire. E_{EFF} accounts for this effect. If the modulus of elasticity for a wire and a homogenous cable with the same outer diameter were compared, the results would be different. E_{EFF} is set equal to $105 \cdot 10^9 \text{Nm}^{-2}$. This value is obtained from Table 14-1 in APPENDIX A for a six-strand steel core wire.

The cross-section area A, is reduced by the coefficient C, which depends on the construction type and the wire class. C is set equal to 0.418 for the selected wire (API - American Petroleum Institute, 2011). A table for different wire classes are given in Table 14-3 in APPENDIX A.

The wire is modeled with beam elements in RIFLEX. Beam elements requires bending and torsion stiffness as input. The bending stiffness is significantly low in a wire, and reducing the stiffness with the factor C is not sufficient. The second order moment of inertia I given in Equation (5-3) is valid for a homogeneous cross-section. The cross-section shown in Figure 5-6 is not homogeneous and the different strands can glide relative to each other. Hence, the moment of inertia and thus the bending stiffness of a wire is significantly lower than for a homogenous cross-section. After conversation the supervisor C. M. Larsen (2015), it has been decided to reduce the bending stiffness with a factor of 1000 in order to obtain a reasonable value. The factor is included in Equation (5-3).

The bending stiffness of the wire is expressed as

$$E_{EFF} I = E_{EFF} C \frac{\pi}{64 * 1000} d^4 \ [N] \tag{5-3}$$

The torsion stiffness (GI_P) is calculated as

$$GI_P = G \frac{\pi}{32} d^4 \ [N] \tag{5-4}$$

where G is the shear modulus for structural steel, equal to $79.3 \cdot 10^9 \text{Nm}^{-2}$ (Engineeringtoolbox, 2014), and I_P is the polar moment of inertia expressed by

$$I_P \ \frac{\pi}{32} d^4 \tag{5-5}$$

The radius of gyration is expressed as

$$r = \sqrt{\frac{I}{A}} \tag{5-6}$$

It is important to multiply the cross-sectional area with the reduction coefficient C, in order to get the correct radius of gyration.

Technical data for the wire are listed in Table 5-3. The stiffness terms are calculated with Equation (5-2), (5-3) and (5-4). The minimum breaking load is taken from a KISWIRE High Tensile Grade - Delta wire given in APPENDIX A. The tangential added mass coefficient is neglected due to the small shear forces between the water and the wire.

Table 5-3: Wire Parameters (76mm) (KTL Group, 2014) and (DNV, 2013b).

Parameter	Symbol	Value	Unit
Nominal diameter	d	76	mm
Weight in air	μ_{AIR}	24.7	kg/m
Minimum Breaking load	MBL	516	tonnes
Modulus of elasticity	E_{EFF}	105e+9	N/m^2
Cross-section area	A	0.0018438	m^2
Radius of gyration	r	0.0298	m
Axial stiffness	$E_{EFF}A$	2.79e+8	N
Bending stiffness	$E_{EFF}I$	200	Nm^2
Torsion stiffness	GI_P	2.6e+5	Nm^2/rad
Drag coefficient (Lateral)	$C_{D,L}$	1.8	--
Drag coefficient (Tangential)	$C_{D,T}$	0,03	--
Added mass coefficient (Lateral)	$C_{M,L}$	1	--

5.4 Chain

Mooring chains are categorized in different chain grades depending on the tensile strength of the steel used in the manufacturing process (IACS, 2011). Common steel grades for mooring chains are R3, R3S, R4, R4S and R5, sorted from lowest to highest capacity with respect to yield stress and tensile strength. Steel grade R4 is often used. The size of the anchor links varies with the system design loads.

The Swedish Company Ramnäs Bruk is a well-established manufacturer of mooring chains. In this thesis, it is decided to use a stud link mooring chain based on data from Ramnäs Bruk. The stud is the bar standing across the inside width of a chain link (Britannica.com, 2015) (See Figure 5-8). A full table of chain dimensions are given in APPENDIX B. The main reason for utilizing stud links instead of regular studless links is to prevent twisting and the occurrence of

knots on the chain. In terms of a DPA installation, stud links avoid the embedded part of the bottom chain from getting curled. Investigation of the embedded chain is not possible after installation, and it is therefore important to install the system correctly. To prevent curls from appearing, a possible solution is to avoid feeding out too much mooring line behind the anchor during the installation. In this way, the tension in the chain is kept at a reasonable level during the seabed penetration and the links are not able to twist around each other. Experience shows that the fatigue life is considerably reduced if the chain is twisted (K. Larsen, 2015). In 2009, a mooring line at the FPSO vessel Dalia, located off the West coast of Africa, failed below the mudline after only two years in service. Knotting of the chain was the cause of failure. The same thing happened in 2012 (Kai-tung Ma et al., 2013). After full anchor penetration, it was believed that a knot formed in the chain when the chain was tensioned. Usually, a knot would be straightened out by pulling on the line. However, the soil resistance prevented this from happening (Kai-tung Ma et al., 2013). Twisting can cause out of plane loading on the links, in which they are not designed for. Figure 5-7 gives an illustration of how such a chain twist may look like.

Figure 5-7: Twist in chain appearing in clay model test during chain pulling (Total, 2014).

Another advantage of studs is that they prevent the links from getting deformed, which increases the proof load of the chain (Ramnäs Bruk AB, 2006). A studless link will deform easier than a stud link when the chain is exposed to large tension.

The fatigue life of a stud chain is in general higher compared to a studless chain (K. Larsen, 2015). The stud gives a stress reduction in the anchor link due to smaller dynamical stresses. This gives higher fatigue capacity. On the contrary, if a stud detaches, a hotspot is created where the stud was placed. This reduces the fatigue life drastically (K. Larsen, 2015).

Studs also increase the weight and cost. Ramnäs Bruk AB (2006) claims that they can deliver studless chains with the same capacity in terms of static strength as stud chains, but with a reduced weight of 9%. This weight reduction becomes significant for long catenary lines.

Nowadays, it is common to use studless chains. This is because the chains are treated properly to avoid the abovementioned problems (K. Larsen, 2015). However, it is argued to use stud links in the embedded part of the bottom chain because examination of the chain configuration is not possible here. The cost of replacing or repairing a mooring line is much higher than using stud chains in the bottom section.

According to K. Larsen (2015) the nominal diameter of chains used for large permanent moored structures ranges from 130mm to 140mm. Based on this, a chain with a nominal diameter of 142mm is chosen from Table 14-4 given in APPENDIX B.

There are several design standards available for mooring chains. An example is the DNV offshore standard DNV-OS-E302 "Offshore Mooring Chain". DNV (2008) describes the content in the following way:

> *"The offshore standard contains criteria, technical requirements and guidance on materials, design, manufacture and testing of offshore mooring chain and accessories."*

Based on this DNV standard and information from MARIN (2003) and Ramnäs Bruk AB (2006) it is possible to calculate important parameters such as breaking load, proof load, weight per meter, and axial stiffness of the selected chain with R4 steel grade.

The Break- and Proof load can be calculated by using Equation (5-7).

$$LOAD = cD^2(44 - 0.08D) \tag{5-7}$$

c is a factor that is different for the Break Load and Proof load. D is the nominal diameter of the chain given in millimeters. This diameter is illustrated in Figure 5-8. The Break load and Proof load for a Ramnäs Bruk 142mm stud link mooring chain with R4 quality are listed in Table 5-4.

Table 5-4: Break Load and Proof Load for a 142mm Stud Link Mooring Chain From Ramnäs Bruk.

C	***Break Load***	***Proof Load***	***Unit***
0.0274	18033,4	--	kN
0.0216	--	14216,1	kN

The weight per unit length and axial stiffness is, as seen in Equation (5-8) and (5-10), also expressed by the nominal diameter.

$$\mu_{CHAIN,AIR} = 0.0219D^2 \tag{5-8}$$

The submerged weight of the mooring chain can be roughly estimated by the following expression (Ramnäs Bruk AB, 2006).

$$\mu_{CHAIN,WATER} = \mu_{CHAIN,AIR} \cdot \frac{\rho_{steel} - \rho_{seawater}}{\rho_{steel}} \tag{5-9}$$

Where $\rho_{steel} = 7850\ kg \cdot m^{-3}$ and $\rho_{seawater} = 1025\ kg \cdot m^{-3}$.

$$(EA)_{CHAIN} = 54936\left(\frac{\pi}{2}\right)D^2 \tag{5-10}$$

The axial stiffness expressed by Equation (5-10) gives a lower value than what you get by $E \cdot A$ with E=210GPa. This implies that a safety factor is implicitly included, since the strain will be larger for the same load.

The design of a common stud link in a mooring chain is shown in Figure 5-8. D represents the nominal diameter used in the equations above.

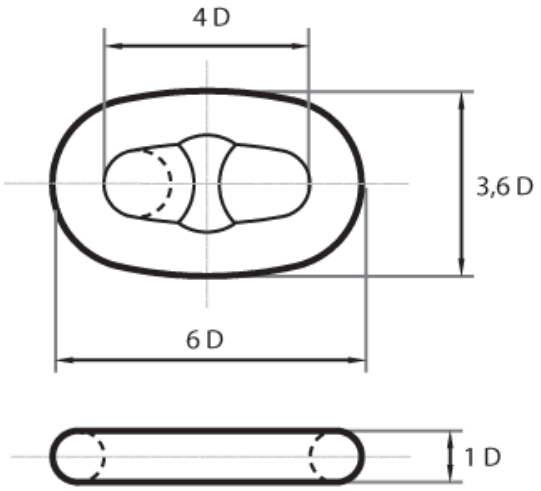

Figure 5-8: Common stud link (Sotra Anchor & Chain, 2015).

A mooring chain consist of several individual links that can rotate relative to each other. For that reason it is important to remember that a chain has no bending stiffness (EI). The only possible contribution to bending stiffness arise from friction forces on the contact surfaces between links when they rotate relative to each other in a tensioned mooring chain. This contribution is negligible. In software such as MIMOSA, delivered by MARINTEK, the bending stiffness in the mooring lines are neglected (MARINTEK, 2003). As a result of this, it may be argued to model the segments with bar elements. Seen from another point of view, bar elements under compression can give numerical instabilities in the calculation. Beam elements are therefore used for all segments.

The lateral stiffness of a beam element have two contributions, bending- and geometric stiffness. The geometric stiffness is determined by the axial tension in the segment. The equilibrium condition for a slender, vertical structure exposed to lateral forces is obtained by a change in the geometry. The force in a wire, chain or fiber will always follow the axial direction. When the orientation of the center axis is changed as the system falls down, the axial force in the deformed shape will create force components in the global coordinate system that outbalances the external forces. In this way, equilibrium is achieved by a change in the geometry, without necessary changing the axial tension. This type of stiffness is the so-called geometric stiffness (C. M. Larsen, 2015). Geometric stiffness can easily be described as the stiffness contribution from the axial force to the transverse stiffness (MARINTEK, 2014a). This applies to both the chain, wire and fiber. When the anchor is released, the axial tension approaches zero in some parts of the mooring line after a certain time. Mainly in the part of the chain loop next to the anchor. At this point, the geometric stiffness is zero. If the bending

stiffness is neglected, and the axial tension cease to exist, the beam element has no lateral stiffness left. The element is at this point not able to withstand any force in the lateral direction. This scenario may cause numerical problems in RIFLEX. To overcome this problem, some bending stiffness is added to compensate for cases where the tension in the line is zero. This ensures numerical stability in the calculations. Hence, the bending stiffness is set to 1 Nm^2.

Figure 5-9 gives an illustration of a mooring line with/without axial tension. In the picture on the left-hand side, the anchor and mooring line is hanging in the drop configuration, ready to be released. In the picture on the right-hand side, the system is free falling, and a curled section of the line is observed inside the red circle. This is a result of lack of lateral stiffness, caused by zero axial tension.

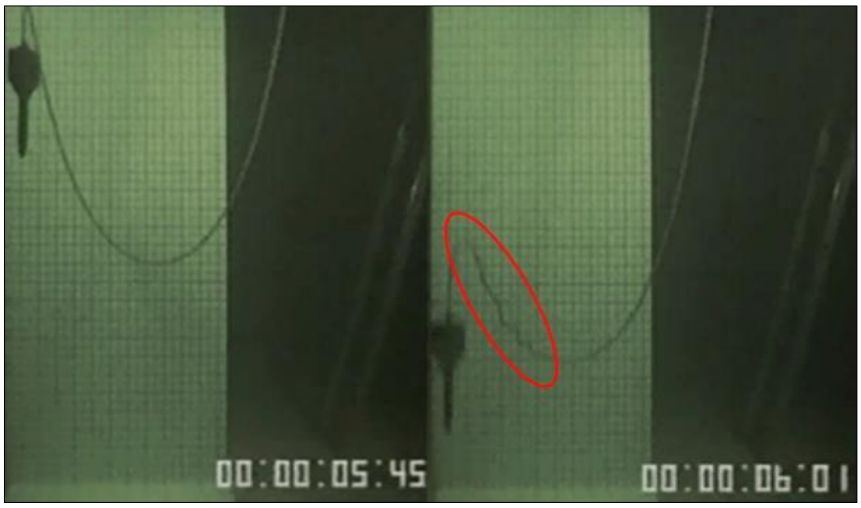

Figure 5-9: DPA Model test – Scale 1:25 (Jon Tore Lieng et al., 2000).

The torsion stiffness in the chain is also dependent on the tension in the segment. After release, a certain tension is preserved in the vertical chain segment due to the weight of the anchor dragging the system downwards and the oppositely directed friction and pressure forces on the chain. The half-bow chain segment will lose its axial tension after release as shown in Figure 5-9. The torsion stiffness of the chain is, after conversation the supervisor C. M. Larsen (2015), set to 200 Nm^2/rad. The basic idea is to use a low but at the same time high enough value obtain equilibrium in the calculations. Since the problem is in 2D, the torsion stiffness is not of importance with respect to the results of the analyses.

The DNV standard DNV-OS-E301 “Position Mooring” (DNV, 2013b), contain values for the lateral and tangential drag force coefficients on a mooring chain segment. The values are 2.6 and 1.4, respectively. Both the lateral and tangential drag coefficient from DNV are scaled according to Equation (5-11).

$$f = \frac{1}{2}\rho C_D \mathrm{D} \cdot v \cdot |v| \tag{5-11}$$

where f is the drag force per unit length, C_D is the respective drag coefficient, D is the nominal diameter of the chain and v is the velocity component in the respective direction (DNV, 2013b).

The values from DNV are valid for stud chains without marine growth. The coefficient are intended for calculation of drag forces due to waves and current. According to DNV (Nestegård, 2015) they can only be used as a rough estimate. There are very little available data on these coefficients, and the values are therefore uncertain. Consequently, they may not be valid for the cases considered in this thesis. A drag coefficient depends on several parameters such as cross-sectional shape, the Reynolds number and the relative surface roughness (MARINTEK, Huse, & Øritsland, 2000). The velocities for the falling anchor is significantly higher than the velocities considered in the DNV standard. A current velocity of 1m/sec is considered to be fast, but the anchor may reach velocities up to 30m/sec. In addition, the anchor has a one-dimensional velocity with a pure axial flow pattern. In a normal catenary system, the fluid motion in a wave creates a two-dimensional flow pattern, meaning it has a velocity component in both the horizontal and vertical direction. Based on this, the DNV values are primarily intended for a different application. The values are however used in the Case studies in Section 8 to examine their influence on the system response.

In RIFLEX, the lateral- and tangential drag coefficients are scaled with respect to different areas. The lateral drag force refers to the projected area used in Equation (5-11), while the tangential drag force is scaled with respect to the cross-sectional wetted surface $S_{w,2D}$ given in Equation (5-12).

$$S_{w,2D} = 2\pi \mathrm{r} = \pi \mathrm{D} \tag{5-12}$$

As a result of the different area references for the tangential drag coefficient, the value obtained from DNV must be converted to a RIFLEX input value. This conversion is performed with Equation (5-13) and (5-14).

$$S_{w,2D} C_{D,T,RIFLEX} = \mathrm{D} C_{D,T,DNV} \tag{5-13}$$

$$C_{D,T,RIFLEX} = \frac{1}{\pi} C_{D,T,DNV} \tag{5-14}$$

where $C_{D,T,DNV} = 1.4$. This gives $C_{D,T,RIFLEX} = 0.4456$.

Cross-sectional parameters for the chain used in this thesis are given in Table 5-5. The modulus of elasticity is chosen slightly larger than the minimum value, which according to DNV (2013b), cannot be less than $5.6 \cdot 10^{10} Nm^{-2}$ for a stud chain of steel grade R3, R4 or R5.

Table 5-5: Technical data for the mooring chain (D=142mm) (Ramnäs Bruk AB, 2006).

Parameter	Symbol	Value	Unit
Nominal diameter	D_{NOM}	142	mm
Weight in air	$\mu_{CHAIN,AIR}$	442	kg/m
Submerged weight	$\mu_{CHAIN,WATER}$	384.3	kg/m
Minimum Breaking load	MBL	18033	kN
Modulus of elasticity	E	5.49e+10	N/m^2
Cross-section area*	A_{CROSS}	0.03167	m^2
Axial stiffness	EA	1.74e+9	N
Bending stiffness	EI	1	Nm^2
Drag coefficient (Lateral)	$C_{D,L}$	2.6	--
Drag coefficient (Tangential)**	$C_{D,T}$	0.4456	--

*A_{CROSS} for the chain is determined by the sum of the cross-section area of two circles with diameter D_{NOM}.
**Only used in the case studies

5.5 Fiber Rope

There are several manufacturers around the world delivering synthetic fiber mooring ropes to the offshore industry. One of these manufacturers is Parker Scanrope, a company placed in Tønsberg in Norway. The company was in January 2015 bought by Bridon, one of the world's biggest producers of mooring systems (NRK, 2015). Data for a Parker Scanrope MoorLine rope is used in this thesis.

MoorLine ropes are made out of polyester. Other materials such as aramid, LCAP (Liquid Crystal Aromatic Polyester) or polyamide are also used for synthetic fiber ropes. Figure 5-10 presents the cross-section of a Parker Scanrope polyester mooring line and its physical structure.

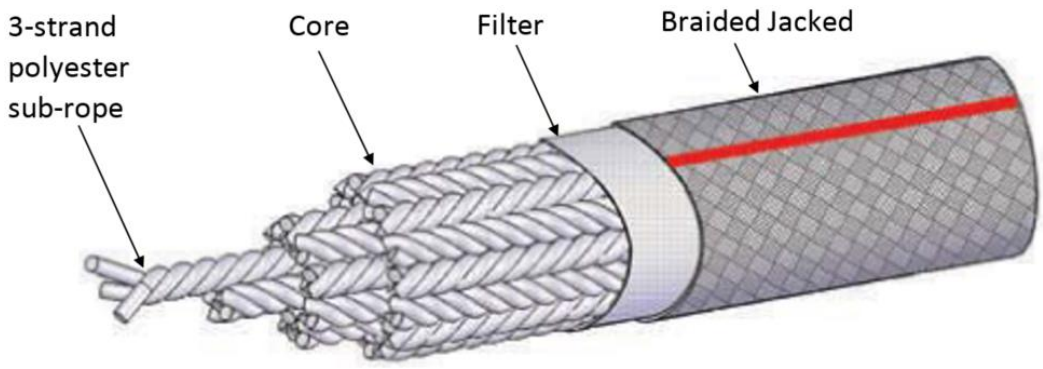

Figure 5-10: Cross-section of a Parker Scanrope Polyester Mooring Line (Parker Scanrope, 2008).

The following text is found in Parker Scanrope (2008). A synthetic fiber rope consists of several layers. The core is the load-bearing part of the cross-section. It consists of several 3-strand polyester sub-ropes that lie parallel to each other. It can be seen in the Figure 5-10 that two sub-ropes next to each other are braided in opposite directions, clockwise and anticlockwise. This gives a torque neutral rope. Outside the core, there is a filter. The intention of the filter is to protect the core from sand, mud and other particles in the water that can cause abrasion. It also protects the core against marine growth, which is a criterion in (DNV, 2013a). Marine growth increases the weight and can wear out the load bearing part of the fiber rope. The outer layer (braided jacket) holds the individual strands in the core together and protects the filter and sub-ropes from abrasion damage.

Fiber ropes used in mooring systems can be verified and certified in accordance with standards such as the DNV offshore standard DNV-OS-E303 "Offshore Fibre Ropes". This standard contains *"…technical requirements to offshore fibre ropes and offshore fibre tethers, and requirements to documentation for verification and certification*" (DNV, 2013a). The objective of the standard is according to *DNV (2013a):*

> "*…to ensure that the design and manufactured quality of offshore fibre ropes and offshore fibre tethers meet the requirements of designated locations, handling and service scenarios for offshore applications, as basis for ensuring reliable offshore systems that use load-bearing lines made from synthetic fibre materials.*"

DNV (2013a) gives several requirements for synthetic fiber ropes. They are for instance sensitive to sunlight and should be protected and covered during storage and transport. Fiber ropes shall never be in contact with the seabed. Sand, mud and rocks can wear out the fibers in the rope. It is therefore important to employ a sufficiently long bottom chain so that the fiber

rope stays off the ground even when the tension in the line is at its minimum. Fiber ropes should neither be used in water with emulsified particles. The particles can *"…be transported into the load-bearing rope by the water that seeps in and out during loading"* (DNV, 2013a). This wears out the fiber.

It is required that the entire length of the mooring line shall be submerged at all times during service. This is to make sure that the mooring lines do not interact with vessels operating close to the floating unit. Interference with a vessel can cause line break, or the fiber rope could get stuck in the propeller. The requirement also prevents the line from being directly exposed to sunlight.

The following information is found in DNV (2013a) and K. Larsen (2015). The selection of a synthetic rope is often based on a criterion stating that the strength of the rope must be equal to or higher than the strength of the chain segment in the mooring line. The strength of the individual line segments can in principle be chosen as desired, as long as they satisfy the design loads. However, safety factor requirements are usually compared to the weakest component in the line. Based on this, it is common to choose components with the same MBL along the line. It is however not recommended to use the minimum breaking strength as the governing performance characteristic. Other characteristics such as change-in-length (CIL) and Tension-Time-Temperature performance (3-T) are more important for the load-bearing capacity of a fiber rope. MBL is although used as a reference for different rope dimensions as seen in APPENDIX C. The selected mooring chain in Section 5.4 has an MBL of 18033kN. Based on this, a synthetic fiber rope with a diameter of 254mm is selected in APPENDIX C due to its larger MBL value (18369kN). Hence, the strength of the fiber rope is sufficiently high.

In real situations, the axial stiffness of a fiber rope is not necessarily linear and must be found with tests. As the axial load increases and the rope is stretched, the contact forces between the individual strands in the rope increases. This is due to friction between the contact surfaces in the yarns in the rope. The friction coefficient may be assumed constant. Hence, if the contact forces increase, also the friction force must increase (C. M. Larsen, 2015). Load-elongation models are widely used to describe the axial stiffness of such ropes. Both linear and nonlinear models are used. K. Larsen (2015) argues that a linear stiffness model is a good approximation for the case investigated in this thesis, and a value of 20·MBL is adequate for the axial stiffness (EA). In Parker Scanrope (2008) the static stiffness in the ropes are tested for loads in the range 12.7·MBL to 18.4·MBL, and the dynamic stiffness is tested for loads up to 30.8·MBL. A value of 20·MBL may therefore be considered as a good mean value.

The axial tension and thus the axial stiffness is very important in a slender marine structure. NTNU, 4Subsea et al (2014) claims that "*A key feature of slender marine structures is that the global geometry is strongly related to axial tension. The main contribution to stiffness versus lateral loads from waves and current, origins from axial tension*". Hence, the tension is controlling the shape of the mooring line.

The modulus of elasticity of the fiber rope, expressed by Equation (5-17), is calculated from the assumed value for the axial stiffness.

$$\mathrm{EA} = 20 \cdot \mathrm{MBL} \tag{5-15}$$

$$\mathrm{E} = \frac{20 \cdot \mathrm{MBL}}{A} \tag{5-16}$$

$$\mathrm{E} = \frac{20 \cdot \mathrm{MBL}}{\frac{\pi}{4} D^2} \tag{5-17}$$

With MBL = 18639kN and D = 254mm the modulus of elasticity is calculated to E=7.36·10^{7}Nm^{-2}.

The bending stiffness of a fiber rope is closely to non-existent. However, every small yarn in the rope has a small EI value that contributes to the total bending stiffness of the fiber rope. It is the friction forces between the yarns that controls the bending stiffness. A value is found by scaling test results provided by Statoil and Larsen (2014) for a rope with MBL = 7848kN and a diameter of approximately 150mm. The lowest value in the test was EI = 267Nm^2 for a bending radius of 0.75m. By utilizing that the second moment of area for a solid circular cross-section is proportional to the fourth power of the diameter, the bending stiffness can be scaled with Equation (5-19). The terms in the equation is explained in Figure 5-11.

$$\frac{(EI)_1}{{d_1}^4} = \frac{(EI)_2}{{d_2}^4} \tag{5-18}$$

$$(EI)_2 = \frac{{d_2}^4}{{d_1}^4}(EI)_1 \tag{5-19}$$

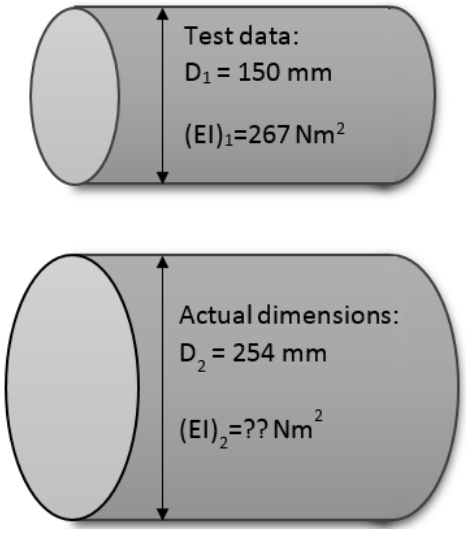

Figure 5-11: Scaling of bending stiffness (Statoil & Larsen, 2014).

By using the given values in Figure 5-11 and the selected fiber diameter, the bending stiffness is calculated to approximately 2200 Nm^2.

The torsion stiffness is determined by the same expression as for the installation wire, Equation (5-2). Torsion stiffness is not a big concern in this thesis. Hence, the value for the torsion stiffness is found by multiplying the bending stiffness by a factor of 2. This gives a torsion stiffness of 4400 Nm^2/rad. The factor, equal to 2, represent the ratio between the second moment of area, used in the calculation for the bending stiffness, and the polar moment of area, in the expression for the torsion stiffness. In cases where torsion stiffness is of greater importance, the shear modulus should be found by Equation (5-20).

$$\mathrm{G} = \frac{E}{2(1+\nu)} \tag{5-20}$$

where E is the Modulus of elasticity and ν is the Poisson's ratio for polyester. This value is set to 0.4 (Goodfellow, 2015).

It is important to use good drag and added mass force models for all segments in the mooring line in order to create a realistic simulation of the line behavior. The lateral drag coefficient C_{Dl} for the fiber rope is set to 1.6 (DNV, 2013b). The tangential drag coefficient , C_{Dt}, is found in a Recommended Practice "DNV-RP-C205" (DNV, 2010) and is expressed as

$$\mathrm{C}_{Dt} = C_{Dl}(m + n \cdot \sin\alpha)\cos\alpha \tag{5-21}$$

where C_{Dl} is the lateral drag coefficient, m and n are constants accounting for surface roughness and α is the angle between the longitudinal axis through the fiber rope and the fluid velocity vector v as shown in Figure 5-12. The fiber rope is considered to have a high surface roughness.

In this case, the corresponding constants that accounts for the surface roughness are according to DNV m = 0.03 and n = 0.055.

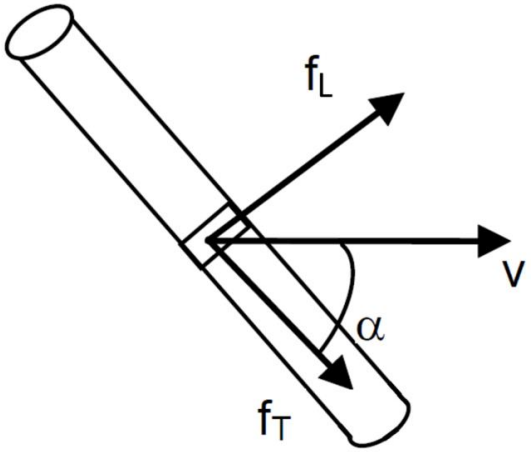

Figure 5-12: Definition of lateral- , tangential- and lift force on slender structure (DNV, 2010).

Assuming α equal to zero in Equation (5-21), the fluid force is acting in the longitudinal direction of the pipe. Equation (5-21) can then be written as

$$C_{Dt} = C_{Dl} \cdot m \qquad (5\text{-}22)$$

By using $C_{Dl} = 1.6$ and $m = 0.03$, the tangential drag coefficient is calculated to 0.048. This value is used in RIFLEX.

The lateral added mass coefficient is set to 1. This value is valid for circular cylinders in infinite fluid (DNV, 2010). This means that the cylinder is far away from boundaries, which is the case in open water. Technical data for the fiber rope used in the RIFLEX analyses is presented in Table 5-6.

Table 5-6: Technical data for a 254 mm MoorLine, a product by Parker Scanrope (Parker Scanrope, 2008).

Parameter	Symbol	Value	Unit
Diameter	D	254	mm
Weight in air	$\mu_{FIBER,AIR}$	42.5	kg/m
Submerged weight	$\mu_{FIBER,WATER}$	10.9	kg/m
Minimum Breaking load	MBL	1.86e+4	kN
Modulus of elasticity	E	7.36e+9	N/m^2
Cross-section Area	A	0.0507	m^2
Radius of gyration	r	0.0635	m
Axial stiffness	EA	3.73e+8	N
Bending stiffness	EI	2200	Nm^2
Torsion stiffness	GI_P	4400	Nm^2/rad
Drag coefficient (Lateral)	$C_{D,L}$	1.6	--
Drag coefficient (Tangential)	$C_{D,T}$	0.048	--
Added mass coefficient (Lateral)	$C_{D,T}$	1	--

5.6 Release unit

A release unit is placed at the lower end of the installation wire. The concept is shown in Figure 5-13. The release unit is assumed to be a circular cylinder with a smooth surface, modeled as a beam element. The minimum breaking load is 546tonnes which is a higher than for the wire (516tonnes). Hence, the release unit will never be the critical component in the system. The modulus of elasticity for steel is used, and the axial stiffness is calculated by the product EA. The bending stiffness (EI), is calculated using the second moment of inertia for a circle and torsion stiffness is calculated with Equation (5-4), the same expression as for the wire.

Figure 5-13: Model 6500/6600 Rig Anchor Release (Inter Ocean Systems, 2014).

All dimensions and parameters used in the analysis are given in Table 5-7. Data for the smallest version, model 6500, is used. This unit has a maximum release load of 273.000kg (273tonnes) which is sufficient for holding the anchor, vertical chain and chain loop used in this thesis with an approximate total dynamic weight of 170tonnes. As for the wire, chain, fiber and anchor, added mass forces in the longitudinal direction is neglected.

Table 5-7: Technical data for the hook/release unit model 6500. Some data are taken from (Inter Ocean Systems, 2014).

Parameter	Symbol	Value	Unit
Diameter	d	0.61	m
Length	L	2.3	m
Total Mass	m	1780	kg
Weight in air	$\mu_{HOOK,AIR}$	774	kg/m
Minimum Breaking load	MBL	~5.4e+6	N
Modulus of elasticity	E	64e+9	N/m^2
Cross-section area	A	0.292	m2
Radius of gyration	r	0.1525	m
Axial stiffness	EA	6e+10	N
Bending stiffness	EI	4e+8	Nm^2
Torsion stiffness	GI_P	1e+9	Nm^2/rad
Drag coefficient (Lateral)	$C_{D,L}$	0.7	--
Added mass coefficient (Lateral)	$C_{M,L}$	1	--

In the analyses, the length of the hook is set to 2m. It is presented in the model as a 2m long beam element in the lower end of the installation wire. to get the correct total weight, a mass coefficient of 980 kg/m is used. Since the hook is 0.3 meters shorter than it is in real life, the buoyancy is reduced a little bit. This reduction is insignificant.

5.7 Stretching of Wire and Chain

During a DPA installation, it is important to account for stretching/elongation of the installation wire and the vertical chain segment. This elongation will reduce the calculated drop height if it is not taken into consideration. The wire and vertical chain segment is stretched due to the large weight of the components, including the anchor. The model used for calculating elongation of the wire and chain is shown in Figure 5-14. The figure includes terms used in the calculation.

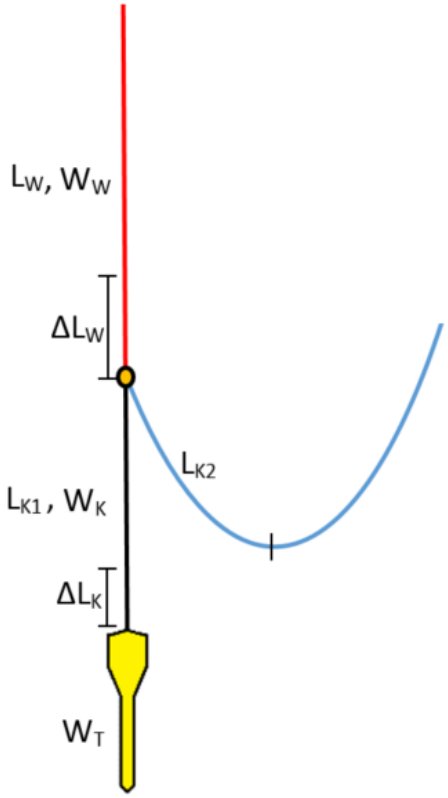

Figure 5-14: Stretch model of anchor system (C. M. Larsen, 2015).

The longitudinal elongation of a bar or a beam is expressed as the tension force applied to the beam divided by the axial stiffness per length. This is shown in Equation (5-23). The formula applies within the yield limit of the material.

$$\Delta\text{Length} = \frac{Force}{Axial\ stiffness\ pr\ length} \tag{5-23}$$

The elongation of the wire and the chain is calculated separately and added together in the end. The wire is exposed to the weight of itself, the anchor, vertical chain segment and half the chain loop. The length of half the chain loop is found by visual inspection of the static equilibrium in Model 1 in RIFLEX. When static equilibrium is found, the bottom element number in the chain loop is read out from the visualization plot in order to know how many elements half the loop consist of. By multiplying the number of elements with the element length, the length of half the chain loop is found.

The wire top is exposed to the largest tension. Hence, the most significant stretching occurs here. When moving down along the wire, axial tension decreases and so does the elongation. C. M. Larsen (2015) argues that this effect should be taken into account by only multiplying half the wire length with the cross-sectional weight. This gives fairly accurate results for the

elongation. This assumption also applies to the chain. By inserting the terms from Figure 5-14 into Equation (5-23) the elongation of the wire can be expressed as

$$\Delta L_W = \frac{W_W \cdot \frac{L_W}{2} + W_K \cdot L_{K1} + W_K \cdot L_{K2} + W_T}{\left(\frac{EA}{L}\right)_W} \tag{5-24}$$

where W_W and W_K is the weight per meter of the wire and chain, W_T is the total weight of the anchor, L_W, L_{K1} and L_{K2} is the initial length of wire, vertical chain and half the chain loop, respectively, and the denominator is the axial stiffness of the wire. The initial length of the wire is determined by

$$L_w = h - h_{DROP} - L_{Anchor} - L_{K1} \tag{5-25}$$

where h is the water depth, h_{DROP} is the drop elevation above seabed and L_{ANCHOR} is the length of the anchor.

The vertical chain only feels the weight of itself and the anchor. Hence, the weight of the wire and chain loop are excluded in Equation (5-26) representing the chain elongation.

$$\Delta L_K = \frac{W_K \cdot \frac{L_K}{2} + W_T}{\left(\frac{EA}{L}\right)_K} \tag{5-26}$$

$\left(\frac{EA}{L}\right)_K$ is the axial stiffness of the chain.

The total elongation, which determines the vertical coordinate of the anchor tip for a given wire length, is given by

$$\Delta L_{TOT} = \Delta L_W + \Delta L_K \tag{5-27}$$

The result of wire and chain elongation is presented in APPENDIX D.

6 Modelling

The main goal of the RIFLEX models is to describe the anchor and mooring line behavior in a realistic manner. The model should be able to reproduce and simulate results measured during testing, such as touchdown velocity, tilt angle and typical line behavior.

The simulation of the anchor and mooring line is separated in two models, Model 1 and 2. The main reason for splitting the system is two models, is to save computational time. The first model is used to find the static equilibrium coordinates of the connection point between the anchor, installation wire and mooring line. The second model is used to simulate the anchor drop. Results from Model 1 are used as input to Model 2. This gives the same static equilibrium condition of the anchor, vertical chain and mooring line. Both models are to be considered as 2D-problems since no forces or displacement are considered in the y-direction (into the plane). All y-coordinates are therefore set to zero. The models are created for water depths ranging from 400m and 3000m.

All components in the system are modeled using beam elements and the axis symmetrical cross-section CRS1. The beam element in RIFLEX can deal with large displacements and rotations, and at the same time, small strains (MARINTEK, 2014a). This type of behavior is typical for slender marine structures.

Current is the only environmental force implemented in the models. Forces and displacements due to wind, waves and vessel motions are not included. Therefore, the upper ends of the wire and mooring line are assumed fixed.

6.1 Anchor Model

It is hard to model the anchor in RIFLEX using the exact geometry shown in Figure 5-3 and Figure 5-4. Hence, a simplified model is made. However, in order to get the most accurate and realistic anchor drop simulation, implementation of correct mass and COG is important. A single finite beam element in RIFLEX has constant cross-sectional properties along its length, while the cross-sectional properties for the anchor varies over its length. The anchor must therefore consist of several elements. It is decided to use five elements in the anchor model; three main elements and two short front and back tip elements. The shape of the anchor and its density is assumed constant. The outer geometry is a circular cylinder with constant diameter and the density for structural steel is used. The cross-section of the RIFLEX anchor model is

shown in Figure 6-1. Each element is represented by its own number and color. The stippled fins in the figure are not modeled in RIFLEX. It should be noted that the figure is not to scale.

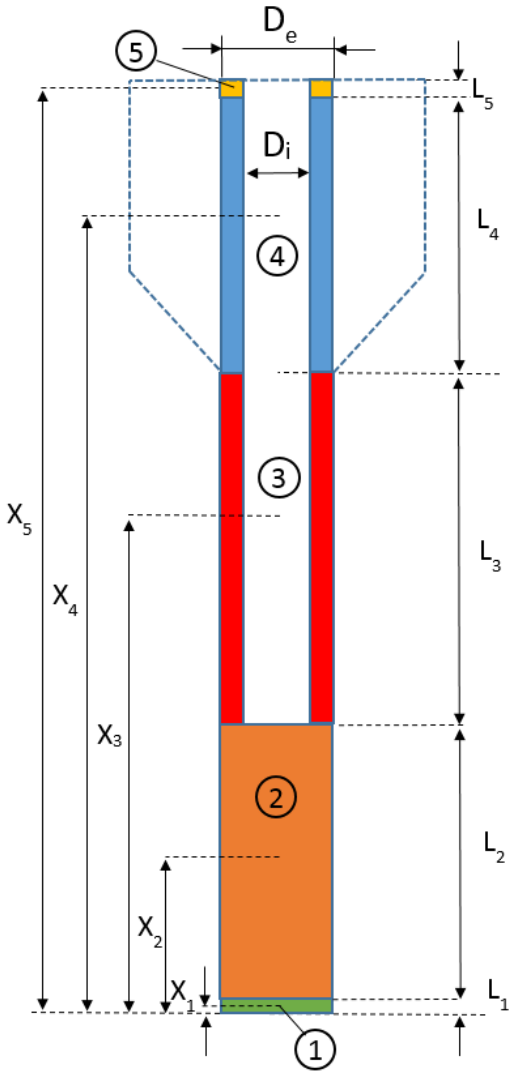

Figure 6-1: RIFLEX Anchor Model (C. M. Larsen, 2015).

Forces cannot be applied to the end surfaces of a geometry in RIFLEX. In this context meaning the top and bottom of the anchor. As a result of this restriction, the pressure force in the front section is applied as a tangential force $F_{D,T}$ on the sidewall of Element 1. The short tip element is therefore given a large tangential drag coefficient to account for the significant pressure drag resistance in this region. This is illustrated in Figure 6-2. The same method is utilized for Element 5, which accounts for the suction drag arising at the anchor back tip. Element 1 is assumed to absorb 90% of the total pressure drag forces while Element 5 absorbs 10%. This percentage distribution is chosen based on conversation the supervisor C. M. Larsen (2015).

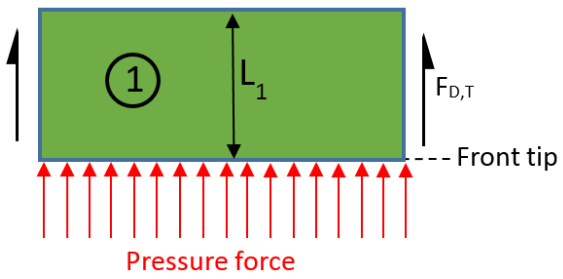

Figure 6-2: Force on anchor tip element (C. M. Larsen, 2015).

In the mid-section, covered by Element 2 and 3, frictional resistance is dominating. If the tilt angle is zero (vertical configuration), no pressure drag occurs in this region. The reason for this is that a pressure force acts perpendicular to the surface of interest. When the anchor falls with zero tilt angle, the fluid velocity vector is parallel to the element surfaces and the only resistance is shear forces between the element surface and the surrounding water. It is therefore preferable to have smooth body surfaces to increase the terminal velocity.

The rear part is covered by Element 4 and 5. There is frictional resistance on both the shaft and the fins, and a pressure drag contribution at the fins cut-off trailing edge. Here, the flow separates and a low-pressure wake occurs. As mentioned above, Element 5 takes this low-pressure into account with a large tangential drag coefficient.

If there is a lateral fluid velocity component on the anchor, the lateral drag force is significantly higher on Element 4 and 5 than for all the other elements due to the presence of the fins. The projection of the anchor is in this region, seen from the side, close to a large flat plate, while the projection of the remaining sections is much more slender. The drag coefficient for a plate is much greater than for a cylinder. This is the fundamental principle for installing the fins in the rear end of the anchor. The fins increase the directional stability of the anchor by creating a large restoring moment when the anchor tilt to either side.

Element 1 and 2 are solid elements with lengths L_1 and L_2, respectively, and a diameter D_e. Element 3, 4 and 5 are hollow elements with lengths L_3, L_4 and L_5, and an external- and internal diameter D_e and D_i, respectively. The correct mass and center of gravity of the anchor model is found by iteration. Two equations, Equation (6-11) and (6-13), and two unknowns, L_2 and D_i, are used to determine the unknown element lengths L_2 and L_3, inner diameter D_i and the distributed mass for all elements. The shaft diameter D_e, total anchor length L, element lengths L_1, L_4 and L_5, COG and total mass M_{tot} are constant and the values are known prior to the anchor calculations. The element lengths, given in meters are as follows

$$L_1 = 0.1 \tag{6-1}$$

$$L_2 = Unknown\ value \tag{6-2}$$

$$L_3 = L - L_1 - L_2 - L_4 - L_5 \tag{6-3}$$

$$L_4 = L_{fins} - L_5 \tag{6-4}$$

$$L_5 = 0.1 \tag{6-5}$$

The mass m_i $(i = 1, \dots, 5)$ for each element is given as

$$m_1 = L_1 \rho_{steel} \frac{\pi}{4} {D_e}^2 \tag{6-6}$$

$$m_2 = L_2 \rho_{steel} \frac{\pi}{4} {D_e}^2 \tag{6-7}$$

$$m_3 = L_3 \rho_{steel} \frac{\pi}{4} \left({D_e}^2 - {D_i}^2\right) \tag{6-8}$$

$$m_4 = L_4 \rho_{steel} \frac{\pi}{4} \left({D_e}^2 - {D_i}^2\right) \tag{6-9}$$

$$m_5 = L_5 \rho_{steel} \frac{\pi}{4} \left({D_e}^2 - {D_i}^2\right) \tag{6-10}$$

The total mass M_{tot} of the anchor is expressed as the sum of all element masses.

$$M_{tot} = m_1 + m_2 + m_3 + m_4 + m_5 \tag{6-11}$$

Equation (6-11) is solved with respect to the inner diameter D_i. This gives Equation (6-12), where the internal diameter is a function of the unknown element length L_2.

$$D_i = \sqrt{\frac{L_{tot} \pi \rho_{steel} {D_e}^2 - M_{tot}}{(L_3 + L_4 + L_5) \pi \rho_{steel}}} \tag{6-12}$$

The expression for D_i is inserted into Equation (6-13) and used to calculate COG, measured from the front tip. Now, the only unknown parameter is L_2.

$$COG = \frac{m_1 x_1 + m_2 x_2 + m_3 x_3 + m_4 x_4 + m_5 x_5}{M_{tot}} \tag{6-13}$$

x_i represents the distance between the center of gravity for element 'i' $(i = 1, \dots, 5)$ and the anchor front tip.

The length of Element 2 and 3, and the wall thickness of the hollow section (determined by D_i) are varied until the correct total weight and COG is obtained. This is conducted with the *"Goal*

Seek" function in Excel. L_2 is adjusted until COG is equal to the known value of 6.381m. At this point, also the total mass is obtained. With COG = 6.381m, the internal diameter is found to be 0.754m. The Excel spreadsheet used for this calculation is found on the attached files.

The axial stiffness (EA) of the anchor is calculated using the elastic modulus for steel equal to 210MPa (eFunda.com, 2015). For Element 3, 4 and 5, which is hollow, it is important to subtract the internal area.

The bending stiffness (EI) is calculated using the second moment of area for a circular, hollow cross-section given in Equation (6-14).

$$I_{circle} = \frac{\pi}{64}(D_e{}^2 - D_i{}^2) \tag{6-14}$$

where D_i is zero for Element 1 and 2.

The torsion stiffness (GI_P) is expressed as

$$K_{torsion} = GI_P = G\frac{\pi}{32}\left(D_e{}^4 - D_i{}^4\right)\,[N] \tag{6-15}$$

Also here, the contribution from the internal area is subtracted for the elements of relevance. For a hollow circular cross-section, I_P is defined as

$$I_P = \frac{\pi}{2}(r_e{}^4 - r_i{}^4) = \frac{\pi}{32}\left(D_e{}^4 - D_i{}^4\right) \tag{6-16}$$

The radius of Gyration for each anchor element is expressed as

$$r = \sqrt{\frac{I}{A}} \tag{6-17}$$

where I is the second moment of intertia for a circle and A is the cross-section area of the wire including the reduction coefficient C.

The anchor is heavy and comparatively much stiffer than the other components in the mooring system. Hence, the minimum breaking strength is set to 40 times the value for the mooring chain (7.21E+8 N).

Since the hollow section of the anchor model is open and filled with water, an internal fluid with seawater properties must be defined in RIFLEX to obtain the correct buoyancy of the anchor.

Input parameters for the RIFLEX anchor elements are listed in Table 6-1 and Table 6-2.

Table 6-1: Anchor element input to RIFLEX.

Element no.	Element Length	Distributed Mass	Axial Stiff. (EA)	Bending Stiff. (EI)	Torsion Stiff. (GI_P)	Radius of gyration
--	m	Kg/m	N	Nm^2	Nm^2/rad	m
1	0.1	9896	2.38E+11	2.14E+10	1.61E+10	0.3
2	0.2838	9896	2.38E+11	2.14E+10	1.61E+10	0.3
3	7.6162	5993	1.44E+11	1.81E+10	1.36E+10	0.3543
4	4.9	5993	1.44E+11	1.81E+10	1.36E+10	0.3543
5	0.1	5993	1.44E+11	1.81E+10	1.36E+10	0.3543

6.1.1 Hydrodynamic force coefficients for the anchor

The anchor is exposed to two types of drag forces - pressure and friction drag. According to CFD Norway AS (1999) the pressure drag coefficient $C_{D,P}$ for the DPA is estimated to 0.43. This value is related to the anchor cross-section area. The reference area $S_{w,2D}$ used for calculation of the tangential drag force per unit length in RIFLEX is given as the cross-sectional wetted surface in Equation (5-12). Over the element length, L, the reference area is written as

$$S_w = 2\pi r = \pi DL \tag{6-18}$$

where D is the element diameter. Since the drag coefficient calculated by CFD Norway AS relates to another reference area than what is used in RIFLEX, $C_{D,P}$ is converted to a RIFLEX input value, $C_{D,P,RIFLEX}$. This conversion is conducted with Equation (6-20).

$$C_{D,P}\pi r^2 = C_{D,P,RIFLEX}\,\pi DL. \tag{6-19}$$

$$C_{D,P,RIFLEX} = \frac{C_{D,P}\pi r^2}{\pi 2rL} = C_{D,P}\frac{r}{2L} \tag{6-20}$$

where r is the element radius.

CFD Norway AS (1999) argues that the friction drag on the anchor may be found with the empirical expression given in Equation (6-21).

$$C_{D,F} = \frac{0.523}{\left(\ln\left(0.06R_{e_L}\right)\right)^2} \tag{6-21}$$

where R_{e_L} is the Reynolds number. According to Deep Sea Anchors (2009) a typical value for the Reynolds number is $R_{e_L} = 130 \cdot 10^6$. With this value, the friction drag from Equation

(6-21) is calculated to 0.00208. The wetted area of the center body of the anchor is approximated by a cylinder of constant diameter (CFD Norway AS, 1999). The friction drag from Equation (6-21) is then converted using Equation (6-22) (Deep Sea Anchors, 2009). The value then relates to the cross-sectional area.

$$C_{D,syl} = C_{D,F}\frac{A_{wet}}{A_{cross-section}} = 4C_{D,F}\frac{L}{D} \tag{6-22}$$

In Deep Sea Anchors (2009) the friction drag on the fins is calculated to $C_{D,fins}$=0.11. By adding up the friction drag coefficient for the cylinder $C_{D,syl}$ and the fins $C_{D,fins}$, and thereafter convert the sum to the correct wetted surface using Equation (6-20) the RIFLEX total friction drag coefficient is found. This value is applied on Element 4 and 5. Only cylinder friction drag is applied to Element 1, 2 and 3.

According to the supervisor C. M. Larsen (2015) the lateral drag coefficient $C_{D,L}$ for Element 1, 2 and 3 may be set to 0.8. For Element 4 and 5, Equation (6-23) is used to calculate to the lateral drag coefficient.

$$C_{D,L,4,5} = 3C_{D,L}\frac{D_{fins}}{D_e} \tag{6-23}$$

This equation gives a value of $C_{D,L,4,5}$=8. C. M. Larsen (2015) argues to add a factor equal to 3, to account for the significantly larger lateral drag forces on a plate compared to a cylinder. The sharp edges on a plate gives rise to vortices. The ratio $D_{fins}{D_e}^{-1}$ is included to account for the fact that the RIFLEX model is simplified by a pure circular cylinder, while the real anchor is equipped with fins. The projected area of the rear section on the real anchor is much larger than for the model. Pressure integrated over a large surface generates more resistance. To make the simplified model physically correct, it must be able to reproduce the forces and behavior of the real anchor. The hydrodynamic forces on the model must therefore be in the same order of magnitude as for the real anchor. If the surface is small, a large force is obtained by a utilizing a higher value for the corresponding drag coefficient. For a normal case, where the model geometry is equal to the real geometry, a drag coefficient equal to 8 is to be considered as artificially high.

Faltinsen (1990) argues that the lateral added mass for a circular cylinder is equal to the displaced mass of the fluid. Hence, the lateral added mass coefficient $C_{M,L}$ is set to 1 for all elements. The tangential added mass coefficient is neglected due to the small shear forces

between the water and the anchor surface. The contribution to the total forces are negligible (C. M. Larsen, 2015). The added mass- and drag coefficients used in RIFLEX are listed in Table 6-2, and all calculations are found in the Excel workbook in the attached files.

Table 6-2: Lateral and tangential added mass coefficients used as input to RIFLEX.

Element	$C_{D,T}$	$C_{D,L}$	$C_{M,L}$
1	1.43097	0.8	1
2	0.09513	0.8	1
3	0.00354	0.8	1
4	0.01224	8	1
5	0.72897	8	1

6.2 Model 1 – Finding Static Equilibrium Coordinates

The horizontal and vertical anchor position is unknown prior to the static equilibrium analysis. The static analysis in Model 1 gives the coordinates of the connection point between the installation wire, mooring line and vertical chain segment that is holding the anchor (see (x_{21}, z_{21}) in Figure 6-4). This is also where the release unit described in Section 5.6 is located. The coordinates (x_{21}, z_{21}) are given as input to Model 2, to ensure correct initial condition for the dynamic analysis.

Two indexations are used to distinguish between the different supernodes and their locations. For a random coordinate x_{ij}, "i" represents the node number and "j" is the configuration. j=0 corresponds to the "stressfree configuration" (start position) and j=1 corresponds to the "static equilibrium configuration" (final position). This is shown in Figure 6-3 and Figure 6-4.

In RIFLEX, all segments are initially modeled in a stress-free configuration. The elements are then not exposed to any strains or forces. The position of the segments is determined by the supernodes, which are located at the segment ends. Both initial and final coordinates are required for the supernodes.

The different loads types are applied to the model in a sequence of load conditions (MARINTEK, 2014a). For the static analysis, described in this section, the applied load types and their sequence order are:

1. Volume forces (weight and buoyancy)
2. Specified displacements (i.e. displacements from stressfree configuration to final position)
3. Position dependent forces (current forces)

The number of load steps and maximum number of iterations during application of load must be given for all the load types. Volume forces are applied during n = 200 load steps and maximum i = 20 iterations, specified displacements n = 300 and i = 20 and current n = 10 and i = 10.

Analyses are conducted both with and without current. The applied current profile is described in Section 6.4.

The respective segment ends that are given a specified displacement, are moved from the initial, stressfree position to final position during a specified number of steps N_{step}. For each step, an incremental node displacement is given. The number of incremental displacements are equal to the number of equilibrium calculations performed between the initial and final position of a supernode. The *RIFLEX Theory Manual* (MARINTEK, 2014a) recommend to use N_{step} in the range of 50-200 steps, but the supervisor (C. M. Larsen, 2015) recommend to use at least 100 steps. Too few steps gives large incremental displacements, which can lead to numerical problems. The installation wire and permanent mooring line are modeled horizontally in the stressfree configuration, and the vertical chain is modeled vertically. This is shown in Figure 6-3. It shall be mentioned that the figure is not to scale.

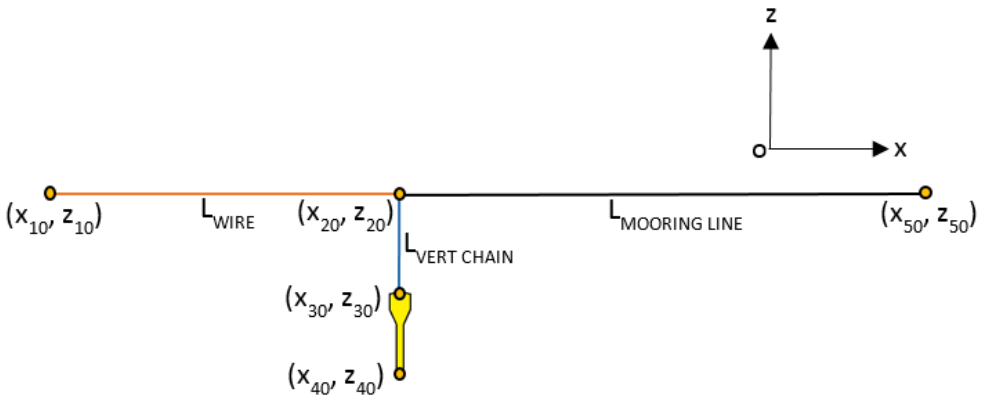

Figure 6-3: Stressfree configuration in static analysis (Model 1) and definition of supernodes.

The orange line in Figure 6-3 represent the installation wire, the blue is the vertical chain and the black is the permanent mooring line. The release unit is modeled with a single beam element and is included in L_{WIRE}. The mooring line consist of two segments; 100m of bottom chain and the remaining length is synthetic fiber. L_{WIRE}, $L_{VERT\ CHAIN}$ and $L_{MOORING\ CHAIN}$ are unstretched lengths and given as input to RIFLEX.

The initial horizontal coordinates of the supernodes are determined by the lengths of the segments. x_{10}=-L_{WIRE}, x_{20}=x_{30}=x_{40}=0 and x_{50}=$L_{MOORING\ LINE}$ for all static analyses in the

model. The initial vertical coordinates varies with the water depths considered. The values are chosen so that the wire and mooring line is not dragged along the sea bottom when specified displacements are applied. The values for z_{30} and z_{40} are determined by z_{20}.

Figure 6-4 illustrates the behavior of the lines from the stressfree condition when volume forces and specified displacements are applied. The red stippled lines represent the path of the specified displacements. The final position of the upper ends of the installation wire and mooring line are then located at the mean sea surface level. DPAs are installed with one or two vessels (Raie & Tassoulas, 2009). If two vessels are used for the operation, the horizontal distance between the upper point of the installation wire and the mooring line represents the distance between the two vessels used for the operation (vessel 1 and 2). This distance affects the sideway force on the anchor from the mooring line. For deep water anchor installations, the ships are located somewhere in the range of 250-350m from each other (K. Larsen, 2015). In this thesis, the distance between x_{11} and x_{51} is set to 10% of the water depth to give a good comparison between the analyses. The final horizontal coordinate of the wire-end is located at x_{11}=0, which means that the mooring line coordinate is located at x_{51}=$0.1 \cdot h$. The coordinates of the three other supernodes, (x_{21}, z_{21}), (x_{31}, z_{31}) and (x_{41}, z_{41}) are free in the final position, and therefore determined by the static equilibrium.

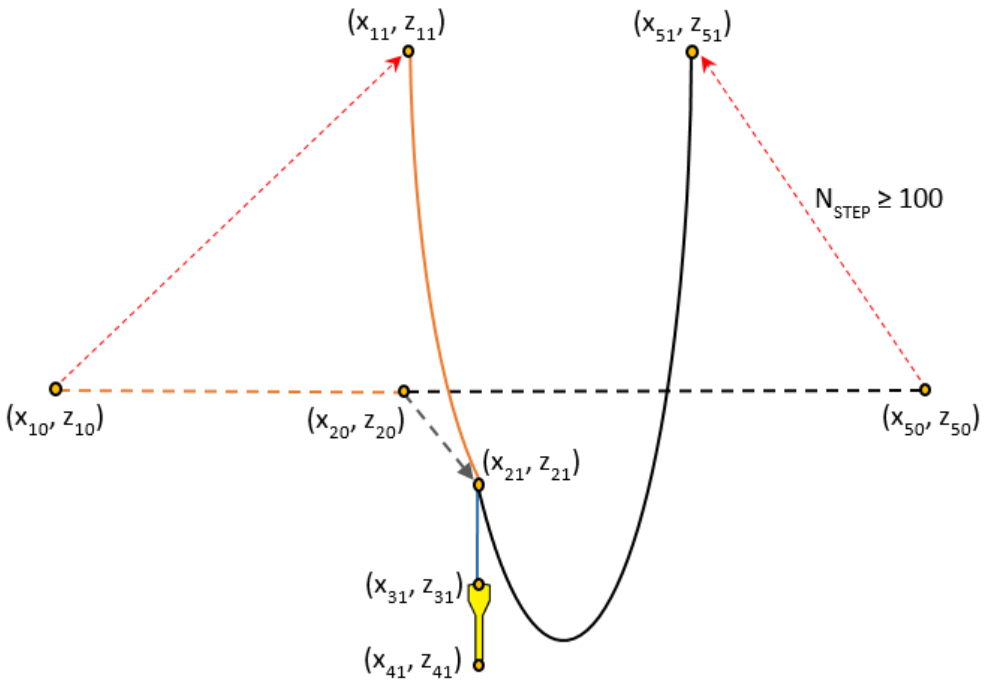

Figure 6-4: Applying Volume Forces and Specified Displacements to Model 1.

As mentioned in Chapter 5, the total length of the fiber calculated with Equation (5-1) are reduced in the RIFLEX models. The segment lengths and corresponding supernode coordinates used in the models are given as a function of the water depth in the attached Excel file. The equilibrium configuration found by RIFLEX is presented in Figure 6-5.

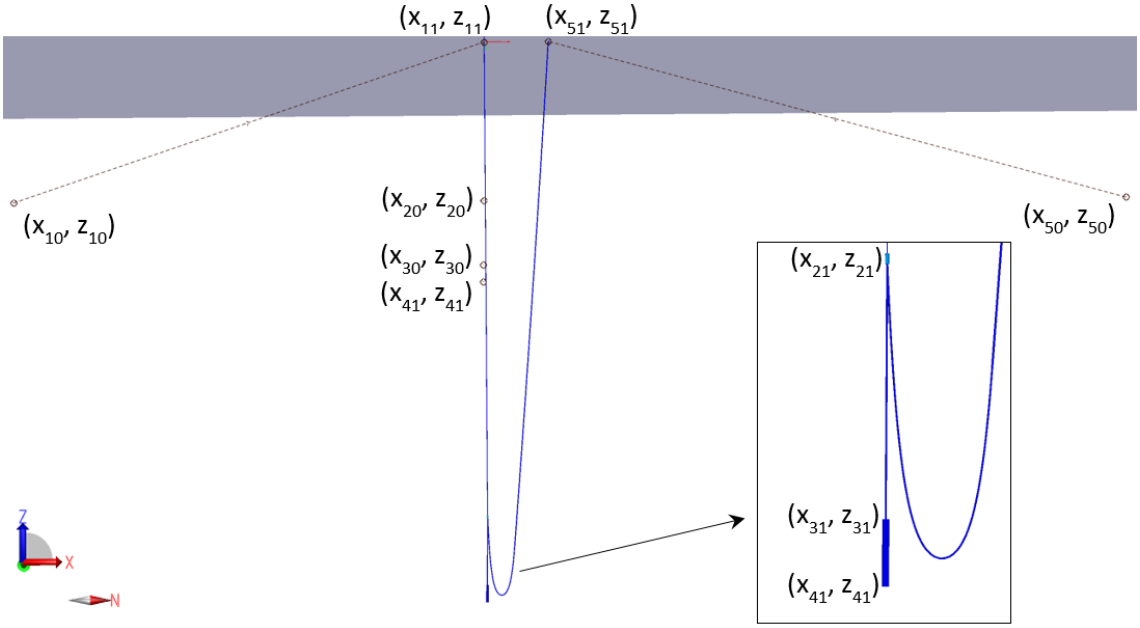

Figure 6-5: Static Equilibrium Configuration in RIFLEX, h=500m.

6.3 Model 2 – Dynamic Analysis of Anchor and Mooring Line

Model 2 is used for investigating the mooring line and anchor during free fall. The only difference between MODEL 1 and 2 with respect to the system components is that the installation wire is removed. The stressfree configuration of the segments is shown in Figure 6-6.

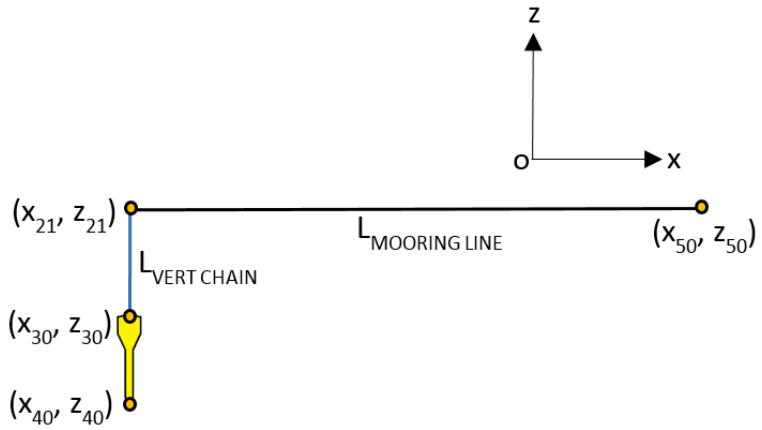

Figure 6-6: Stressfree configuration in static analysis (Model 2) and definition of supernodes.

The coordinates (x_{21}, z_{21}) are obtained from Model 1 to ensure equal static equilibrium configuration of the vertical chain and mooring line in Model 1 and 2. This supernode is fixed in the static analysis in this model. When volume forces are applied, the chain is stretched. This gives a small difference between (x_{30}, z_{30}) and (x_{31}, z_{31}), and (x_{40}, z_{40}) and (x_{41}, z_{41}). Stretching of segments is further explained in Section 5.7. x_{50} is moved relative x_{21}, which means that x_{50}=x_{21}+$L_{MOORING\ LINE}$. The final position of the node x_{51}, is still equal to $0.1 \cdot h$.

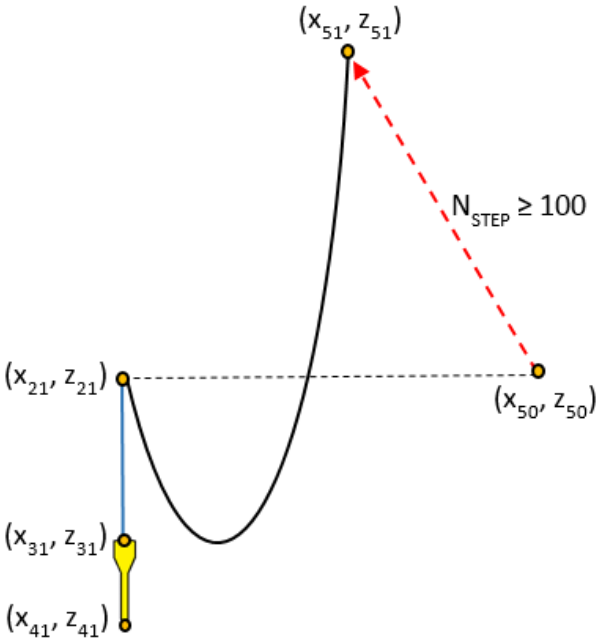

Figure 6-7: Applying Volume Forces and Specified Displacements to Model 2.

After the static analysis is complete and the equilibrium configuration in Figure 6-7 is found, the dynamic analysis is performed. The anchor is then released by changing the boundary condition of the supernode located at (x_{21}, z_{21}) to "free". The anchor, vertical chain and permanent mooring line is then free to fall towards the sea bottom.

The dynamic behavior of the system from initiation of anchor drop until touchdown on the seabed is investigated. The anchor hits the seabed within 10 sec for all cases. Hence, the simulation length is set to 10 seconds. The time step is set to 0.001 sec. This gives 1000 calculations for each simulated second. The dynamic analysis is terminated if a larger time step (e.g. 0.01sec) is used. The visualization length of the response is set to 10 sec with a time increment of 0.1 sec. Snapshots are therefore taken every 0.1 sec.

6.4 Current profile

After conversation the supervisor C. M. Larsen (2015), it is decided to use a current profile with linear variation between specific water depths. The current profile has a maximum current velocity of 0.8m/sec at the sea surface, 0.6m/sec at 300m depth and 0.2m/sec at 400m depth. From 400m and deeper, the velocity decreases linearly to zero at the sea floor. As a result of this, only the lowest part of the current profile varies. In Figure 6-8, the current profile for a water depth of 1000 meters is presented.

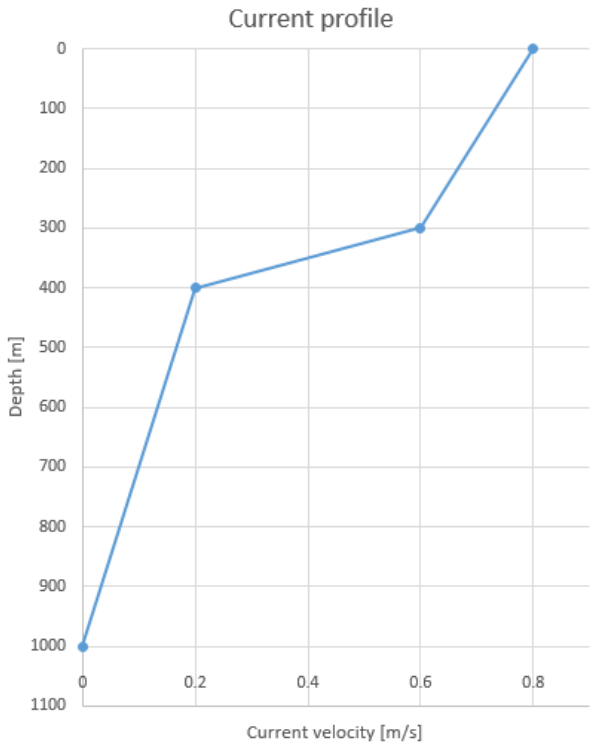

Figure 6-8: Current Profile for 1000 meters water depth C. M. Larsen (2015).

7 Input to/ results from RIFLEX

This Chapter gives a brief description of how Excel and RIFLEX are used together to build up the models described in Chapter 6 and how to find/ post-process the results. The Excel workbook and the RIFLEX Tasks developed throughout the thesis period are to be found in the attached files. Figure 7-1 presents the workflow from input to output with respect to the analyses.

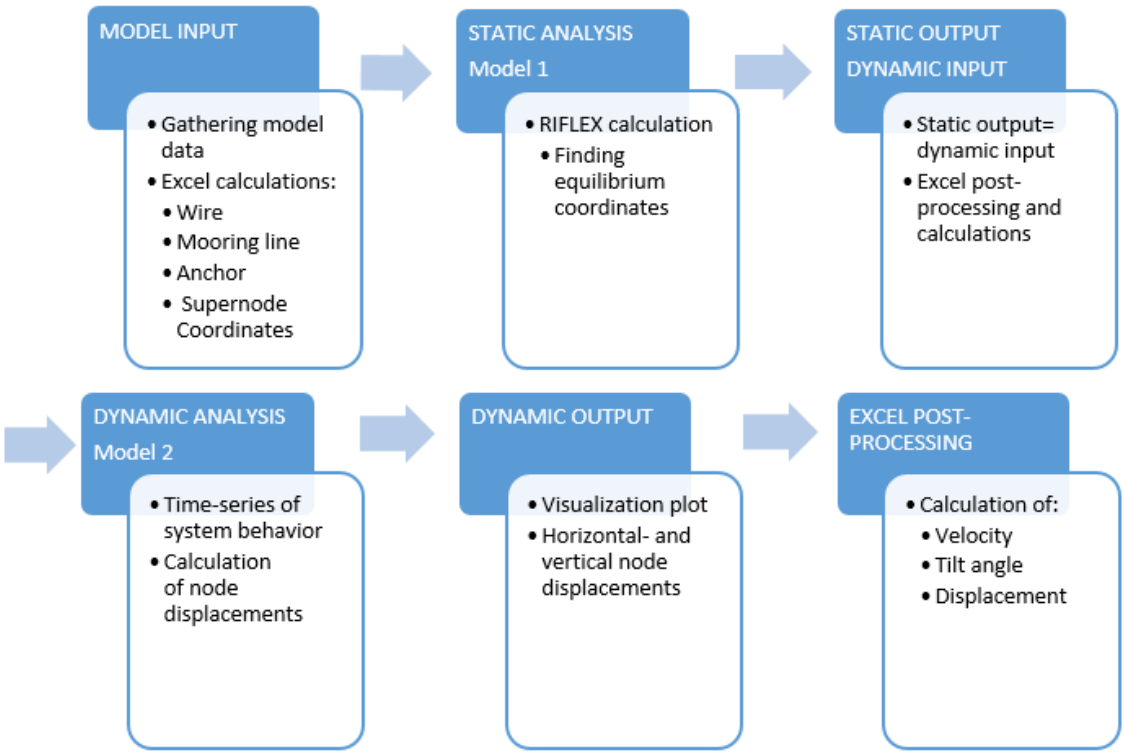

Figure 7-1: Flow chart of calculations and analyses.

7.1 Model 1 – Static analysis

7.1.1 Input

All input data are stored and calculated in an Excel workbook. The workbook contains spreadsheets for the wire, release hook, chain, anchor, fiber line, hydrodynamic coefficients, supernode coordinates and line lengths. The RIFLEX input values calculated in Excel are given manually to RIFLEX.

7.1.2 Output

The output from the static analysis is found in the *sima_stamod.mpf* file in the result folder. The static XZ configuration of the installation wire is selected, and the values in the plot are copied

and pasted into an Excel spreadsheet. Several similar spreadsheets are created, of which contains output data from the respective parameter study. The x- and z-coordinates for the wire bottom end are found in the last row of each column.

7.2 Model 2 – Dynamic analysis

7.2.1 Input

The x- and z- equilibrium coordinates from Section 7.1.2 are input in a spreadsheet that calculates the position of all supernodes in the dynamic analysis model (Model 2). The coordinates are given manually to RIFLEX. The spreadsheet is similar to the one calculating the input coordinates to the static analysis in Model 1.

7.2.2 Output

The data you want RIFLEX to calculate and store are selected under the menu *Dynamic Calculation Parameters*. Displacement data in x- and z-direction for the two end-nodes on the anchor and visualization of the response during free fall are required. The displacement data are obtained by use of Post Processor Tasks. Each Post Processor Task has several Post Processor Specifications, one for each dynamic analysis (RIFLEX Task). Results from each analysis are sent through its Post Processor Specification and exported to Excel files for further post processing. After an analysis is completed, one must click on the export button to obtain the latest output data. Data from all Excel result files are gathered in one workbook. The displacement data are used to calculate the touchdown velocity and tilt-angle of the anchor. The method of calculating these two parameters are explained in the following.

The instantaneous touchdown velocity is determined by investigating the distance traveled during two time steps close up to the point where the anchor touches the seabed. The approximate time of touchdown is determined by visual inspection of the dynamic visualization plot in RIFLEX. The velocity is approximated to be constant during the small time increment (T_2-T_1). This assumption is shown in Figure 7-2. The constant slope of the displacement curve between the two time steps represents the vertical instantaneous velocity.

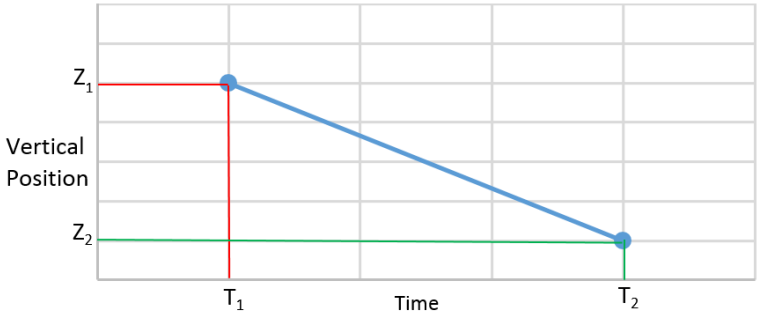

Figure 7-2: Determination of Touchdown Velocity.

Based on the assumption of a constant slope, the vertical instantaneous velocity v_z over the short time increment is given as

$$v_z = \frac{T_2 - T_1}{Z_2 - Z_1} \tag{7-1}$$

where T_1, T_2, Z_1 and Z_2 are the respective time steps and corresponding vertical positions.

The tilt angle is found by comparing the relative position of two points on the anchor at the time of touchdown. This is illustrated by Figure 7-3. The coordinates of the two points forms a right angled triangle where the hypotenuse is equal to the length of the anchor. This is utilized to calculate the tilt angle relative to the vertical in Equation (7-2).

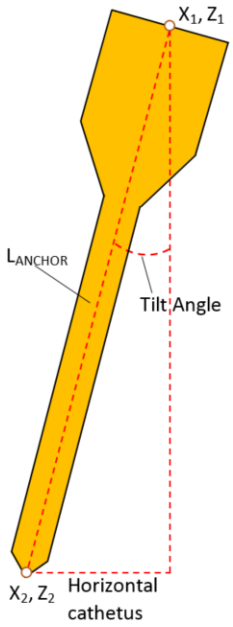

Figure 7-3: Calculation of anchor tilt angle.

The tilt angle is expressed as

$$\theta = \sin^{-1}\left(\frac{x_1 - x_2}{L_{anchor}}\right) \tag{7-2}$$

8 Case Studies

Case studies are performed to see how the static- and dynamic simulation models, described in Chapter 6, behaves with the input parameters from Chapter 5. The results are compared to calculations for the installation at the Gjøa field (Deep Sea Anchors, 2009). In this way, it is possible to verify if the model is able to reproduce the behavior from previous test results and calculations. The velocity and tilt angle at the time of touchdown, mooring line behavior during free fall and displacement due to current are of interest in this chapter. A water depth of 500m is applied. Results from the case studies are given in the following sub-sections.

8.1 Mooring Line Model

This model is similar to Model 2 explained in Section 6.3. All segments are included in the mooring line, which explains the name of the model. Input parameters for the anchor, wire, chain and fiber are the same as given in Chapter 5 and 6. $L_{VERT\ CHAIN}$ is set to 50m. The intension of the model is to see if the anchor and mooring line behaves as expected with the input parameters given in the previous chapters. Especially the tangential chain drag force coefficient is of interest. Table 8-1 contains essential parameters that are varied in the following sections.

Table 8-1: Input Parameters for the Mooring Line Model.

Parameter	Symbol	Value	Unit
Current	$V_{CURRENT}$	0	m/sec
Tangential drag coeff. chain	$C_{D,T,CHAIN}$	0.4456	--
Permanent Mooring line attached	--	Yes	--
Vertical chain attached	--	Yes	--

8.1.1 Touchdown Velocity and Tilt Angle

Equation (7-1) and (7-2) are used with the post-processed displacement data for the x- and z-direction to calculate the touchdown velocity and tilt angle of the anchor. The results are given in Table 8-2.

Table 8-2: Output from the Mooring Line Model.

Parameter	Symbol	Value	Unit
Time of Touchdown	T_{TOUCH}	7.5	Sec
Touchdown velocity	V_{TOUCH}	9.8	m/sec
Tilt angle	θ	1.11	Degrees

The displacement curve for the z-direction used to calculate the touchdown velocity are presented in Figure 8-1. The values are obtained from the bottom node of the anchor (Segment 5, Node 2). The position h (vertical axis) is plotted as a function of time T (horizontal axis).

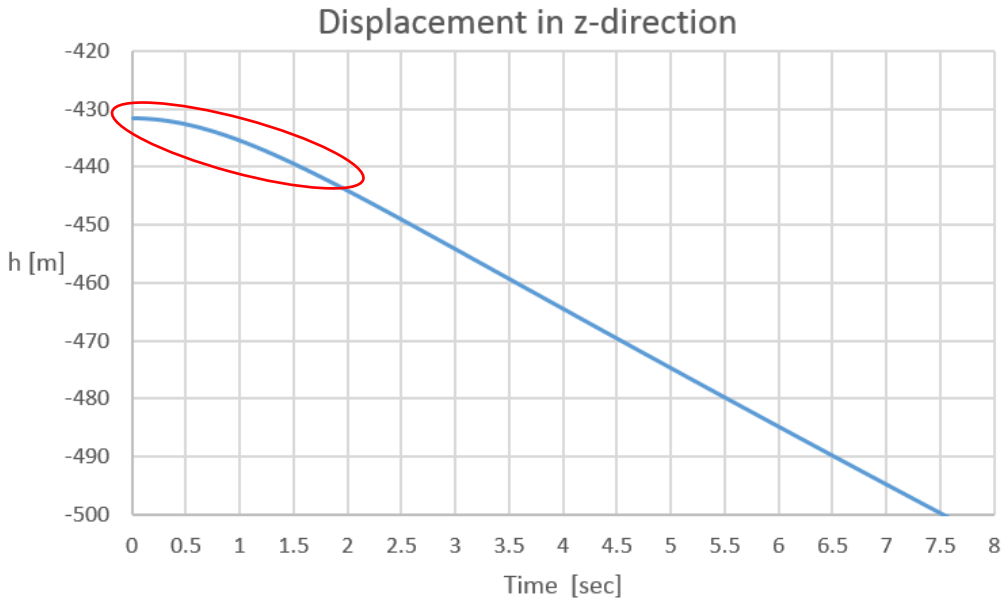

Figure 8-1: Displacement in the z-direction of node 2, segment 5 (anchor tip).

It is observed in Figure 8-1 as well as in the dynamic visualization plot in RIFLEX that anchor touchdown (h = -500 m) appears after approximately 7.5 sec. The slope is constant between 1.5 and 7.5 sec, which means that terminal velocity is achieved already after 1.5 sec. This means that the anchor only accelerates during a short time interval of 1.5 sec (inside the red circle). The touchdown velocity is equal to the terminal velocity since the terminal velocity is achieved before the anchor hits the seabed. The value is calculated to approximately 9.9 m/sec. This is too low and does not correspond to observed velocities during the Troll field test (1:3) or the Gjøa installation (1:1). The short period of anchor acceleration indicates too large resistance in the system. The report from the small scale test (1:25) at MARINTEK's facilities in Trondheim states that a 75 tonnes DPA dropped from a height of 30-40 meters will acquire a velocity of 20-25 m/sec when it hits the seabed (Jon Tore Lieng et al., 2000). During installation at the Troll field and at the Gjøa field (Deep Sea Anchors, 2009), the measured velocity was in this range. This indicates that the RIFLEX model needs some modification in order to represent the measured behavior from the tests.

The x-direction displacement curves of the front- and back tip node of the anchor is plotted in Figure 8-2.

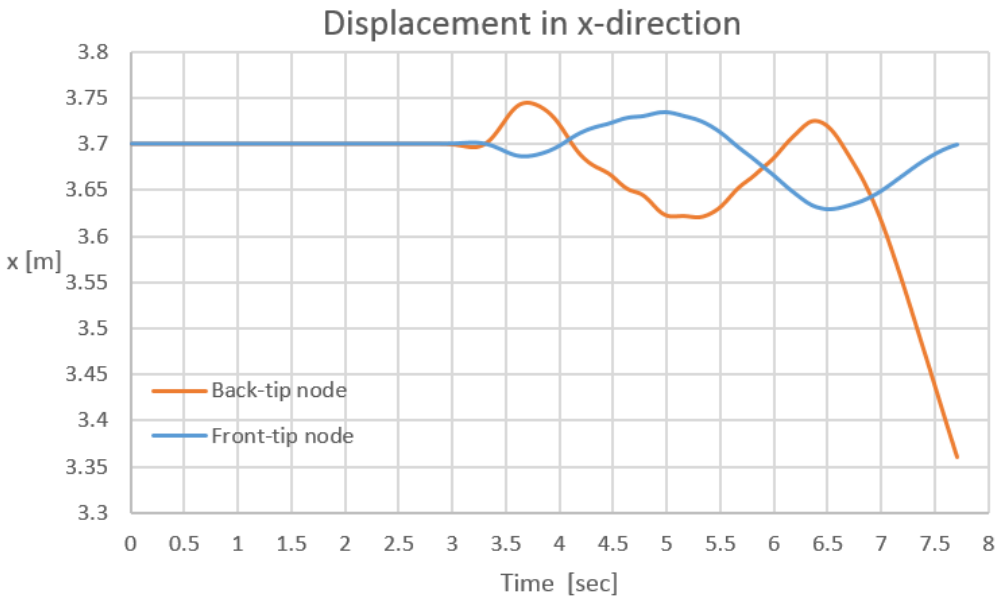

Figure 8-2: Displacement in x-direction of Node 1, segment 1 and node 2, segment 5

It is seen in Figure 8-2 how the anchor starts to tilt after 3sec. It is observed in the visualization tool in RIFLEX that the vertical chain segment starts to oscillate in the horizontal direction as the time goes on. The wave-pattern disperse through the segment from the top and reaches the anchor after approximately 3sec. This is when things start to happen in the plot above. The tilt angle at seabed touchdown is calculated to 1.11°. This is considered to be a small angle. As mentioned in Section 3.2.3, angles less than five degrees are accepted. The low tilt angle is comparable to the Gjøa installation where both anchors were installed with angles less than two degrees. It can therefore be argued that the horizontal force from the mooring line has a minor influence on the anchor trajectory and its tilt angle. This was also concluded in the small scale test (1:25), Trondheimsfjord test and Troll field test (1:3) (Jon Tore Lieng et al., 2010). It was here observed that the chain configuration only had a marginal effect on the anchor behavior during the drop phase for a travel distance less than six times the anchor length. This is also confirmed by the straight vertical trajectory of the anchor model. The x-coordinate of the anchor tip is closely to constant during the drop. All these observations clearly show that the vertical forces are dominating the system behavior. This is as expected due to the large anchor weight.

The mooring line is still slack when the anchor hits the seabed which means that tension from the mooring line is not slowing the anchor down. This implies that the vertical resistance components probably are the reason for the low speed. These forces are tuned by the tangential drag coefficients. As mentioned in Section 5.4, the drag coefficients found in the DNV-OS-E301 can only be used as a rough estimate. Since the anchor speed obtained from the RIFLEX

simulation was significantly lower than expected, decreasing the tangential drag coefficient of the chain could improve the system performance.

8.1.2 Dynamic Mooring Line Behavior

The dynamic behavior of the chain is analyzed by investigating snapshots during free fall. Snapshots for the first two seconds after release are plotted in Figure 8-3 with intervals of 0.2 sec. The gray circle at the top of each snapshot is the static equilibrium position of the connector between installation wire and mooring line (release node). This point is displayed to show the relative distance between the release point and the top of the chain for all snapshots. The coordinates of this point are x=3.7m, y=0m and z=-368.5m. The plotted chain section in the first snapshot is 20m long.

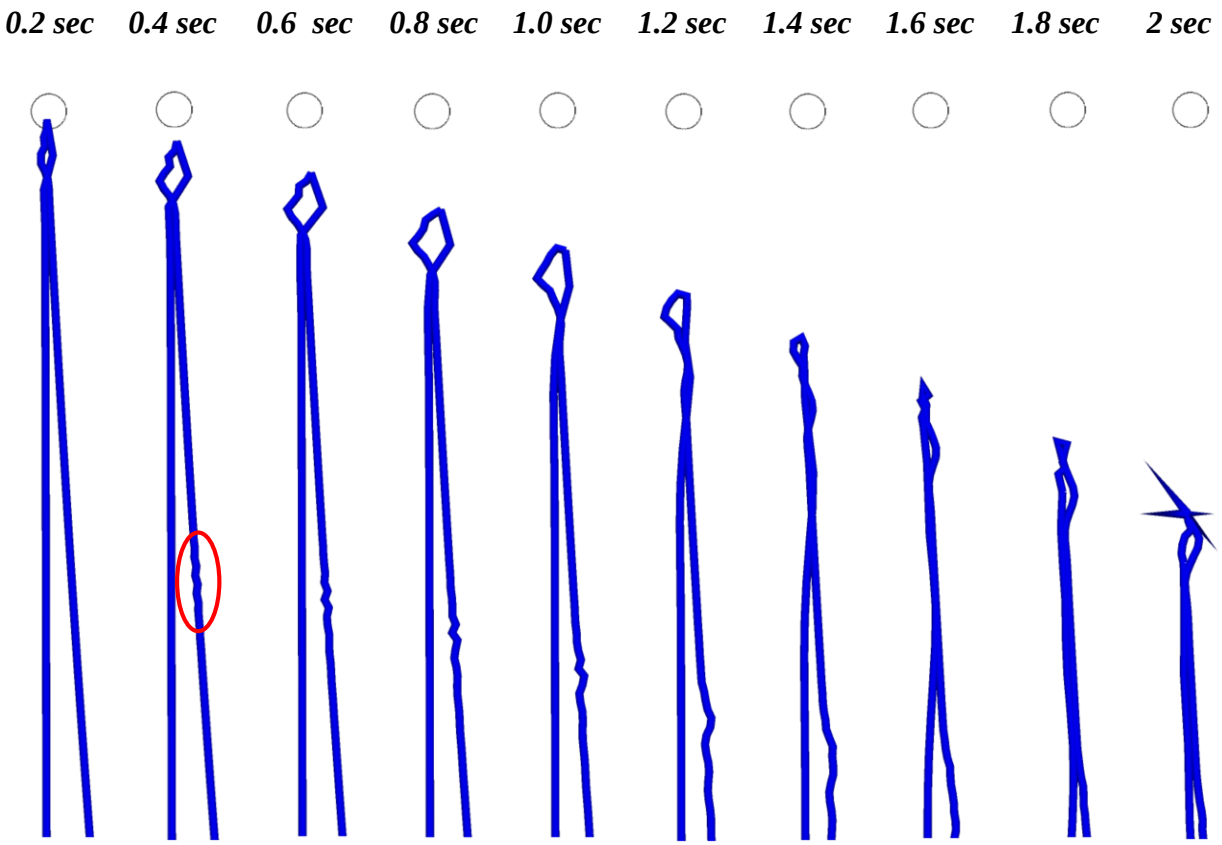

Figure 8-3: Snapshots of the Chain After Anchor Release.

In section 5.4 it is described how the tension in the mooring line loop is lost after anchor release. This effect can be seen already at T=0.4sec inside the red circle in Figure 8-3. The chain deviates from a smooth curved line and has a tendency to form a zigzag pattern. This implies a loss of geometric stiffness. The zig-zag pattern gets more and more disordered as the time goes on.

It can be seen how the elements in the upper end of the chain in Figure 8-3 gets twisted right after release. The twisting gets more significant during the first four seconds, hereafter it

stabilizes. This is shown inside the red circle in Figure 8-4. Twisting of the chain is unwanted. It can, as explained in Section 5.4, cause fatigue failure due to out of plane loading if a knot is present after installation and tensioning of the mooring line. The extreme twist behavior presented in Figure 8-3 does not follow general laws of physics. RIFLEX is a numerical tool and therefore not able to describe the exact behavior of each small element. The program can describe the overall behavior of the mooring line. The behavior observed in RIFLEX may be artificial since a low value for the bending stiffness is applied. It can be seen how the chain loop segment crosses the vertical chain segment. RIFLEX is not able to apprehend when an element hits another element in the same line. The elements just pass straight through each other.

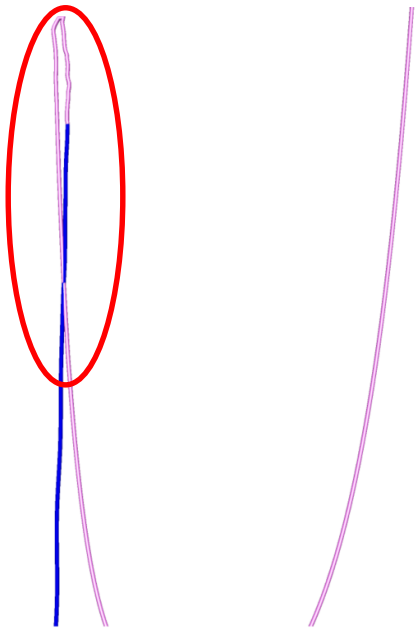

Figure 8-4: Dynamic Simulation, Stabilization with a twist, h=500m, t=4 sec.

It is observed in the dynamic visualization plot that the length of the vertical chain segment increases as the anchor approaches the seabed. More and more chain from the chain loop will follow the trajectory of the anchor (the pink part of the vertical line in Figure 8-4), increasing the vertical extent of chain behind the anchor. The pink part of the vertical chain in Figure 8-4 is approximately 6.5m. This additional vertical chain will give a contribution to the tangential chain drag forces.

In order to get a better overview of how the different segments affect the system, two additional models are made. One model includes the vertical chain segment and the other one is only the anchor. These models are described in the following sections.

8.2 Vertical chain model

This model is identical to the Mooring Line Model, both with respect to input parameters and components, except that the mooring line is removed to investigate the influence of it. This configuration was proposed as drop configuration in the Geotechnical report for the Gjøa field (Deep Sea Anchors, 2009). The model is shown in Figure 8-5.

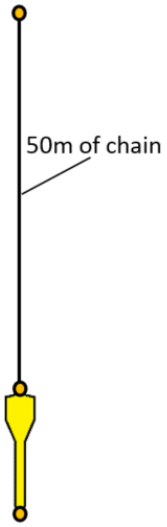

Figure 8-5: Vertical chain model.

8.2.1 Touchdown Velocity and Tilt Angle

The vertical displacement curve given in Figure 8-6 resembles the curve for the Mooring Line Model, except that touchdown occurs earlier.

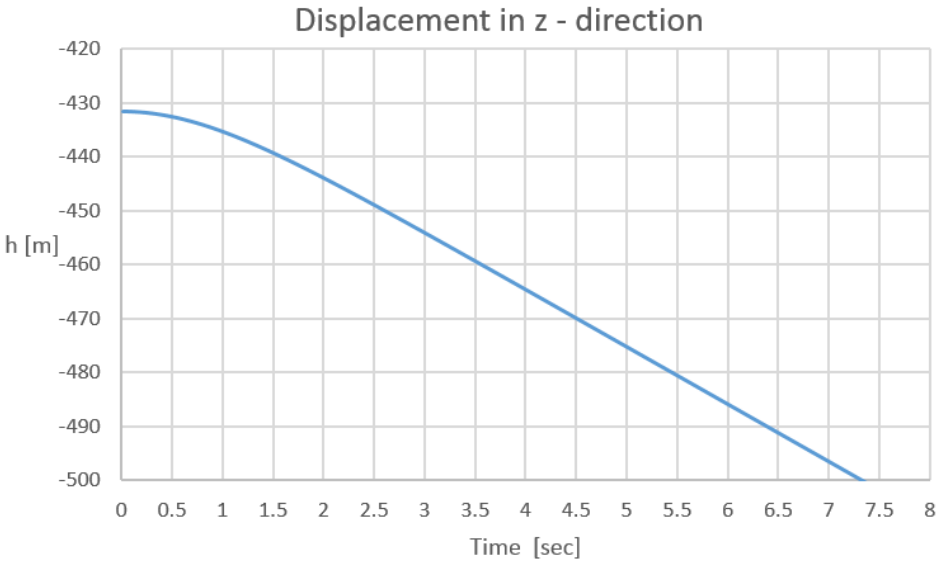

Figure 8-6: Displacement in the z-direction of Node 2, Segment 5. Vertical Chain model.

The calculated touchdown velocity and tilt angle are listed in Table 8-3.

Table 8-3: Output from Vertical Chain Model.

Parameter	Symbol	Value	Unit
Time of Touchdown	T_{TOUCH}	7.3	Sec
Touchdown velocity	V_{TOUCH}	10.6	m/sec
Tilt angle	θ	0	Degrees

In Figure 8-6, the anchor is observed hitting the seabed at approximately T =7.3sec, which is just a slightly shorter time compared to the Mooring Line Model. However, the small difference of 0.2sec results in a slightly increased terminal velocity (10.6m/sec). The slope is constant from approximately T=1.7sec, implying that terminal velocity is achieved. Increasing the drop height would therefore not increase the touchdown velocity. Removing the permanent mooring line obviously gives a negligible effect on the touchdown velocity. This implies that the resistance on either the chain or the anchor elements is too large.

The tilt angle is observed to be 0^{o} from start to finish due to the absence of the chain loop and permanent mooring line. Hence, no horizontal force is trying to tilt the anchor. This is also verified by the vertical chain segment which is observed to follow the straight vertical trajectory of the anchor. The anchor hits the seabed without any change in horizontal position.

8.2.2 Dynamic Mooring Line Behavior

The vertical shape of the chain does not collapse during free fall. This is due to the heavy weight of the anchor dragging the chain downwards and the friction drag on the mooring chain which gives an upward directed force. These opposite directed forces produce a small tension in the chain causing a non-zero geometric stiffness. This is shown in Figure 8-7. The axial tension for three different nodes in the vertical chain segment is plotted as a function of time in the figure. At the time instant right after anchor release, the tension is zero in the top node of the chain segment. This is represented by the blue curve. The bottom node of the chain (green curve) feels the largest tension because friction forces from the total chain length are acting at this point. The red curve represents the center node of the chain segment (25m from each end).

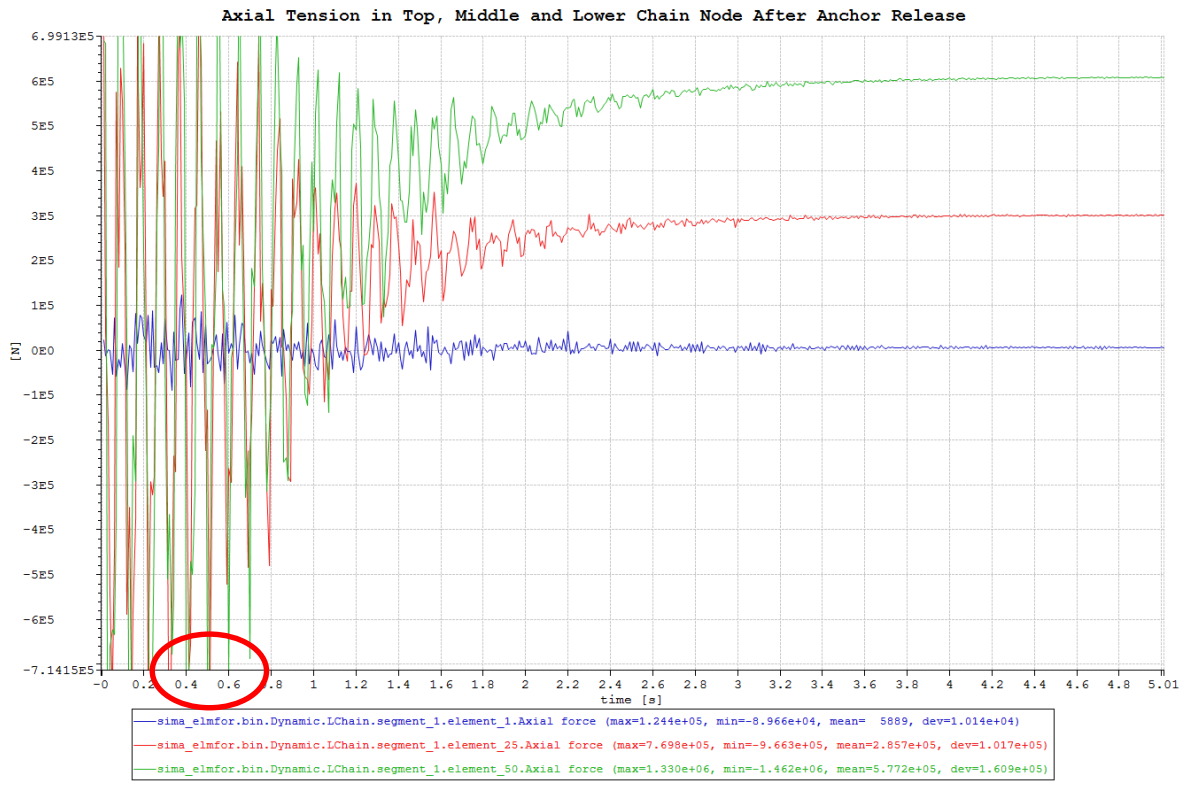

Figure 8-7: Axial Tension in Top, Middle and Lower Chain Node After Anchor Release.

As seen in Figure 8-7, the tension forces seem to stabilize after 3sec. This is 1.3sec after terminal velocity is achieved (Figure 8-6). It can be seen that the tension varies from zero at the top node to 600N at the bottom node. The stabilized tension in the center node is exactly half the tension in the bottom node. This implies that the tension varies linearly over the chain length.

The force amplitude oscillations during the first seconds in Figure 8-7 are most likely axial elastic oscillations caused by stored elastic energy that is released when the anchor is dropped and tension in the chain disappears. The decay of the high oscillating force amplitudes is due to damping forces in the system. It is observed that all maximum force values for the three nodes occurs at the same time. The fluctuations therefore represents a standing wave. The frequency of the oscillations is found by the well known relation between period and frequency given in Equation (8-1). The force period T (time between two peaks) is read off inside the red circle to be approximately 0.1sec.

$$\omega = \frac{2\pi}{T} \tag{8-1}$$

Using Equation (8-1) the frequency is calculated to 62.83 rad/sec. This frequency should be equal to the eigenfrequency obtained from the analytical expression for axially oscillating rods (Larsen, 2014b) given in Equation (8-2).

$$\omega_{0,n} = \left(n - \frac{1}{2}\right)\frac{\pi}{l}\sqrt{\frac{E}{\rho}} \tag{8-2}$$

where n is eigenfrequency number, l is the length of the vertical chain, E is the modulus of elasticity for the chain and ρ is the density of the chain material.

Equation (8-2) is valid for a beam with one free and one fixed end. The anchor is pulling the chain downward with such a significant force that the lower end of the chain can be assumed fixed relative to the vertical chain segment. The lowest eigenfrequency is obtained by n equal to 1. The segment length l is set to 50m. The modulus of elasticity (E = 5.49e+10 N/m^2) and density (ρ = 13941.97301 kg/m^3) are based on the mass coefficient μ_{CHAIN} axial stiffness EA_{CHAIN} and cross-sectional area A_{CROSS} of the chain given in Section 5.4. E and ρ are calculated using Equation (8-3) and (8-4).

$$E = \frac{EA_{CHAIN}}{A_{CROSS}} \tag{8-3}$$

$$\rho = \frac{\mu_{CHAIN,AIR}}{A_{CROSS}} \tag{8-4}$$

The eigenfrequency from of Equation (8-2) is calculated to 62.36rad/sec. The two eigenfrequencies calculated by Equation (8-1) and (8-2) corresponds very well with each other. Hence, the assumption of axial elastic oscillations is supported by the analytical formula, and may be considered as verified.

The anchor model investigated in this section confirms the assumption from Section 8.1.1 that the mooring line hanging on the side of the anchor has a negligible effect on the terminal velocity and tilt angle. As mentioned in Section 8.1.2, the vertical chain segment gets longer as the anchor approaches the seabed. This increased length is obviously not large enough to give a significant contribution to the total friction and drag forces on the chain. This is due to the negligible increase in touchdown velocity. The velocity should have been decreased if the vertical extension in Section 8.1.2 had influence on the resistance.

8.3 Only Anchor Model

In this model, only the anchor is present. The intention with the model is to see how the anchor is affected by the vertical chain segment with respect to the resistance and to compare the touchdown velocity with results from the Gjøa field installation. The anchor is released from the same height as in the two previous models. All input parameters are unaltered. The output is presented in Table 8-4.

Table 8-4: Output from Only Anchor Model.

Parameter	Symbol	Value	Unit
Time of Touchdown	T_{TOUCH}	4.5	Sec
Touchdown velocity	V_{TOUCH}	26.2	m/sec
Tilt angle	θ	0	Degrees

8.3.1 Touchdown Velocity and Tilt Angle

No horizontal forces are present, and the tilt angle is therefore still 0°. The vertical displacement curve is shown in Figure 8-8.

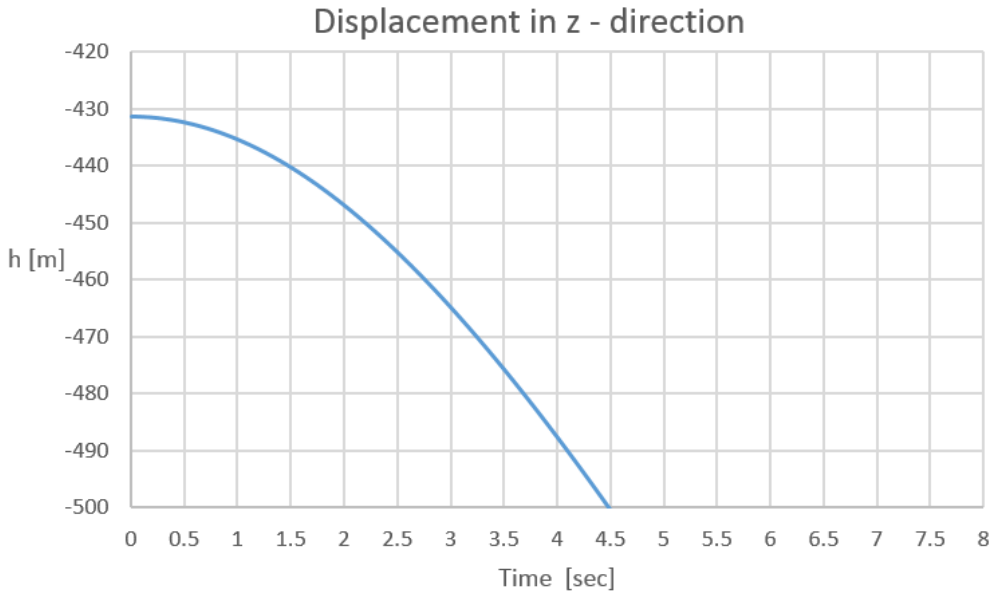

Figure 8-8: Displacement in the z-direction of Node 2, Segment 5.Only Anchor Model.

It can be seen in Figure 8-8 how the slope of the curve gets steeper and steeper until the anchor hits the seabed after approximately 4.5sec. The touchdown velocity is at this point calculated to 26.2m/sec, which shows that the free fall velocity is drastically increased when the chain segment is removed. In the geotechnical design report written ahead of the installation at Gjøa (Deep Sea Anchors, 2009), the anchor velocity was calculated to around 28.5 m/sec when released from approximately 70m. The observed velocities during the actual installation was 24.5m/sec and 27m/sec (Jon Tore Lieng et al., 2010). The velocity obtained from RIFLEX (26.2m/sec) has good agreement with the above mentioned results. The anchor model is simplified and based on several assumptions, therefore, some deviation must be expected. A touchdown velocity of 26.2 m/sec from a drop height around 70 meters can therefore be considered as acceptable. It should be mentioned that the chain dimensions used in this thesis

(D = 142mm) is larger than for the Geotechnical Design Report (Deep Sea Anchors, 2009) (D = 84mm).

By setting the vertical stiffness of the sea bottom to zero and observing where the displacement curve becomes linear, the terminal velocity is found to be approximately 33.3m/sec. This velocity corresponds well with the calculated terminal velocity of 37m/sec for a 75ton DPA in the Gjøa report (Jon Tore Lieng et al., 2010). An acceptable touchdown and terminal velocity means that the element distribution of the anchor and the corresponding drag- and friction coefficients are chosen so that the anchor model gives reasonable results.

Figure 8-9 gives a presentation of the velocity development after anchor drop for the three above mentioned models. Observed time of touchdown (T) and the corresponding touchdown velocity (V) is also given.

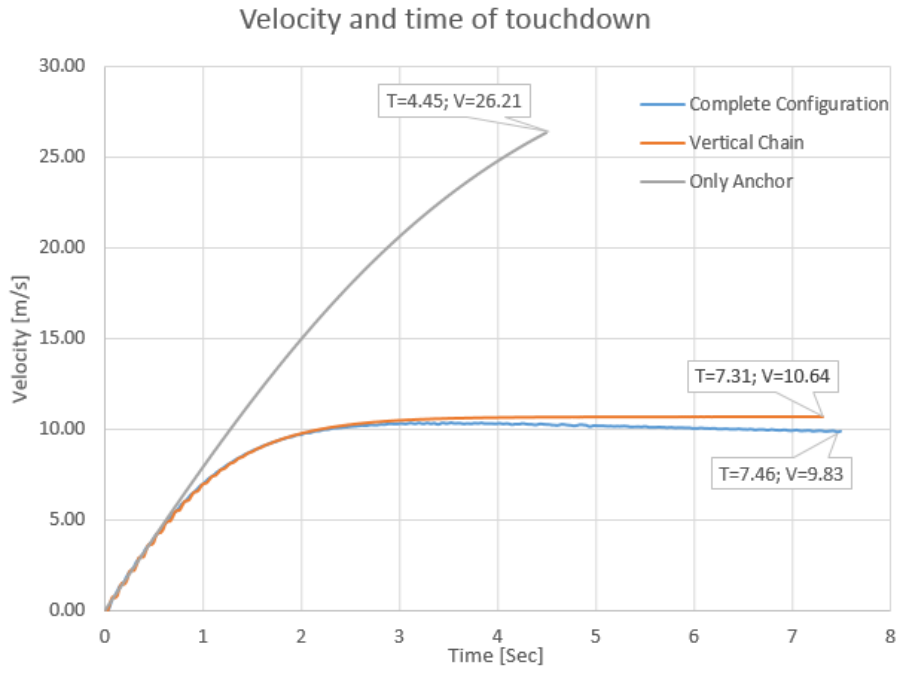

Figure 8-9: Velocity increase during free fall, time of touchdown and telocity.

The small distance between the blue and orange curves in Figure 8-9 illustrates the insignificant resistance contribution from the permanent mooring line on the anchor velocity. The large gap between the gray and orange curves indicates that the resistance in the vertical chain is too large when the tangential chain drag coefficient from DNV is applied. In order to find an acceptable touchdown velocity with the chain attached, the tangential chain drag must be modified.

8.4 Modification of Tangential Chain Drag Coefficient

In Deep Sea Anchors (2009) it is argued that the chain drag is minimal when the whole chain length has a vertical extension behind the anchor. A value of 0.0069 was used for the chain drag coefficient because this value gave a good fit with recorded velocity data from tests performed in the Trondheim fjord. This is significantly lower than the value obtained from DNV. An analysis using the Mooring Line Model is conducted to see the effect of the significantly reduced coefficient.

8.4.1 Touchdown Velocity and Tilt Angle

The drag coefficient given in Table 8-1 is then set to 0.0069. The output parameters are listed in Table 8-5.

Table 8-5: Output from Mooring Line Model with $C_{D,T,CHAIN}$=0.0069.

Parameter	***Symbol***	***Value***	***Unit***
Time of touchdown	T_{TOUCH}	4.4	Sec
Touchdown velocity	V_{TOUCH}	26	m/sec
Tilt angle	θ	0	Degrees

The displacement curve in the z-direction is identical to Figure 8-8 except that touchdown occurs at 4.4sec. It is therefore not plotted again. The results show that reducing the anchor chain drag coefficient from 0.4456 to 0.0069 increases the anchor touchdown velocity from 9.9m/sec to 26m/sec. This velocity is nearly identical to observed anchor touchdown velocity for the Only Anchor Model. This does not agree with expectations. It is believed that including the mooring line with its lateral and tangential drag coefficients will at least decrease the anchor speed to some extent. However, the touchdown velocity agrees with velocities obtained at the Gjøa field installation (See Chapter 3.3) and the model is therefore believed to give a satisfactory description of the velocity vs. drop height. $C_{D,T,CHAIN}$ = 0069 is used in further calculations.

8.4.2 Change in Dynamic Behavior

A comparison of the mooring line configuration for the two tangential drag coefficients is visualized in the snapshots for T = 3sec in Figure 8-10.

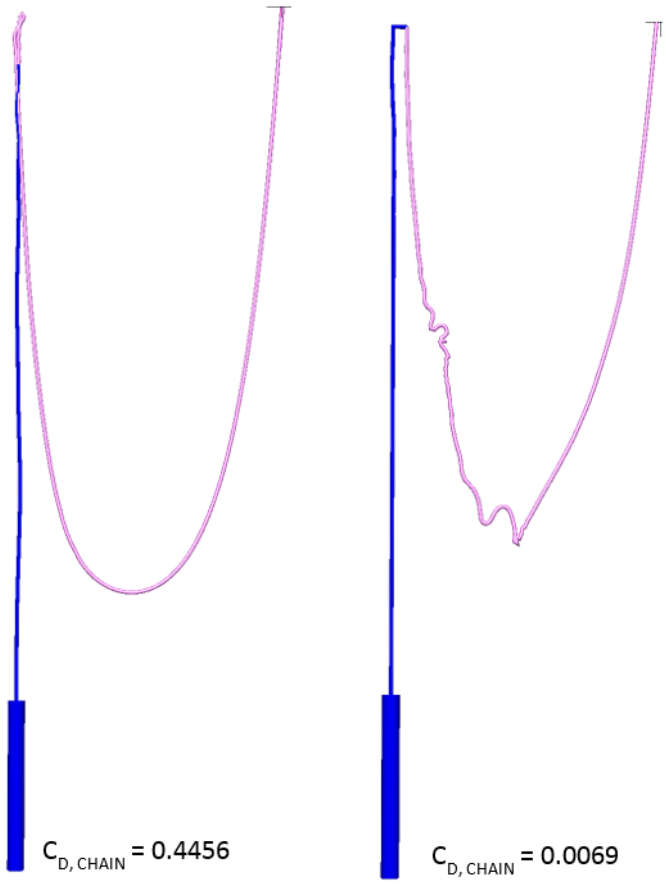

Figure 8-10: Snapshots at T=3sec. Comparison of chain configurations for different chain drag coefficients.

It is observed in Figure 8-10 that the mooring line behavior during free fall is slightly changed. The wave pattern observed in the vertical chain (left side of figure) is no longer existing, the two chain segments do not cross each other and the elements in the chain loop are much more curled (right side of figure). The higher degree of curled sections in the chain loop can be explained by the difference in geometric stiffness, which is governed by the axial tension. Reducing the drag coefficient, reduces the chain resistance. This result in lower axial tension.

The absence of the waveform in the vertical chain (right side of figure) explains why the tilt angle is zero. It is the horizontal forces and oscillations that tilt the anchor. The anchor coordinates in the horizontal plane are constant during the drop, which implies that the anchor falls straight downwards.

9 Influence of Current

In this chapter, current is applied to Model 1 and 2 to examine its effect on the installation. The current profile from Section 6.4 is utilized. The water depth mainly ranges from 500m to 3000m. In Model 1, the static equilibrium position of the wire bottom node (x_{21}, z_{21}) are compared for the cases with and without current. Both horizontal and vertical displacements are considered. In Model 2, the change in horizontal position of the anchor tip during free fall is studied. The tangential chain drag coefficient is set to 0.0069.

9.1 Current on Static Equilibrium

Examples of the two equilibrium configurations (with/without current) used for comparing displacements are presented in Figure 9-1. The current propagates from left to right.

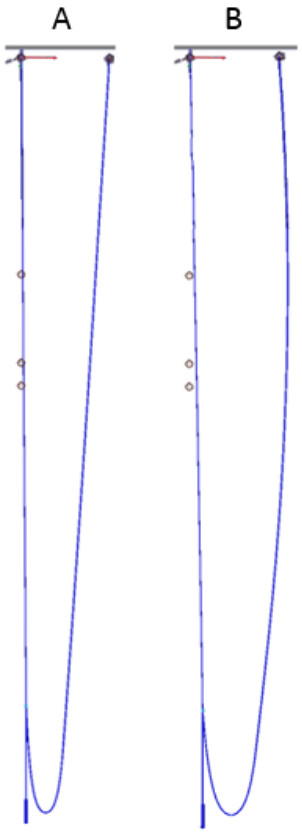

Figure 9-1: Static equilibrium without current (left) and with current (right), h=500m.

By comparing figure A and B in Figure 9-1, it is seen how the fiber section of the mooring line, as well as the wire and chain, is pushed towards right in Figure B. The three grey circles in each figure represents the initial position of the supernodes. One can see how the installation wire is pushed towards right. The chain loop in figure B is wider, which means that elements om the loop has a more horizontal configuration than figure A.

The static equilibrium results from Model 1 is presented in Table 9-1. The water depth ranges from 400-3000m. The shallower depths are included to see the trendline of the displacements around h = 500m in Figure 9-2. All values in the table are given in meters.

Table 9-1: Static equilibrium coordinates for the bottom wire node in Model 1.

	No Current		**Current**		**Displacement**	
h	**X**	**Z**	**X**	**Z**	**ΔX**	**ΔZ**
400	2.8	-268.0	9.2	-267.9	6.4	0.1
425	3.2	-293.1	9.1	-293.0	5.9	0.1
500	3.8	-368.5	8.0	-368.4	4.2	0.1
550	4.3	-418.7	8.2	-418.6	3.9	0.1
750	5.9	-619.6	9.8	-619.6	3.9	0.1
1000	10.8	-870.8	14.8	-870.7	4.0	0.1
1500	19.2	-1373.2	23.6	-1373.1	4.4	0.1
2000	24.6	-1876.0	29.5	-1875.9	4.9	0.1
2500	33.9	-2378.8	39.5	-2378.7	5.6	0.1
3000	44.0	-2881.7	50.4	-2881.6	6.3	0.1

It seen by the small ΔZ-values in Table 9-1 how the vertical displacement position of the lower wire end is nearly unaffected by the current. A variation of 10 cm is negligible. The force exerted by the current is not large enough to cause the wire-end to swing upwards. A variation of 10 cm is negligible.

On the contrary, it is seen by the large ΔX-values in Table 9-1 that current has an effect on the equilibrium position in the horizontal plane. The horizontal position of the node is changed with nearly 4m for all water depths considered. This offset is important to account for during installation in locations with subsea infrastructure.

The current profile is chosen such that the largest velocities are at the upper 400m below mean sea level, hence, the topmost part of the installation wire and mooring line is exposed to the largest current forces. The change in horizontal position as a function of water depth $\Delta X(h)$ for the wire bottom node is plotted in Figure 9-2.

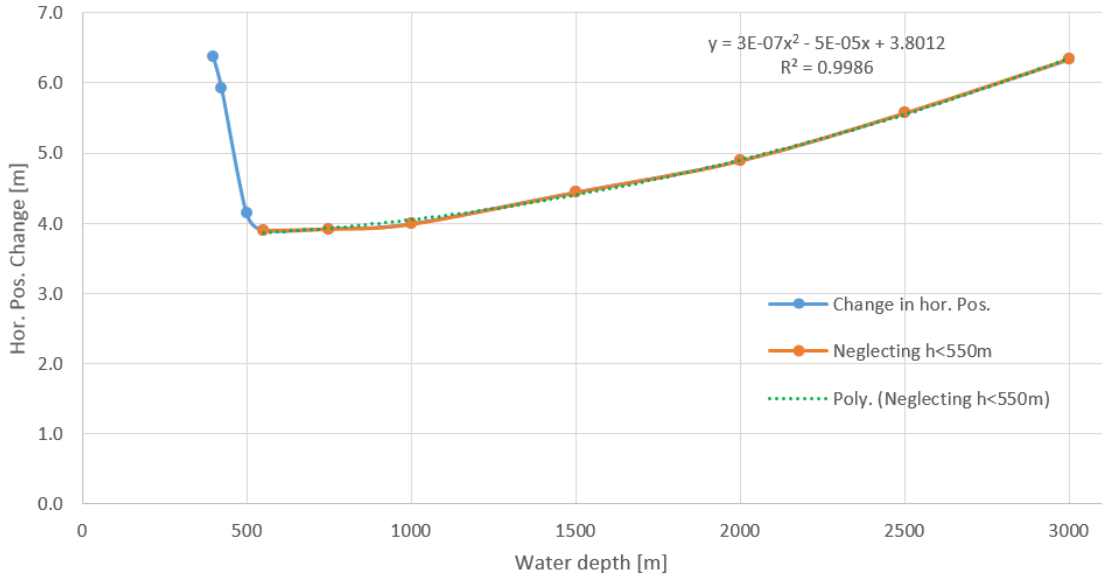

Figure 9-2: Horizontal position of wire bottom end as a function of water depth.

It is observed in Figure 9-2 that the horizontal displacement for h = 500m is higher than for h=1000m. Therefore, some additional water depths are analyzed to give a more precise current investigation around h =500m. Water depths equal to 400m, 425m, 550m and 750m are chosen. It is observed that the current displacement of the wire bottom node increases rapidly for h<500m and varies with a small quadratic slope for depths h>500m. The reason for the rapid displacement increase for h<500m is due to large current velocities over the entire length of the wire. For increasing water depths, the fraction of the mooring line exposed to large current forces decreases. For e.g. a wire length of 3000m, only 13% of the length is exposed to large current velocities. The slope is therefore much lower for increasing depths.

The trendline described with the second order polynomial presented in Equation (9-1) gives a good fit to the RIFLEX output coordinates. The trendline is found by the *Least Square Method*, where R^2 equal to one implies that the polynomial gives a 100% fit to the plotted data. With this equation, horizontal bottom node displacement can be estimated as a function of h for the applied current profile. It is important to remember that this trendline is highly dependent on the input parameters to this thesis, especially the selected current profile, and may therefore not be used for a general case.

$$\Delta X(h) = 3 \cdot 10^{-7} h^2 - 5 \cdot 10^{-5} h + 3.8012 \qquad (9\text{-}1)$$

In Table 9-2 the RIFLEX output is compared to values calculated with Equation (9-1). It is seen that the trendline has a good fit for the original range of water depths, 500-3000m.

Table 9-2: Comparison of horizontal displacement from RIFLEX and trendline formula.

Water depth		Trendline Value	Error
h	**ΔX**	**ΔX_{TREND}**	**$E=\Delta X-\Delta X_{TREND}$**
400	6.4	3.8	2.6
425	5.9	3.8	2.1
500	4.2	3.9	0.3
550	3.9	3.9	0.0
750	3.9	3.9	0.0
1000	4.0	4.1	-0.1
1500	4.4	4.4	0.0
2000	4.9	4.9	0.0
2500	5.6	5.6	0.0
3000	6.3	6.4	0.0

9.2 Current on Anchor During Free Fall

The influence of current during free fall is investigated by a dynamic analysis (Model 2) applying h = 500m and the current profile from Section 6.4. The results show that the x-coordinate of the anchor tip is changed from x = 8.132m at the time of drop to x = 8.217m when the anchor reaches the seabed. A change in horizontal position of 0.085m over a vertical distance of 70m is negligible. It seems like the gravity force of the anchor is so high compared to the current force acting during free fall, that the anchor is barely affected by the current force.

For increasing water depths, the current profile decreases. Between 400m below the mean surface and the sea bottom, the current velocity goes linearly from 0.2m/sec to zero. Hence, for a deepwater installation, the current velocity will be close to zero at the drop position due to the relatively short distance from the sea bottom. Since the current influence on anchor displacement is small for the shallowest water considered, the influence is even more negligible for deeper waters.

Current appears only to affect the static equilibrium configuration before anchor drop due to the long wire and mooring line but has a negligible effect on the dynamical motion during free fall.

10 Variation of Mooring Line Top Node Position

In this chapter, the behavior of the mooring line, vertical chain and anchor is investigated for varying distance between the installation vessels. This corresponds to the horizontal distance between the upper nodes of the installation wire and mooring line. The expected behavior is explained first, and the results are presented thereafter.

10.1 System Behavior

In the analyses, the water depth is set to 500m and the tangential chain drag coefficient ($C_{D,T,CHAIN}$ = 0.0069) from Section 8.4 is applied. The length of the vertical chain length $L_{VERT.CHAIN}$ is set to 50m. The horizontal distance between the upper ends of the installation wire and mooring line is termed X_{DIST}. System behavior is investigated for X_{DIST} equal to 50m, 75m, 100m, 125m, 150m and 170m. X_{DIST} affects the equilibrium position of the anchor when it is hanging in the drop position. By keeping the lengths of the wire and mooring line constant, a larger value for X_{DIST} increases the horizontal component of the force exerted by the mooring line on the connection point between the installation wire and mooring chain. This force is pulling the installation wire, and therefore moves the static equilibrium position of the connection point in the direction of the upper end of the mooring line. The connection point is moved in both the horizontal and vertical direction, but the horizontal displacement is dominating. This is illustrated in Figure 10-1.

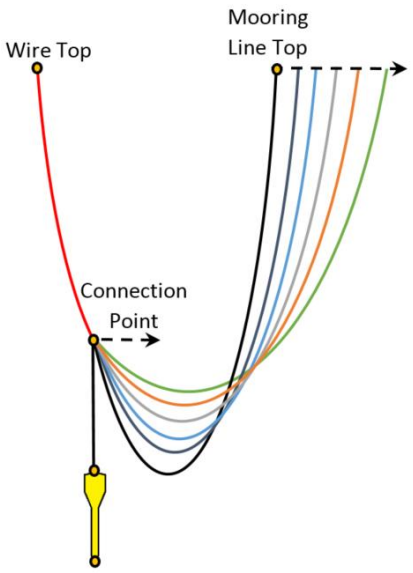

Figure 10-1: Increasing the horizontal distance between the top point of installation wire and mooring line.

Model 1 from Section 6.2 is used to find the new equilibrium positions of the connection point as a function of X_{DIST}. The equilibrium coordinates is found both with and without current. Since the current, described in Chapter 9, turns out to only give significant contributions to the static part of the analysis, it is not applied in the dynamic analyses.

The mooring line configuration, especially the chain loop, may also affect the direction of motion, tilt angle and touchdown position of the anchor after release from the drop position. Figure 10-2 gives a presentation of how the chain loop configuration gets more narrow and deep with a steeper slope for low values of X_{DIST} (Fig. A), while the loop gets wider and the slope more gradual for larger values of X_{DIST} (Fig. B). It is then assumed that the length of the installation wire and mooring line is constant. The configuration of the elements on either side of the bottom point in the loop is more vertical in Fig. A compared to Fig. B. Two random elements (green rectangles) are enlarged and highlighted and in the figure.

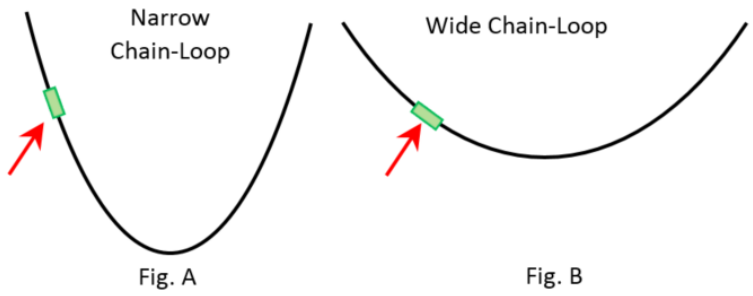

Figure 10-2: Illustration of element orientation in a narrow (A) and wide chain loop (B).

When the anchor is released, the counter force from the installation wire on the mooring line disappear, and it is nothing holding the mooring line, vertical chain and anchor in position anymore. As the segments starts to accelerate downwards, the velocity increases and drag forces become increasingly important. At this point, its weight, buoyancy and drag resistance dominate the behavior of the chain.

10.1.1 Element Drag Forces

To investigate the dynamic behavior of the two configurations in Figure 10-2, the highlighted element in Fig. A and B are studied more in detail in Figure 10-3. The figure is meant as an illustration, and the length of the arrows are not in scale.

The red lines in Figure 10-3 represents velocities, the blue lines are the drag forces and the purple lines are the resultant- and driving forces. The resultant velocity V_R represents the

velocity that the element feels when it is free falling through the water. V_R is decomposed into a lateral- and tangential component, V_L and V_T. The lateral- and tangential drag forces, F_L and F_T, are found using the standard expression for a hydrodynamic force given in Equation (3-3). It is important to remember that F_L and F_T are scaled with respect to different projected areas A_L and A_T, and drag coefficients $C_{D,L}$ and $C_{D,T}$. Due to the significant difference in magnitude of $C_{D,L}$ and $C_{D,T}$, a velocity component can be large and the corresponding force can be low when a small drag coefficient is applied. On the contrary, the velocity can be low but the force large when a large coefficient is used. This may cause the resulting velocity- and drag force vectors $F_{D,R}$ and V_R to point in different directions. This is illustrated in Figure 10-3. The driving force F_{DRIV} is given as

$$F_{DRIV} = mg - B = w_{WATER} \cdot g \tag{10-1}$$

where m is the mass, g is the gravitational acceleration, B is the buoyancy and w_{WATER} is the submerged weight ($m - B/g$).

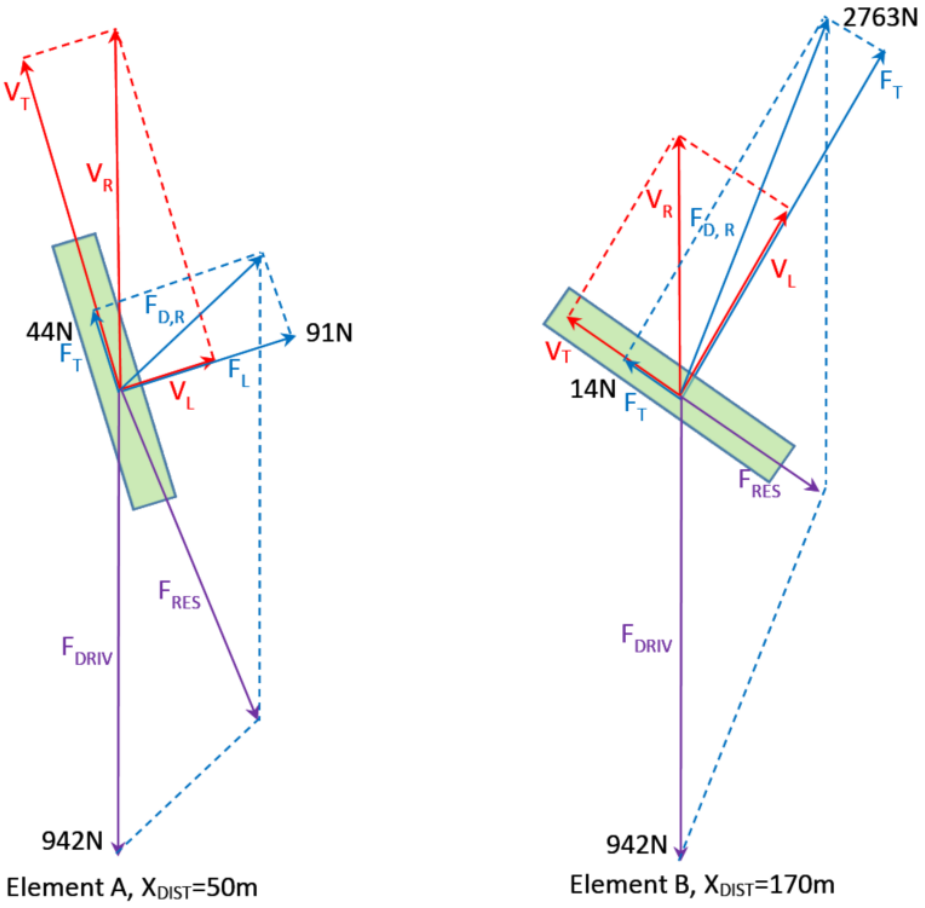

Figure 10-3: Decomposition of velocity and forces on selected elements in configuration A and B.

To illustrate the behavior of Element A and B Figure 10-3, velocities and forces are calculated for a chosen element in both a narrow- and a wire chain loop. All data (velocity and coordinates) are obtained at T=3sec. The models for X_{DIST} equal to 50m and 170m are utilized.

The element between Node 46 and 47 in the mooring line chain segment is selected in both models. The reason for investigating this particular element is that it is observed located outside the curled and twisted chain section during the first three seconds of free fall. Obtaining data from nodes located at a twisted section may give incorrect results due to numerical errors.

The unstretched length of the beam element is 0.25m, and it is located 11.5m from the lower end of the segment. The vertical velocity V_R of the element is calculated from the displacement curve in Node 46 and horizontal displacements are obtained for both Node 46 and 47. The horizontal coordinates of the element-ends are used to calculate the orientation of the element. The anchor tip is then located at approximately z=-465m for both models. This is approximately half the drop height. Figure 10-4 gives a presentation of how the element orientation and velocity components are found.

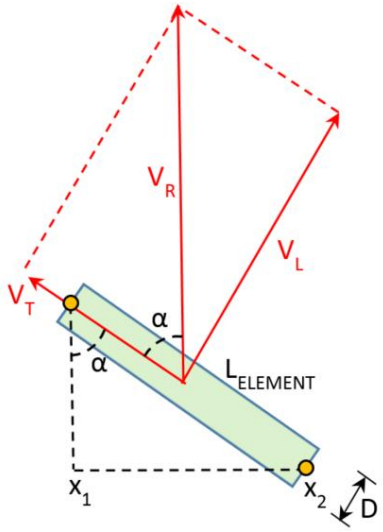

Figure 10-4: Element orientation and velocity decomposition.

By using the geometry relations in Figure 10-4 the orientation, lateral- and tangential velocities are obtained by the following equations.

$$\alpha = \sin^{-1}\left(\frac{x_1 - x_2}{L_{ELEMENT}}\right) \tag{10-2}$$

$$V_L = V_Z \sin\alpha \tag{10-3}$$

$$V_T = V_Z \cos\alpha \tag{10-4}$$

The orientation could also be found using the stretched length with Pythagoras' Theorem and $\alpha = \tan^{-1}\left(\frac{x_2-x_1}{z_2-z_1}\right)$. The difference will be small due to the high axial stiffness and the short length of the elements.

It is important that the parameters in the drag force calculation are defined in the same way as in RIFLEX. Over one element length, the tangential area A_T is equal to A_{CROSS} = 0.032 from Section 5.4. The lateral area A_L is given by $D \cdot L_{ELEM}$ (see Figure 10-4), where D is obtained from Equation (10-5) (MARINTEK, 2014b).

$$D = \sqrt{\frac{4}{\pi} A_{CROSS}} \tag{10-5}$$

D is calculated to approximately 0.2m. The lateral area A_L is then calculated to 0.05m^2 using L_{ELEM} = 0.25m.

The driving force F_{DRIV} is calculated to 942N using the submerged weight from Table 5-1 in Section 5.2. The element orientation, lateral- and tangential velocities and forces obtained from the two models, X_{DIST} =50m and are given in Table 10-1. The values are presented in Figure 10-3.

Table 10-1: Element orientation, velocities and forces obtained at T=3sec for X_{DIST} equal to 50m and 170m

X_{DIST}	V_R	α	V_L	F_L	V_T	F_T
m	m/sec	deg	m/sec	N	m/sec	N
50	19.89	3.4	1.2	91	19.86	44
170	12.9	29.8	6.4	2763	11.2	14

The element in the narrow chain loop (Element A, X_{DIST}=50m) is almost vertically aligned. The tangential velocity component is here almost identical to the vertical velocity V_R. Even though the V_L is only a fraction of V_T, $F_L$are highest. The ratio F_L/F_T is approximately 2.

Element B in the wide chain loop (X_{DIST}=50m) are considerably more tilted with respect to the vertical axis. The vertical velocity V_R is only 12.9m/sec compared to 19.89m/sec for the narrow loop. This implies that the drag forces are significantly larger. This is clearly seen by F_L which is 2763N compared to 91N for the narrow loop. V_T is also here larger than V_L, but the difference is smaller. The ratio F_L/F_T is approximately 197 in this case. It is therefore clearly that elements with a more horizontal configuration are dominated by the lateral forces, and since the corresponding drag coefficient is significantly larger than the tangential, the resistance becomes much higher and the element is slowed down.

For Element B in Figure 10-3 it is observed that the lateral drag force F_L (directed upwards) are larger than F_{DRIV} (directed downwards). If these were the only forces on the elements, the element would move towards the sea surface instead of falling to the sea bottom. The axial tension forces pointing down to the right are not calculated and accounted for. This force would affect the resulting force vector F_{RES}, and give a force equilibrium pointing downwards.

With the drag coefficients applied in this thesis, it can be concluded that more vertical aligned elements have more free falling behavior than more horizontally aligned elements.

10.2 Results from Static and Dynamic Analyses

10.2.1 Displacements Without Current

The horizontal equilibrium coordinates X_{EQ} for analyses without current are presented in Table 10-2 as a function of X_{DIST}, and the vertical equilibrium coordinates Z_{EQ} are presented in Table 10-3. The tables also presents some gradients and step values. All x- and z-coordinates are given in meters. To easily explain the variables in the tables Figure 10-5 is created.

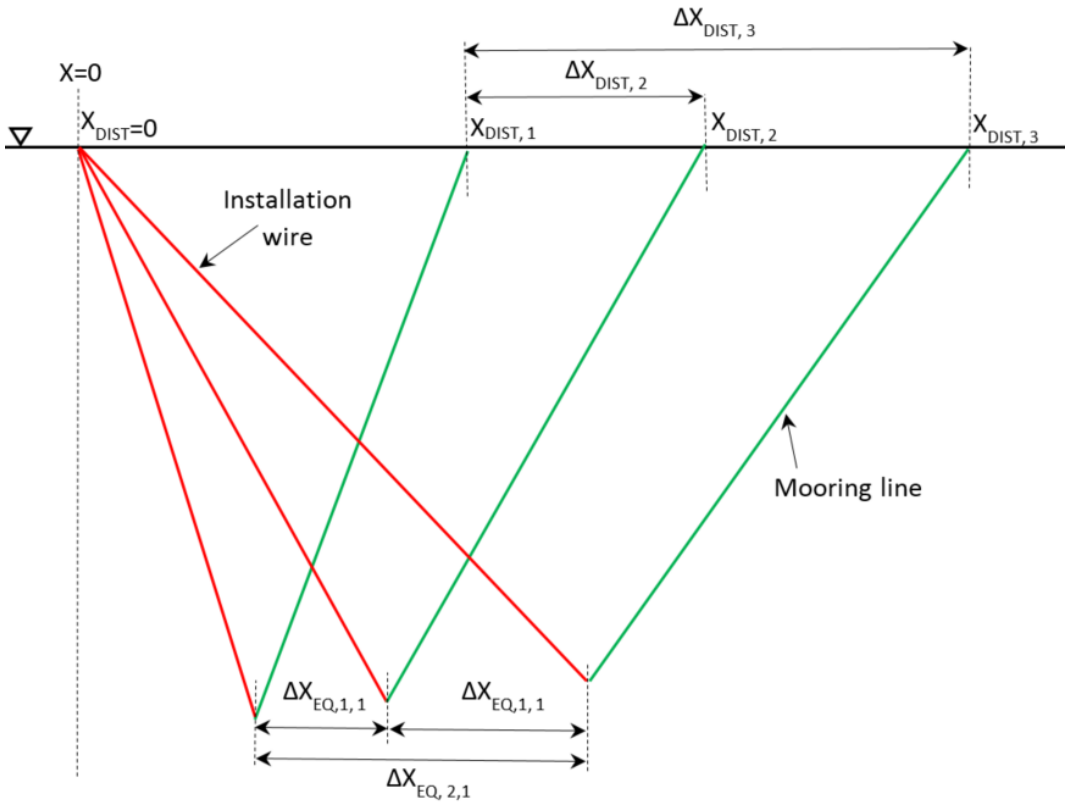

Figure 10-5: Explanation of displacement parameters.

Table 10-2: Equilibrium x-coordinates for the connection point without current.

i	$X_{DIST,i}$	$X_{EQ,i}$	$\Delta X_{EQ,1,i} = (X_{EQ,i} - X_{EQ,i-1})$	a	$\Delta X_{EQ,2,i} = (X_{EQ,i} - X_{EQ,1})$	$\Delta X_{DIST,i} = (X_{DIST,i} - X_{DIST,1})$	$\Delta X_{EQ,2,i} / \Delta X_{DIST,i}$
1	50	3.83					
2	75	6.14	2.3	0.09	2.3	25	9 %
3	100	8.69	2.6	0.102	4.9	50	10 %
4	125	11.52	2.8	0.11	7.7	75	10 %
5	150	14.69	3.2	0.13	10.9	100	11 %
6	170	18.26	3.6	0.18	14.4	120	12 %

Table 10-3: Equilibrium z-coordinates for the connection point without current.

i	X_{DIST}	Z_{EQ}	$\Delta Z_{EQ,i} = (Z_{EQ,i} - Z_{EQ,i-1})$
1	50	-368.46	
2	75	-368.43	0.03
3	100	-368.37	0.06
4	125	-368.29	0.08
5	150	-368.17	0.12
6	170	-368.00	0.17

By comparing the equilibrium coordinates (X_{EQ}, Z_{EQ}) and their variation $(\Delta X_{EQ}, \Delta Z_{EQ})$ for different values of X_{DIST} in Table 10-2 and Table 10-3, it is seen that the horizontal displacement is clearly dominating. This is as expected. For the largest X_{DIST} value, the horizontal coordinate $(\Delta X_{EQ,2,i})$ is 14.4m while the maximum vertical change $(\Delta Z_{EQ,i})$ is less than 0.2m. The change in vertical direction is therefore negligible and not discussed further.

The slope a of the displacement curve in Table 10-2 is calculated as a constant value within each interval. It is expressed as $\Delta X_{EQ,1,i} / \Delta X_{DIST,i}$, where $\Delta X_{EQ,1,i}$ and $\Delta X_{DIST,i}$ are the change in X_{EQ} and X_{DIST} , between analysis number "i" and the previous "i-1" (See Figure 10-5) .This calculation is illustrated in Figure 10-6.

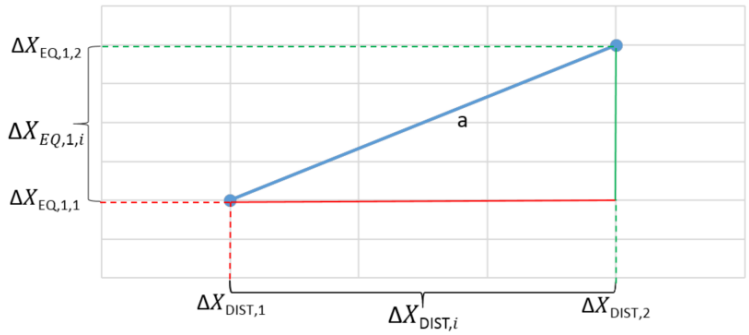

Figure 10-6: Illustration of the displacement slope, a.

The increasing values for the slope a in Table 10-2 implies that the displacement X_{EQ} is a nonlinear function of X_{DIST}. This is seen by the curve in Figure 10-7, where the horizontal equilibrium coordinates X_{EQ} are plotted as a function of X_{DIST}. It is observed how the curve gets steeper for increasing X_{DIST}. This nonlinear shape is expected due to the nonlinear equation describing the relation between force and displacement in a catenary system.

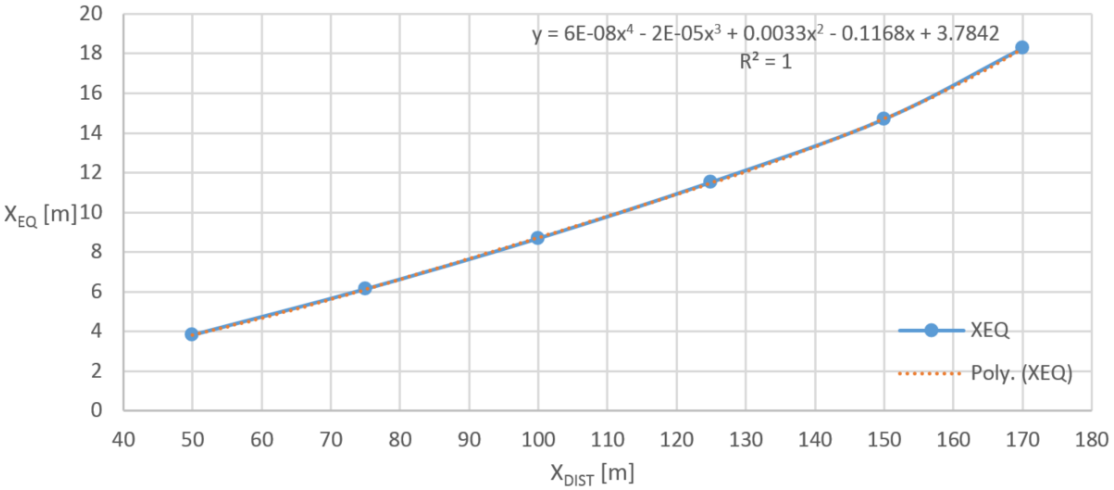

Figure 10-7: Plot of X_{EQ} as a function of X_{DIST}.

The expression given in the top of Figure 10-7 is the trendline expressed by a fourth order polynomial found with the same method as in Section 9.1. The trendline is plotted as the orange, dotted line. For a certain value of X_{DIST}, it is possible to estimate the equilibrium position of the anchor in the horizontal plane with respect to the position of the top node on the installation wire. It is, once again, important to remember that the trendline expression is highly case-dependent. The segment's physical dimensions and stiffness terms determine the behavior of the system.

The ratio $\Delta X_{EQ,2,i}/\Delta X_{DIST,i}$ is also calculated. This ratio represents the change in equilibrium coordinates over the change in horizontal distance between the wire and mooring line top end, measured from the initial positions of $X_{EQ,1}$ = 3.83m and $X_{DIST,1}$ = 50m (See Figure 10-5). The ratio ranges from 9-12%, which implies that the trendline curve of the equilibrium coordinates increase with a higher order polynomial.

To illustrate the effect of X_{DIST} on the static equilibrium configuration, the static equilibrium configuration for X_{DIST} = 50m and 170m is shown in Figure 10-8.

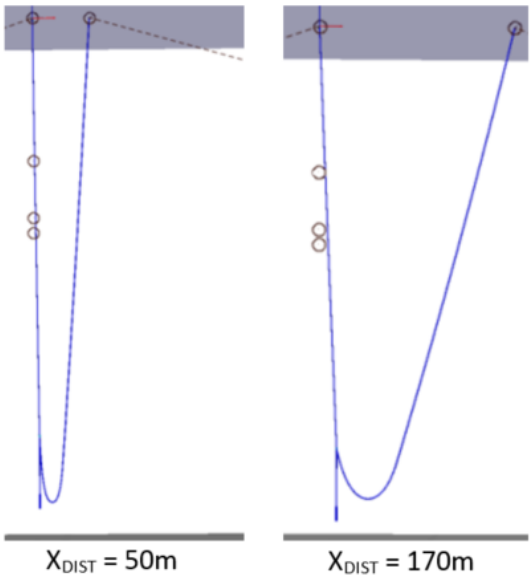

Figure 10-8: Static equilibrium condition for h =500m, X_{DIST} = 50m and 170m.

10.2.2 Displacements due to Current

To compare the cases with/without the influence of current equilibrium coordinates for both cases are given in Table 10-4.

Table 10-4: Equilibrium x- and z-coordinates for the connection point including current.

X_{DIST}	X_{EQ}	$X_{EQ,\,Current}$	$\Delta X_{EQ,\,Current}$	Z_{EQ}	$Z_{EQ,\,Current}$	$\Delta Z_{EQ,\,Current}$
50	3.8	8.0	4.15	-368.46	-368.39	0.07
75	6.14	10.39	4.25	-368.43	-368.33	0.10
100	8.69	12.99	4.30	-368.37	-368.25	0.12
125	11.52	15.83	4.31	-368.29	-368.13	0.16
150	14.69	18.99	4.30	-368.17	-367.97	0.20
170	18.26	22.53	4.27	-368.00	-367.77	0.23

The change in coordinate, when current is applied, is nearly constant for all values of X_{DIST} in Table 10-4. As an example: For the minimum and maximum value of X_{DIST}, 50m and 170m, the displacement due to current $\Delta X_{CURRENT}$ ($X_{EQ,CURRENT}$-X_{EQ}) is equal to 4.15m and 4.27m, respectively. This small difference is negligible. An approximate mean value of 4.3m is found from the table. It should be mentioned that this value is only valid for the water depth considered (500m). It is seen that the vertical displacement due to current is small and is still negligible.

10.2.3 Mooring Line Configuration During Free Fall

Snapshots of the mooring line during free fall are taken for X_{DIST} equal to 50m and 170m to give a good presentation of the dynamic behavior. Figure 10-9 presents snapshots of the mooring line during free fall for X_{DIST} = 50m are, while Figure 10-10 shows snapshots for X_{DIST} = 170m. No interesting observations are made during the first second of the simulation. Therefore, the snapshots are plotted from 1.0sec after anchor release, with intervals of 0.4sec up 4.2sec after drop. The circle in the top of the figures represents the anchor release point. In snapshot 3.4sec, 3.8sec and 4.2sec, the view is moved down in order each time to show the interesting section of the mooring line. Hence, the release point is outside the view in these snapshots. If a closer comparison of the snapshots in Figure 10-9 and Figure 10-10 is desired, a side by side presentation of the snapshots could be found in APPENDIX E.

1.0 sec	1.4 sec	1.8 sec
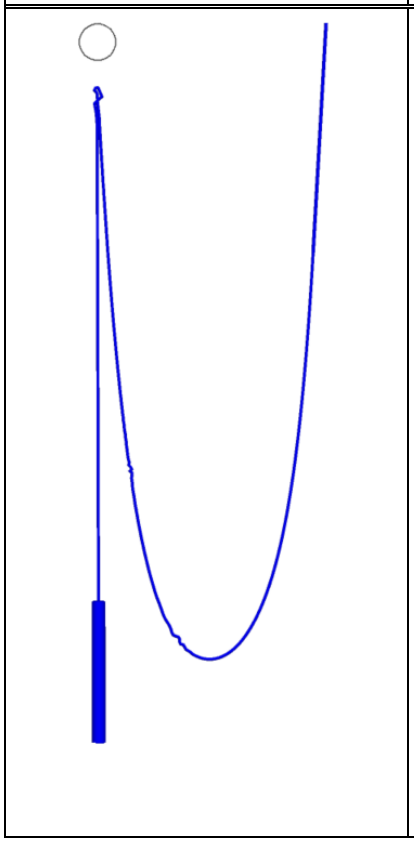	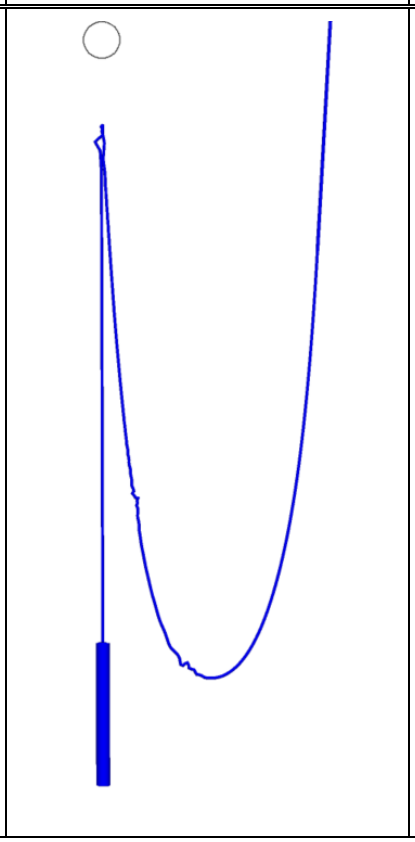	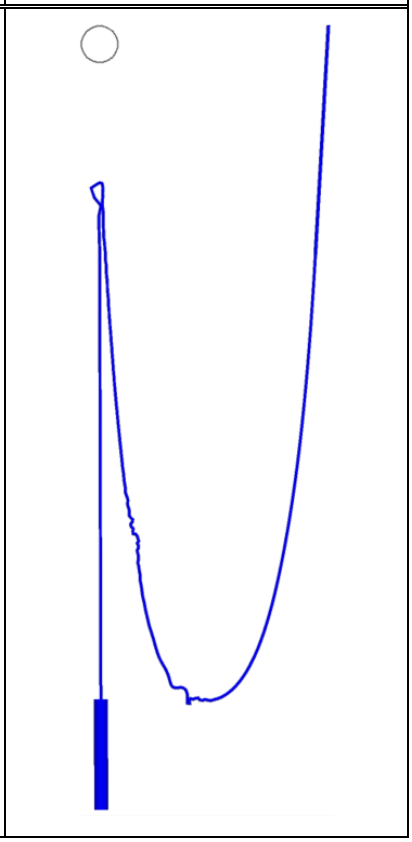

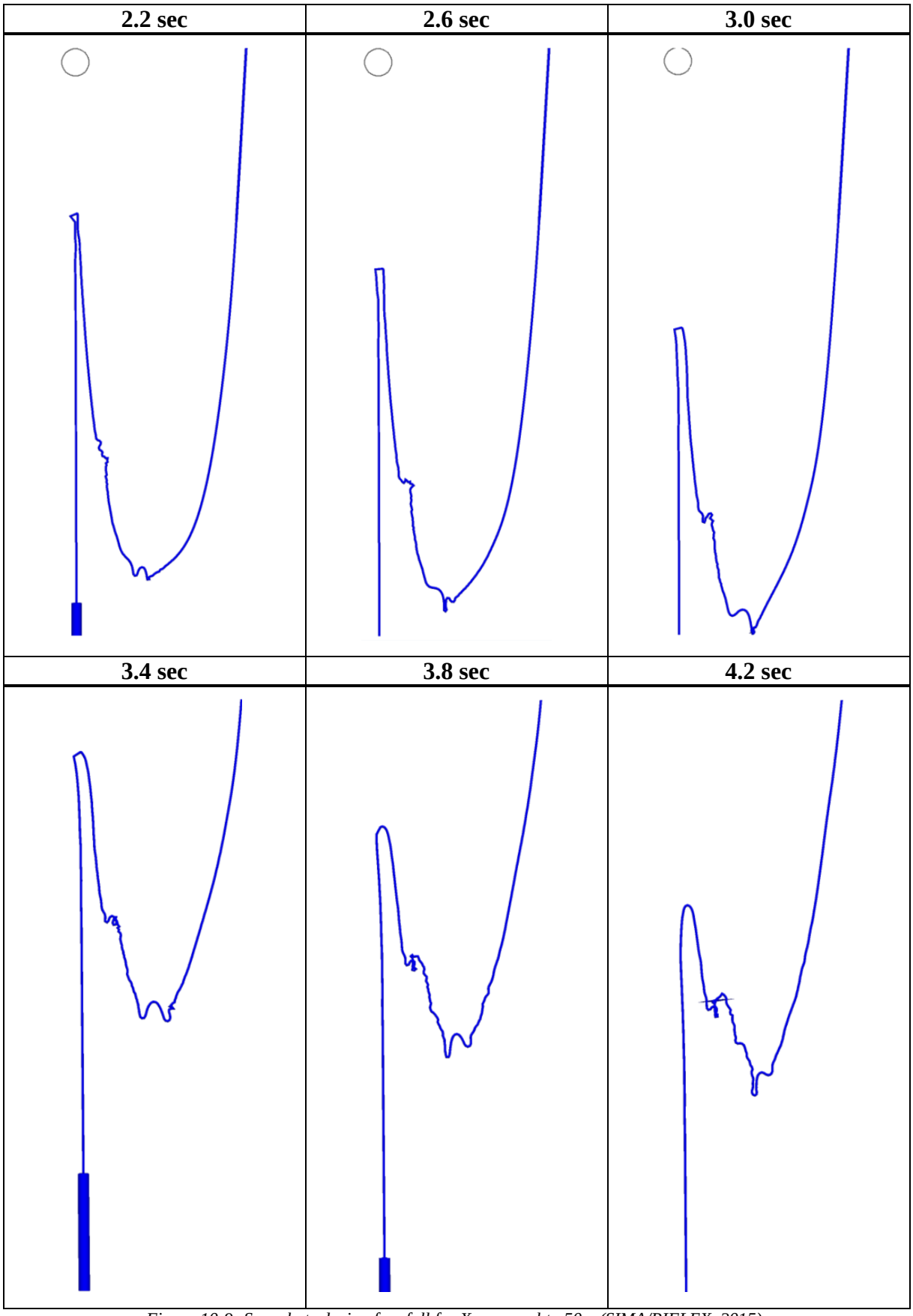

Figure 10-9: Snapshots during free fall for X_{DIST} equal to 50m (SIMA/RIFLEX, 2015).

It is clearly seen in Figure 10-9 that for X_{DIST} = 50m the slope of the chain loop is quite steep. In the majority of the chain loop, the chain elements therefore has a vertical extension which implies that tangential velocities are dominating. Since the tangential drag coefficient is small, in combination with low activated lateral velocities, the elements are exposed to small drag forces as observed in Figure 10-3. The chain in the snapshots above is observed to fall with just a slightly lower speed than the anchor.

The chain loop is observed to get more and more curled as the time goes on. This is due to the lack of geometric stiffness, explained in Section 5.5, occurring when axial tension is lost at the time of anchor release. The low friction forces on the elements caused by the low lateral drag forces only give a small tension in the line. The geometric stiffness is then not sufficient to keep the line slope smooth.

The snapshots of the mooring line during free fall for X_{DIST} equal to 170m are presented in the following figure.

1.0 sec	**1.4 sec**	**1.8 sec**
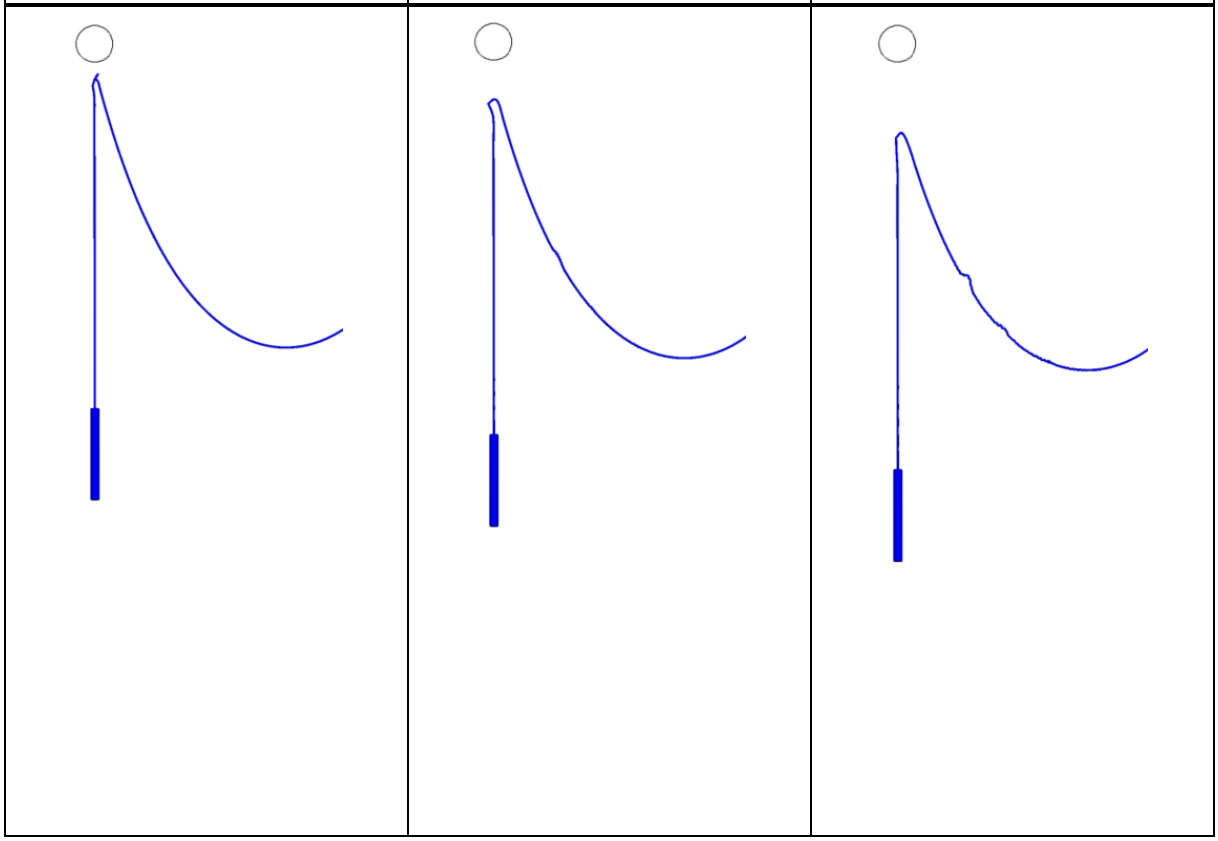		

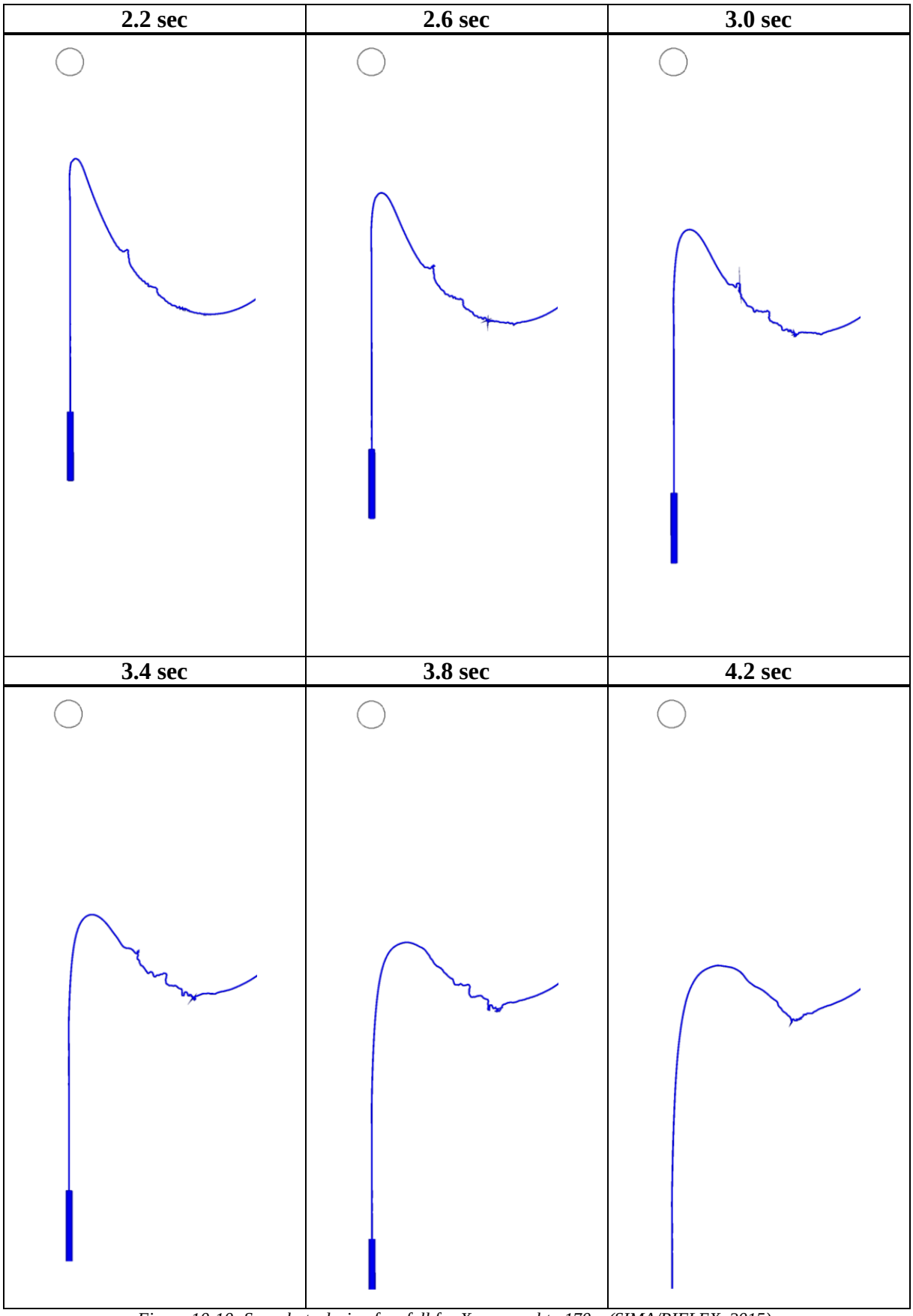

Figure 10-10: Snapshots during free fall for X_{DIST} equal to 170m (SIMA/RIFLEX, 2015).

It is observed in Figure 10-10 that the slope of the chain loop is more gradual compared to Figure 10-9. This means that the elements in the loop have a more horizontal orientation. This is expected since the length of the mooring line is constant, and the line is stretched in the horizontal direction. As the anchor is falling down, the tangential drag forces increase. The scenario is then equal to the Element B in Figure 10-3 where the chain is clearly dominated by the lateral drag forces. The velocity of the anchor is then higher than for the mooring line, and the free-falling behavior of the line is limited.

The chain loop in these snapshots is seen to be significantly less curled. An increase in axial stiffness is clearly seen by comparing the snapshots for 3.8sec and 4.2sec because the chain is much less curled in the last snapshot. A larger part of the chain in the mooring line is dragged behind the vertical chain, which creates a certain tension in the line. This increases the geometric stiffness. The limited free fall behavior due to the high drag resistance combined with geometric stiffness in the chain gives a smoother mooring line configuration. The increased axial tension is confirmed in Figure 10-11, where the time series of the axial tension for a chain element in the mooring line (Element 20) is plotted. The selected element is chosen based on an adequate distance from the vertical chain segment (5m). The blue curve represents the time series obtained from RIFLEX, and the orange curve is the trendline described by a third order polynomial. The curve fit is not optimal, but the intention of the trendline is just to show the tendency of how the axial tension increases with time.

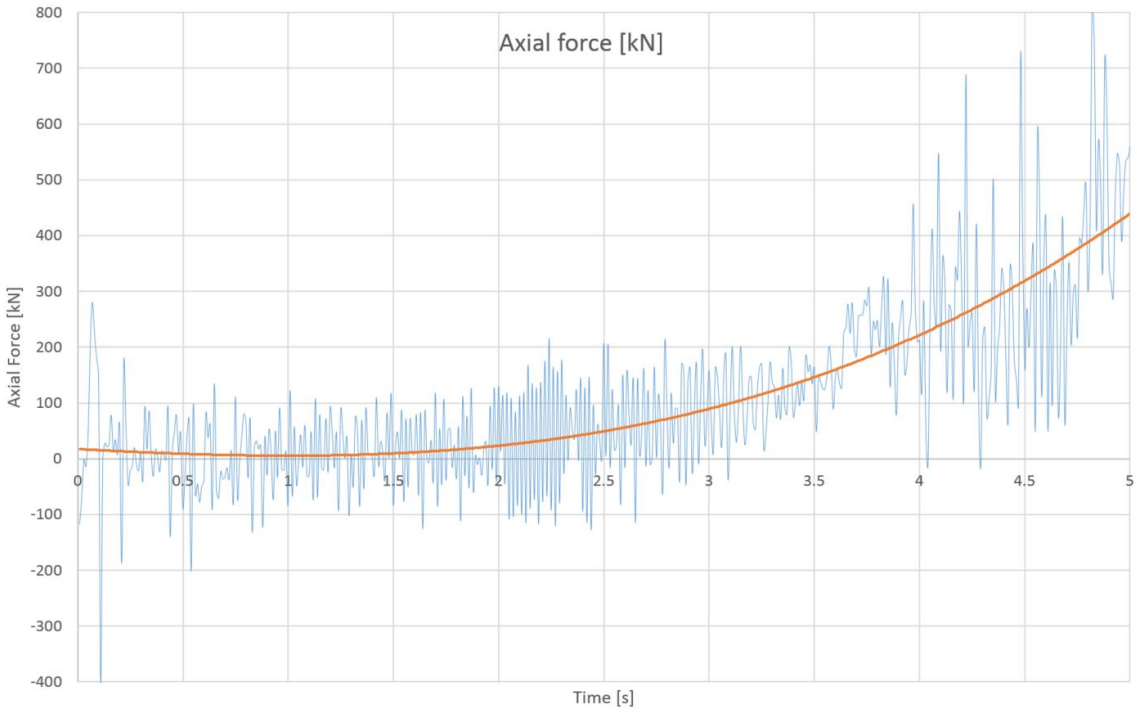

Figure 10-11: Axial force in Element 20, Segment 1 (chain), Mooring line.

It is seen how the axial tension in the element starts to increase after approximately 2sec and continues to rise even after the anchor hits the seabed at 4.4sec. The oscillating force amplitudes is due to numerical problems (C. M. Larsen, 2015). The oscillations do not represent real force variations because the frequency is very high.

Figure 10-12 presents snapshots taken at seabed touchdown (T = 4.4sec) after anchor release for X_{DIST} requal to 50m and 170m, respectively. The lower end of the anchor is then positioned approximately 1m and 2.5m from the seabed implying that the anchor is falling slightly faster for X_{DIST}=50m. The intension of the figure is to show the difference in vertical extension of the chain segment for the two cases. The original vertical chain is marked with blue, while the permanent mooring line is pink.

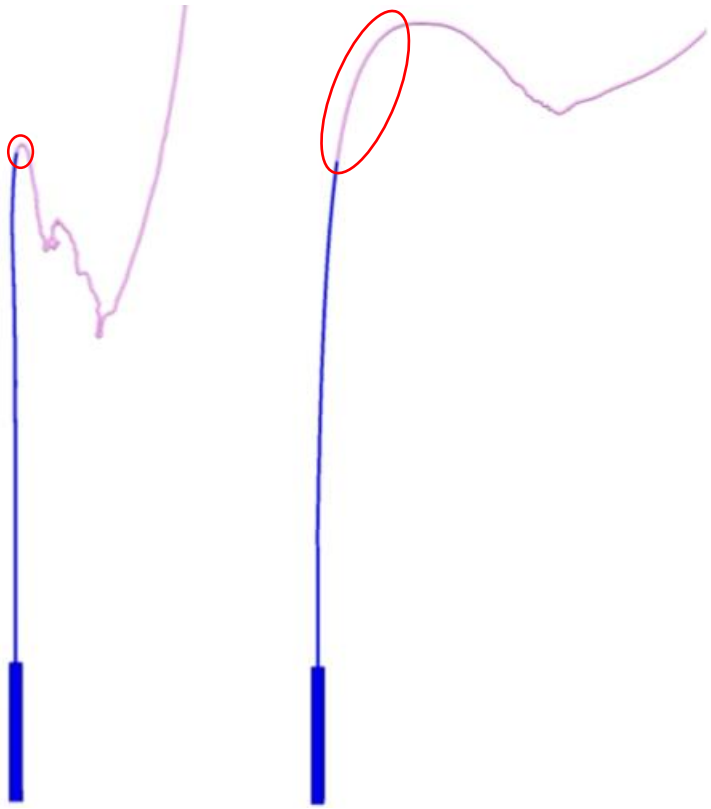

Figure 10-12: Snapshots at T=4.4 sec for X_{DIST} equal to 50m (left) and 170m (right) (SIMA/RIFLEX, 2015).

Within the two areas circled in Figure 10-12, the vertical extension of the chain is approximately 1m (area to the left) and 17m (area to the right). This difference is significant. The figure also gives a good representation of the free falling behavior of the chain in an initially narrow or wide chain loop. The bottom element in the loop in the left figure has fallen significantly longer than the chain in the right figure. This effect can also be observed for all other X_{DIST}-values in Figure 10-13.

In Figure 10-13 all snapshots are taken at the approximate time of touchdown (T=4.4sec). The upper and lower end of the view is approximately z=-410m and z=-465m, respectively.

X_{DIST} = 50 m	X_{DIST} = 75 m
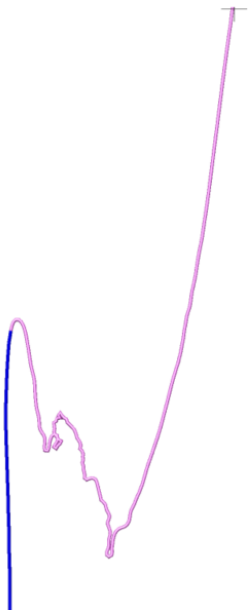	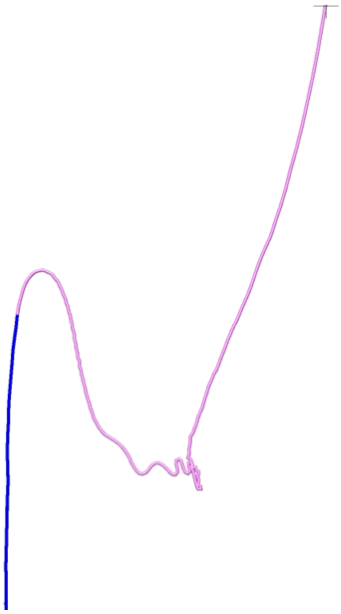
X_{DIST} = 100 m	**X_{DIST} = 125 m**
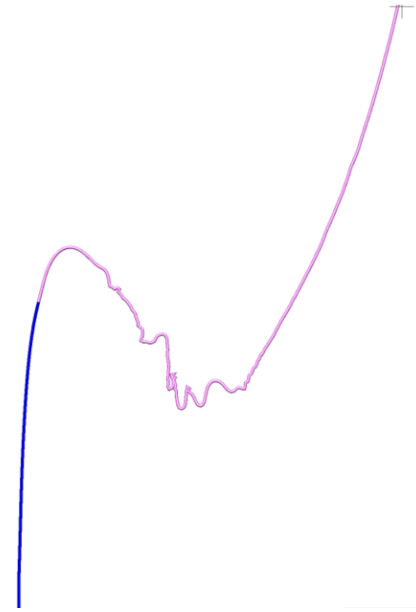	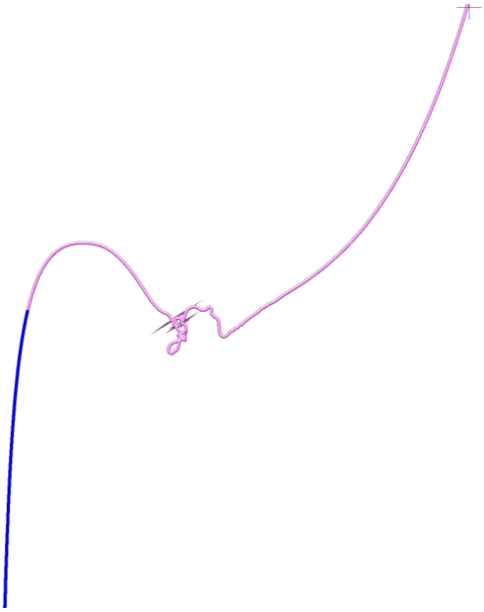

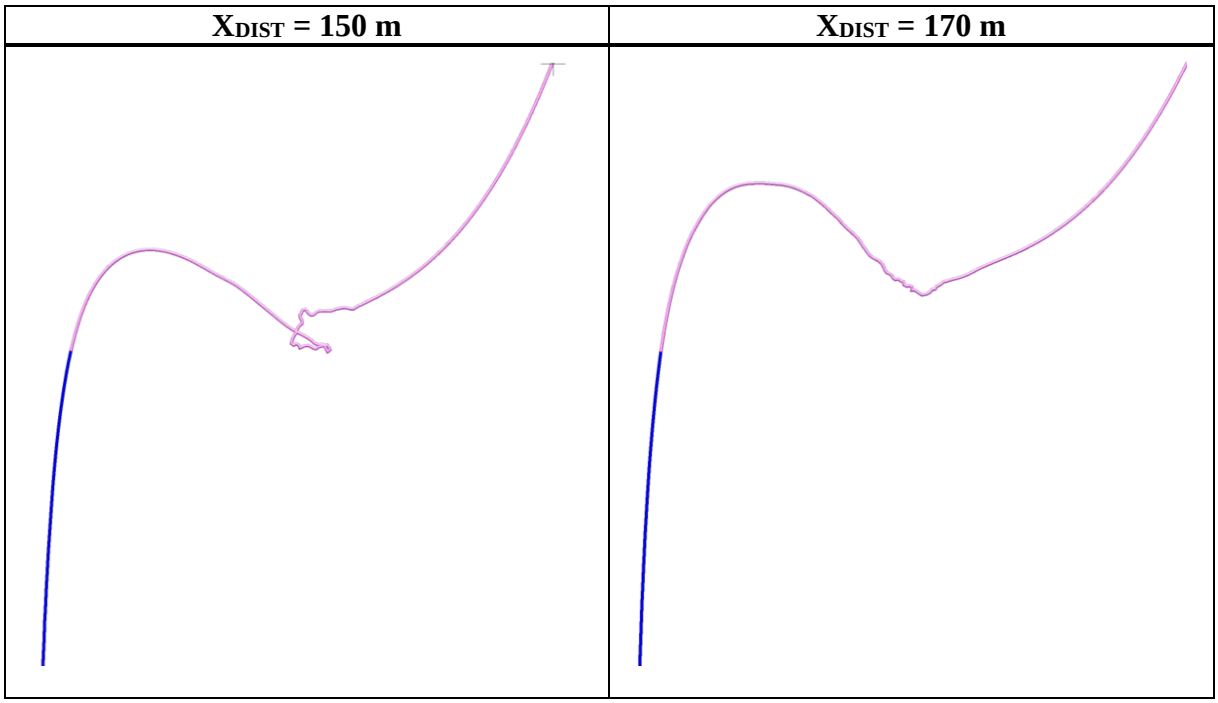

Figure 10-13: Mooring line configuration at the approximate time of touchdown for all values of X_{DIST}.

One can observe in Figure 10-13 the tendency that the relative vertical distance between the bottom point of the loop and the anchor tip increases for increasing X_{DIST}. As expected, the stretch in the horizontal direction increases throughout the snapshots. It is also seen how the lines in general becomes less curled for increasing values of X_{DIST}. The curled parts of the line disappear for X_{DIST} = 170m. However, some of the observed curls in the chain are artificial. As mentioned in Section 8.1, RIFLEX does not account for lines crossing each other. The model is created with elements that are able deal with unlimited rotations, meaning that the elements can deform in any way. The RIFLEX analysis is numerical, hence, the model will not be able to reproduce the exact line behavior on element level. However, the model is able to show that the tension in the mooring line disappears and the chain becomes curled after anchor drop. Some tension is restored in the chain segment when the anchor pulls the chain down. It is seen that this effect increases with increasing values of X_{DIST}.

10.2.4 Touchdown Velocity and Tilt Angle

The effect of mooring line configuration on touchdown velocity and tilt angle of the anchor are also investigated. Table 10-5 presents the results of touchdown velocity and tilt angle for all values of X_{DIST}.

Table 10-5: Velocity and Tilt Angle as a function of $X_{DIST.}$

Parameter	**Values**						**Unit**
X_{DIST}	50	75	100	125	150	170	m
Velocity	26.4	26.0	25.9	25.4	24.8	24.9	m/sec
Tilt angle	0	0	0	0	0	0	deg

The velocities in Table 10-5 ranges from 24.9 m/sec to 26.4m/sec, and decreases for increasing X_{DIST}. However, the variation is small, and the difference between the highest and lowest velocity is only 5.7%. As seen in the table, the tilt angle is zero for all investigated cases. This is due to the long vertical chain behind the anchor. To the right in Figure 10-12 (largest X_{DIST}) the upper part of the vertical chain is pulled to the right, while the lowest part is still completely vertical.

It can be concluded that the width of the chain loop affects the behavior of the chain as it is falling towards the sea bottom. It can also be concluded that the anchor tilt angle is not affected for the investigated values of X_{DIST} when a sufficient length of vertical chain ($L_{VERT.CHAIN}$ =50m) is present behind the anchor at initiation of anchor drop. If the vertical chain was shorter, the horizontal force from the mooring line would probably have propagated all the way down to the anchor and maybe tilted it. This problem is investigated in the next chapter.

11 Variation of Vertical Chain length

Until now, the length of the vertical chain behind the anchor is kept constant ($L_{VERT.CHAIN}$=50m). This length is now varied to investigate its influence on velocity and tilt angle of the anchor, in addition to the dynamic behavior of the mooring line. $L_{VERT.CHAIN}$ is decreased incrementally from 50m to 10m, with steps of 10m. The total length of the bottom chain is kept constant equal to 150m. Two water depths with two horizontal distances between the upper ends of the installation wire and mooring line (X_{DIST}) are investigated. These values are listed in Table 11-1.

Table 11-1: Water depths h and corresponding X_{DIST}-values

h	$X_{DIST,1}$	$X_{DIST,2}$	Unit
500	50	150	m
1500	170	510	m

The length of the fiber insert is also kept constant equal to 390m for h = 500m and 1390m for h = 1500m.

Current is not applied in this chapter. The influence of current is already investigated in Chapter 9 and partly in Section 10.2.2.

The supernode coordinates are adjusted so that the anchors tip is released from approximately the same elevation above the seabed for all analyses. This can be looked into in the attached Excel file.

11.1 Change of Chain Element Size

In previous analyses, the chain element length in the vertical chain and the mooring line has been different, $L_{ELEM,VERT.CHAIN}$ = 1m and $L_{ELEM,MOOR.CHAIN}$ = 0.25m. This significant length difference, may have affected the results. Since only one chain dimension is described in Section 5.4, the chain element length in RIFLEX should have been equal in all analyses to give a good comparison between different water depths. However, changing the element size in this chapter makes it possible to investigate how the element size affects the behavior of the chain segments during free fall. In this chapter $L_{ELEM,VERT.CHAIN}$ = $L_{ELEM,MOOR.CHAIN}$ = 0.5m. This value is based on the real chain link size. The length of a chain element should represent the true size of a chain link. As described in Figure 5-8 in Section 5.4, the distance between the contact surfaces in a standard link is $4 \cdot D_{NOM}$. This distance is shown in Figure 11-1.

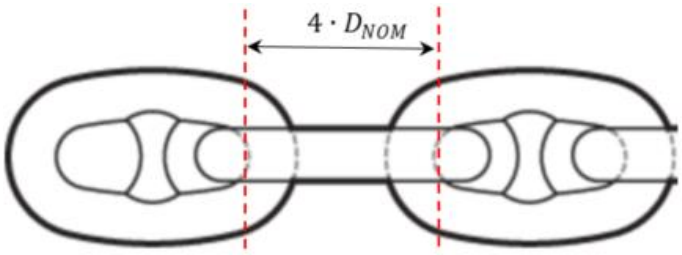

Figure 11-1: Chain element length

Using D_{NOM} = 142mm, gives $4 \cdot D_{NOM}$ = 586m. To keep it simple and take into consideration that the selected chain dimension is comparatively large, $L_{ELEM,CHAIN}$ is set to 0.5m in this Chapter.

11.2 h=500m, X_{DIST}=50m

The total length of the mooring line is set to 540m for h = 500m in the RIFLEX model. This corresponds to 108% of the water depth.

11.2.1 Touchdown Velocity and Tilt Angle

Table 11-2 shows the touchdown velocity and tilt angle of the anchor as a function of $L_{VERT.CHAIN}$.

Table 11-2: Velocity and tilt angle for h=500m, X_{DIST}=50m in vertical length variation analysis.

Parameter	Values					Unit
Chain Length	50	40	30	20	10	m
Touchdown Velocity	24.7	25.0	25.82	25.1	25.83	m/sec
Tilt Angle	-0.05	-0.10	0.04	-0.19	0.01	deg

It is seen in Table 11-2 that the anchor touchdown velocity is higher for the shortest vertical chain length than for the longest. It is however observed that the velocity for $L_{VERT.CHAIN}$ =30m is higher than for $L_{VERT.CHAIN}$ = 40m and 20m. The variation in the values are small and the trend is that the velocity is just slightly increasing for decreasing vertical chain lengths. The difference between the lowest and highest velocity is just approximately 1m/sec.

In earlier chapters, where $L_{ELEM,VERT.CHAIN}$ = 1m, the tilt angle was zero degrees for all cases. After changing the length to 0.5m, it is observed in RIFLEX that the vertical chain is not straight vertical during free fall anymore. This is also observed in the snapshots in Figure 11-2, especially for the longest chain lengths. This obviously has some effect on the tilt-angle even though a tilt angle of 0.19° is considered as negligible.

11.2.2 Snapshots during free fall

Snapshots of the anchor and mooring line at T=3sec are presented in Figure 11-2. The anchor tip is located at approximately z=-465m in all snapshots.

50m	40m
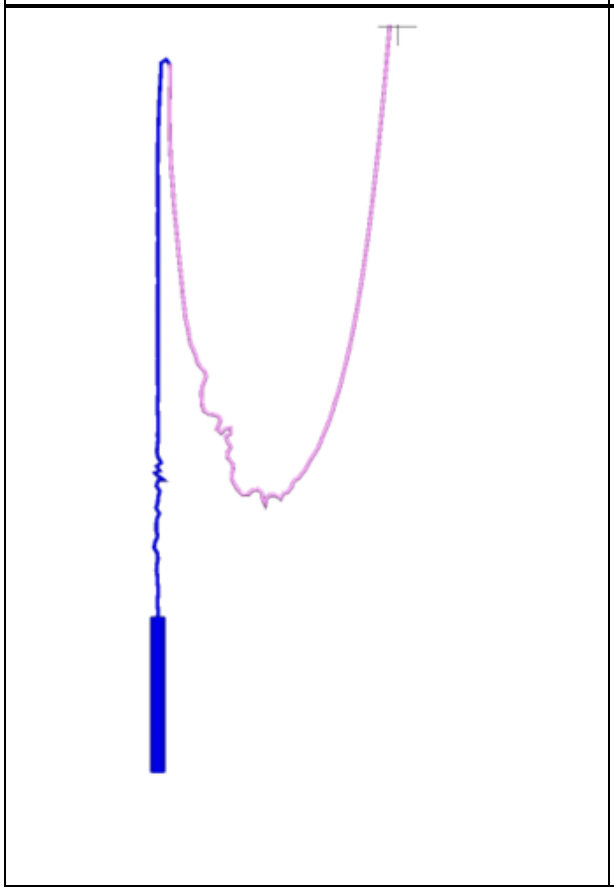	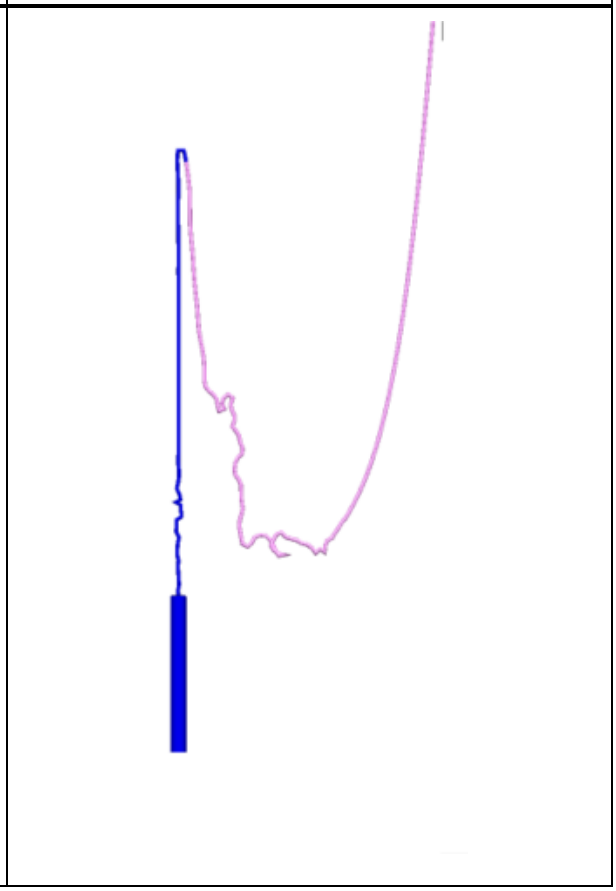

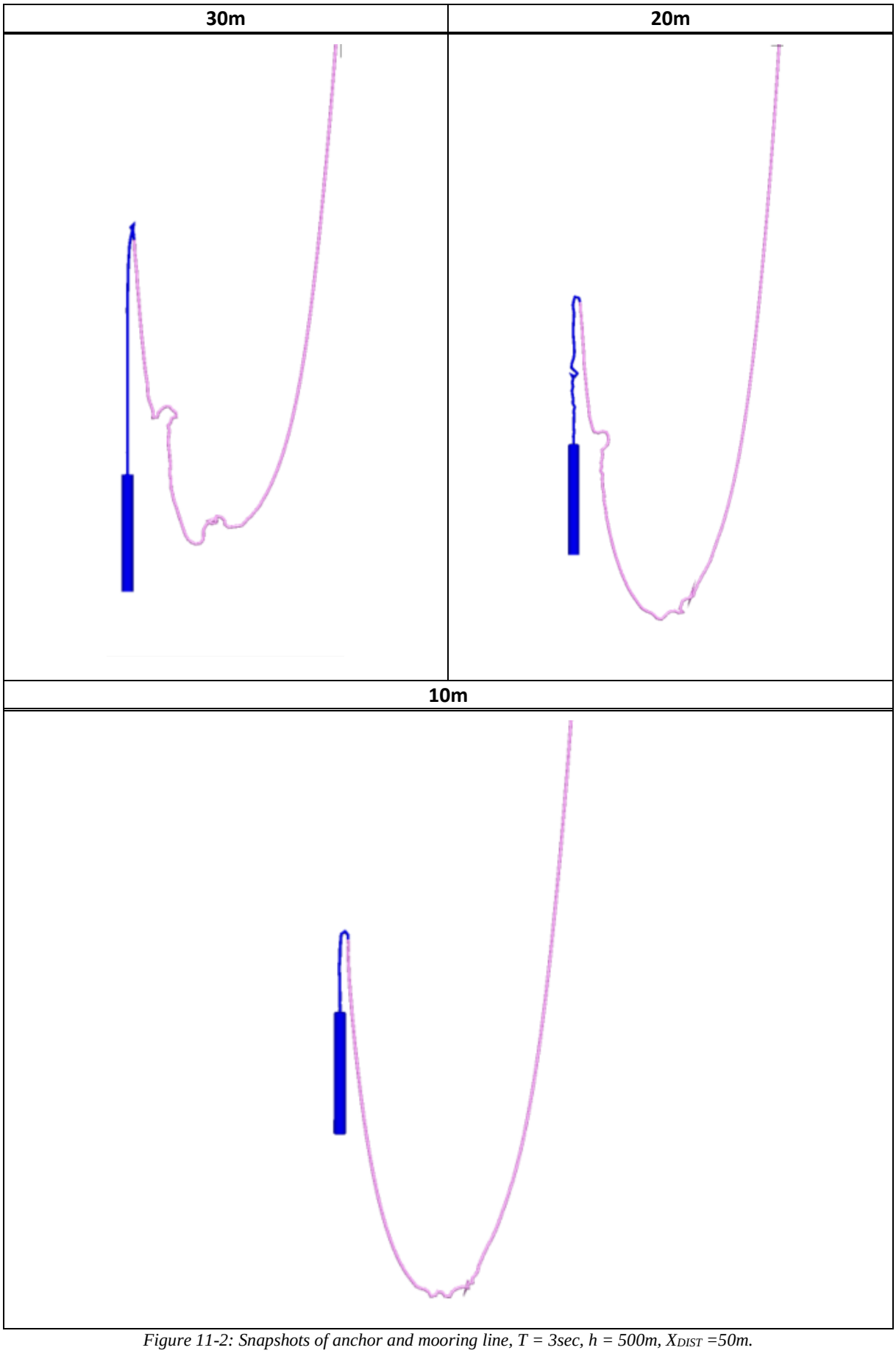

Figure 11-2: Snapshots of anchor and mooring line, T = 3sec, h = 500m, X_{DIST} =50m.

It is observed in Figure 11-2 that the chain loop becomes curled in all snapshots. However, it seems like it becomes less curled for decreasing vertical chain lengths. Also, parts of the vertical chain become curled to some degree. Just as for the chain loop, this implies a loss of geometric stiffness. Dividing $L_{VERT.CHAIN}$ into several elements gives larger flexibility in the system.

The position of the anchor tip relative to the bottom of the chain loop is interesting to examine. It is clearly seen in Figure 11-2 how the chain loop sinks deeper for decreasing $L_{VERT.CHAIN}$ since the mooring line becomes longer. As shown in Section 10.1.1, a narrow and deep chain loop almost falls with the same velocity as the anchor. The anchor and chain loop is then observed to hit the seabed approximately at the same time. This is illustrated in Figure 11-3 by comparing the configuration of the mooring line at the time of touchdown for $L_{VERT.CHAIN}$ = 50m (wide loop) and 10m (narrowest loop).

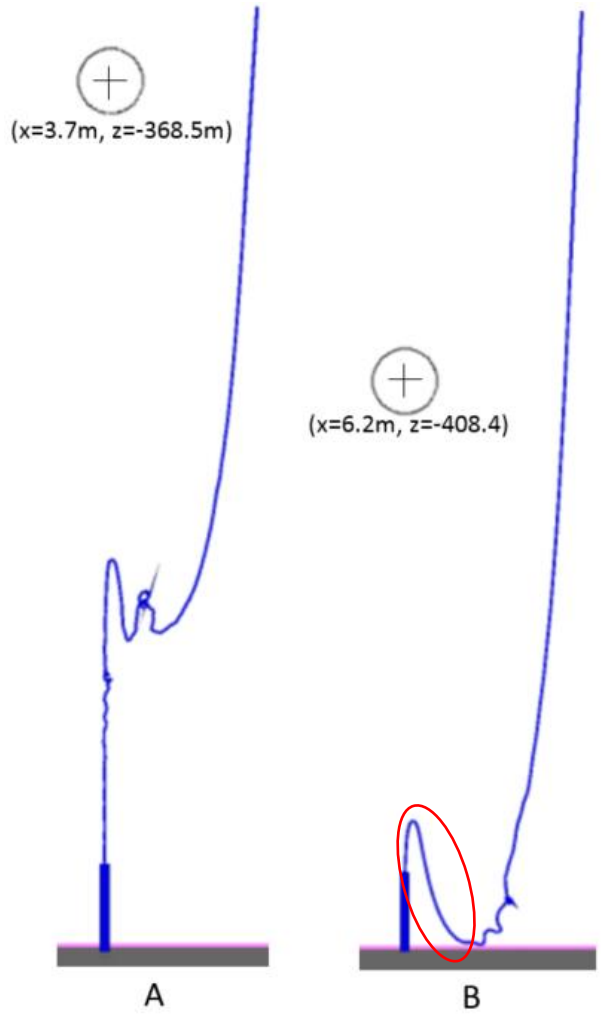

Figure 11-3: Anchor touchdown at seabed, T = 4.5sec, $L_{VERT.CHAIN}$ = 50m (A) and 10m (B)

In Figure 11-3 A), the curled section of the chain takes place several meters above the seabed. This implies that the chain is located behind the anchor at all times during free fall, and no chain

pileup occurs at the seabed provided that the length of the mooring line is not too long. There is no chain next to the anchor hitting the seabed simultaneously as/before the anchor tip. In Figure 11-3 B), the chain touches the seabed almost simultaneously as the anchor. If the length of the mooring chain within the circled area is long, there will be a pileup of chain on the seabed. In this analysis, the chain length between the back tip of the anchor and the seabed touchdown point is only approximately 30m ($L_{VERT.CHAIN}$+L_{ELEM} · 44elements) and the anchor has not started seabed penetration yet. Hence, chain pileup does not seem to be a problem.

11.3 h=500m, X_{DIST}=170m

The total length of the mooring line is also here set to 540m for h = 500m in the RIFLEX model. This corresponds to 108% of the water depth.

11.3.1 Touchdown Velocity and Tilt Angle

Table 11-3 shows the touchdown velocity and tilt angle of the anchor as a function of $L_{VERT.CHAIN}$.

Table 11-3: Velocity and tilt angle for h = 500m, X_{DIST} =170m in vertical length variation analysis.

Parameter	Values					Unit
Chain Length	50	40	30	20	10	m
Touchdown Velocity	24.44	24.17	24.03	23.57	23.37	m/sec
Tilt Angle	-0.02	0.04	-0.04	1.16	2.96	deg

In Table 11-3 the touchdown velocity is observed to decrease by small amounts for decreasing values of $L_{VERT.CHAIN}$. This is opposite of the results from the analysis with X_{DIST} = 50m where the trend shows increased velocity for decreased $L_{VERT.CHAIN}$. The negligible reduced velocity for the larger loops can however be explained by the following. The loop is significantly wider, and the elements are therefore more horizontally aligned (See Figure 10-8). As described in Section 10.1.1 a wider loop is exposed to larger drag forces and the free falling behavior is limited.

By comparing the minimum velocity in Table 11-3 (found at $L_{VERT.CHAIN}$ = 10m) with the maximum velocity in Table 11-2, the anchor touchdown velocity is reduced with approximately 2.5m/sec when X_{DIST} = 170m. It can therefore be argued to use a low as possible X_{DIST}. Using a short vertical chain length could give chain at rest on the seabed before anchor penetration is complete, and this is not wanted.

The tilt angle for the three longest vertical chain lengths is negligible. The anchor starts to become tilted for $L_{VERT.CHAIN}$ = 20m but only the tilt angle for $L_{VERT.CHAIN}$ = 10m (3°) is of importance. This value is still within the installation criteria of 5°. However, due to the rapid increase between $L_{VERT.CHAIN}$ = 20m and 10m it can be argued that X_{DIST}-values higher than 30% of the water depth (170m/500m) could result in high tilt angles.

11.3.2 Snapshots during free fall

Snapshots of the anchor and mooring line at T = 3sec are presented in Figure 11-4. The anchor tip is located at approximately z=-464m in all snapshots.

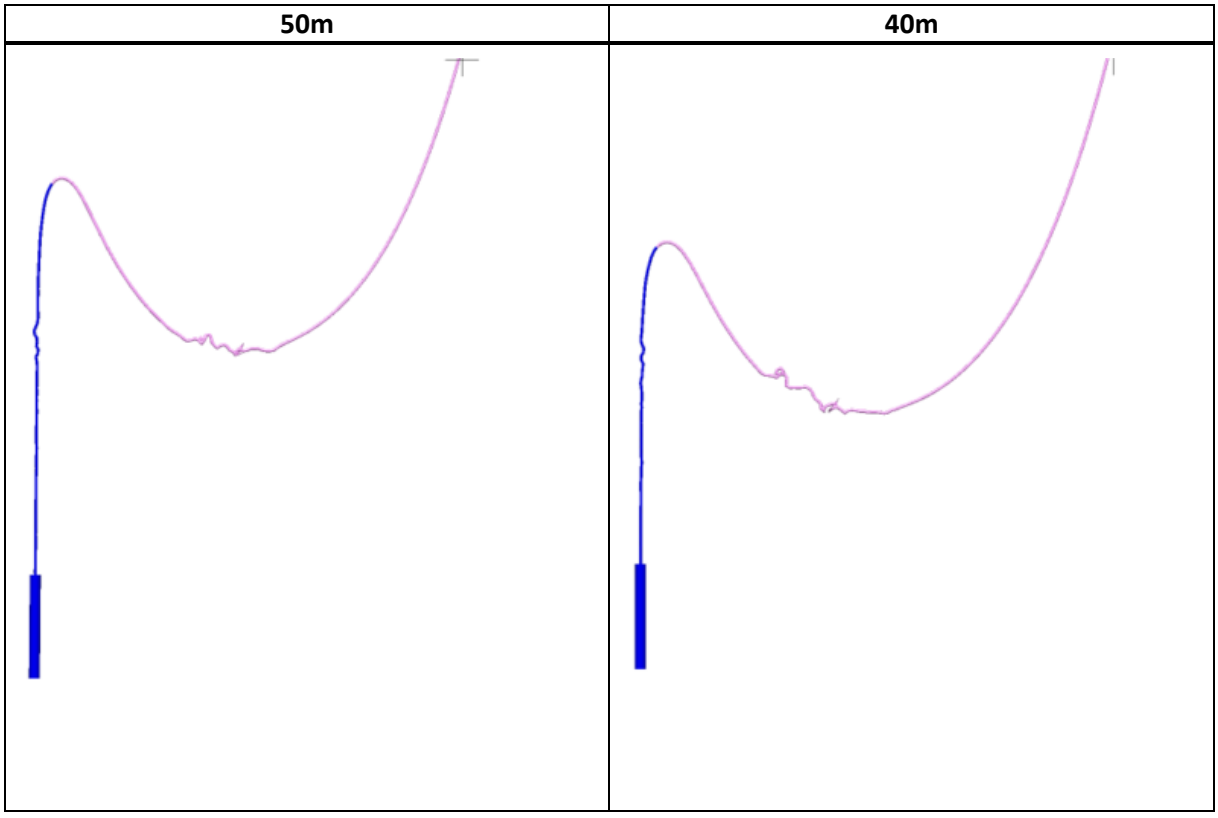

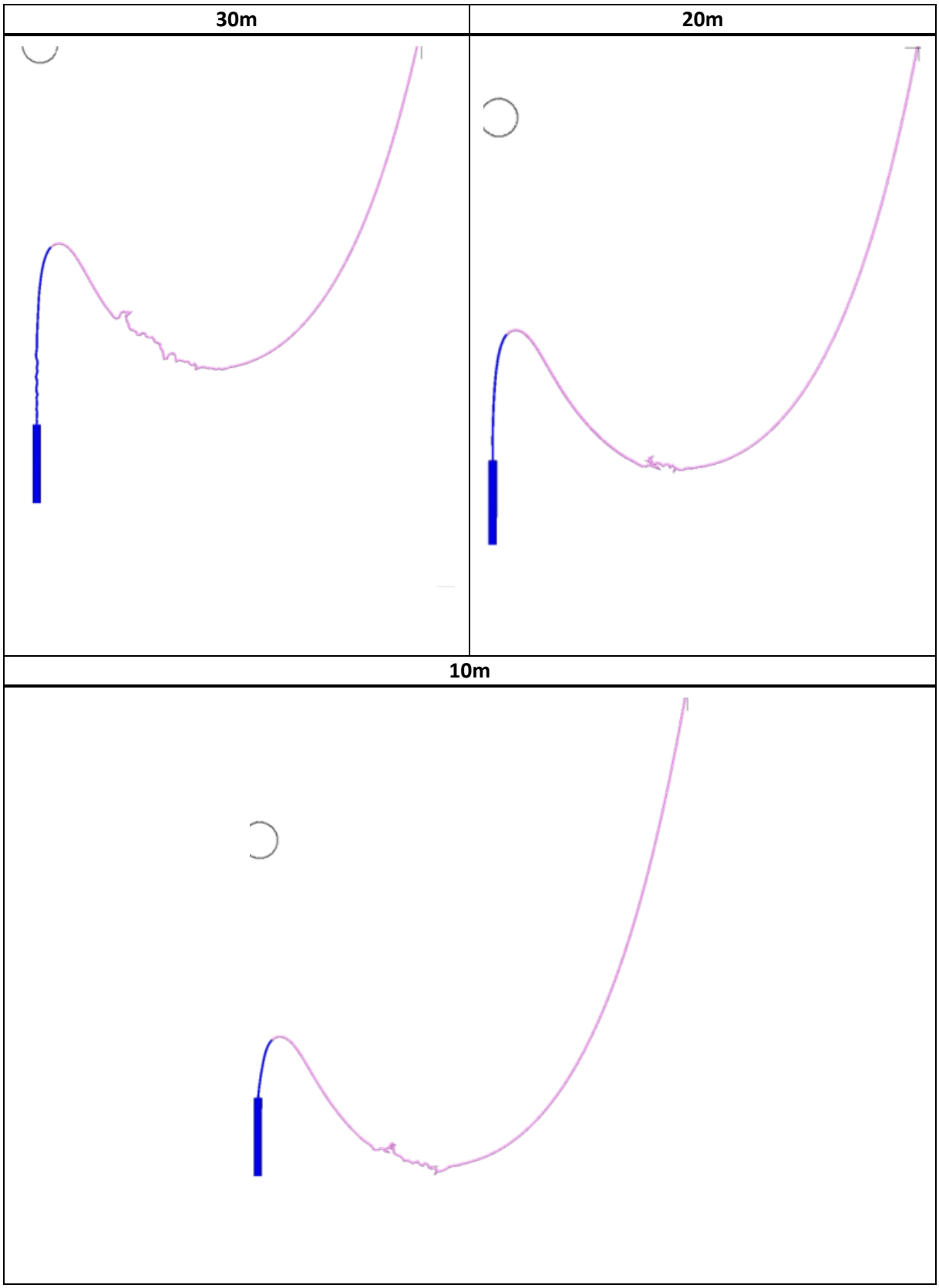

Figure 11-4: Snapshots of anchor and mooring line, T = 3sec, h = 500m, X_{DIST} =170m.

The mooring line is significantly less curled in all snapshots in Figure 11-4 compared to Figure 11-2. The significantly higher drag forces probably limit the free falling behavior, which also

creates a higher axial tension in the line. By comparing the snapshots for $L_{VERT.CHAIN}$ = 10m in the two figures, it is seen that the 10 meter of vertical chain is much more tilted in Figure 11-4 compared to Figure 11-2. This is due to the horizontal extension of the mooring line caused by the high horizontal distance (X_{DIST}) between the upper nodes of the installation wire and the mooring line. The vertical line is "eaten up" by the horizontal component of the hydrodynamic forces on the mooring line. Hence, the anchor becomes tilted for decreasing vertical chain lengths in combination with deeper and wider chain loops.

11.4 h=1500m, X_{DIST}=150m

$L_{Mooring}$ is set to 1540m for h = 1500m. Same value as used in earlier analyses. This corresponds to 102% of the water depth. If the length is adjusted so that it corresponds to 108% of h, the line becomes too long and pileup of chain occurs on sea bottom. In order to find the static equilibrium condition (initial condition for the dynamic analysis) without errors, the original dynamic model explained in Section 6.3 is modified. The top node of the vertical chain is fixed in analyses for h = 500m, while prescribed displacements are used in the model for h = 1500m. This is illustrated in Figure 11-5.

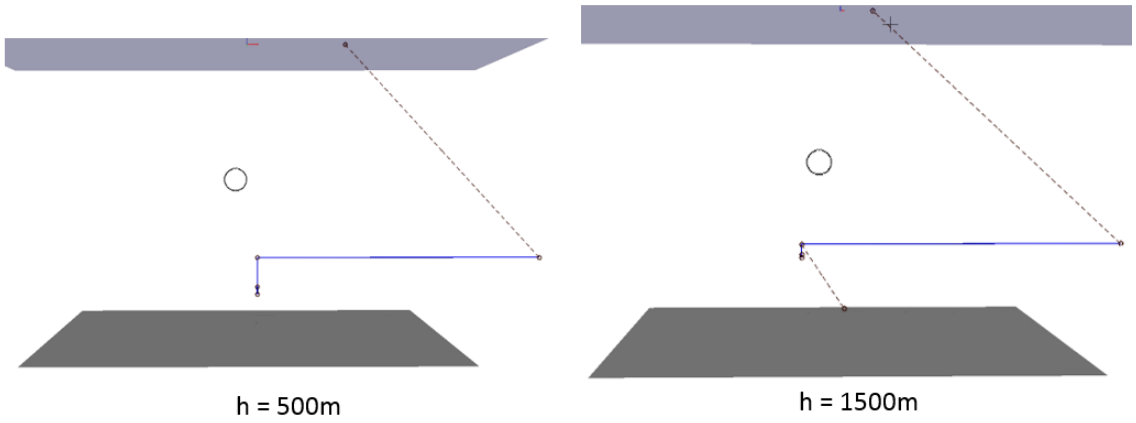

Figure 11-5: Comparison of RIFLEX models for h = 500m and 1500m

The number of load steps in the static calculation of the dynamic analysis model is adjusted from 300 to 600 for the specified displacements in order to obtain equilibrium in the calculations.

11.4.1 Touchdown Velocity and Tilt Angle

Table 11-4 shows the touchdown velocity and tilt angle of the anchor as a function of $L_{VERT.CHAIN}$.

Table 11-4: Velocity and tilt angle for h = 1500m, X_{DIST} =150m in vertical length variation analysis.

Parameter	Values					Unit
Chain Length	50	40	30	20	10	m
Touchdown Velocity	24.5	25.0	25.8	24.7	25.2	m/sec
Tilt Angle	0.16	0.03	0.00	0.17	0.36	deg

The results in this section are compared to results in Section 11.2 (h=500m, X_{DIST}=50m). The same trend is shown in Table 11-4 and Table 11-2. Also here, the velocity for $L_{VERT.CHAIN}$ = 10m is higher than for $L_{VERT.CHAIN}$ = 50m. $L_{VERT.CHAIN}$ = 30m gives the is highest velocity. The difference between the lowest and highest velocity is here 1.3m/sec.

The highest tilt angle is observed for the lowest $L_{VERT.CHAIN}$. This agrees with the observation in Section 11.3.2 stating that the tilt angle increases for decreasing $L_{VERT.CHAIN}$. The angle is however negligible.

11.4.2 Snapshots during free fall

Snapshots of the anchor and mooring line at T = 3sec are presented in Figure 11-6. The anchor tip is located at approximately z=-1470m in all snapshots.

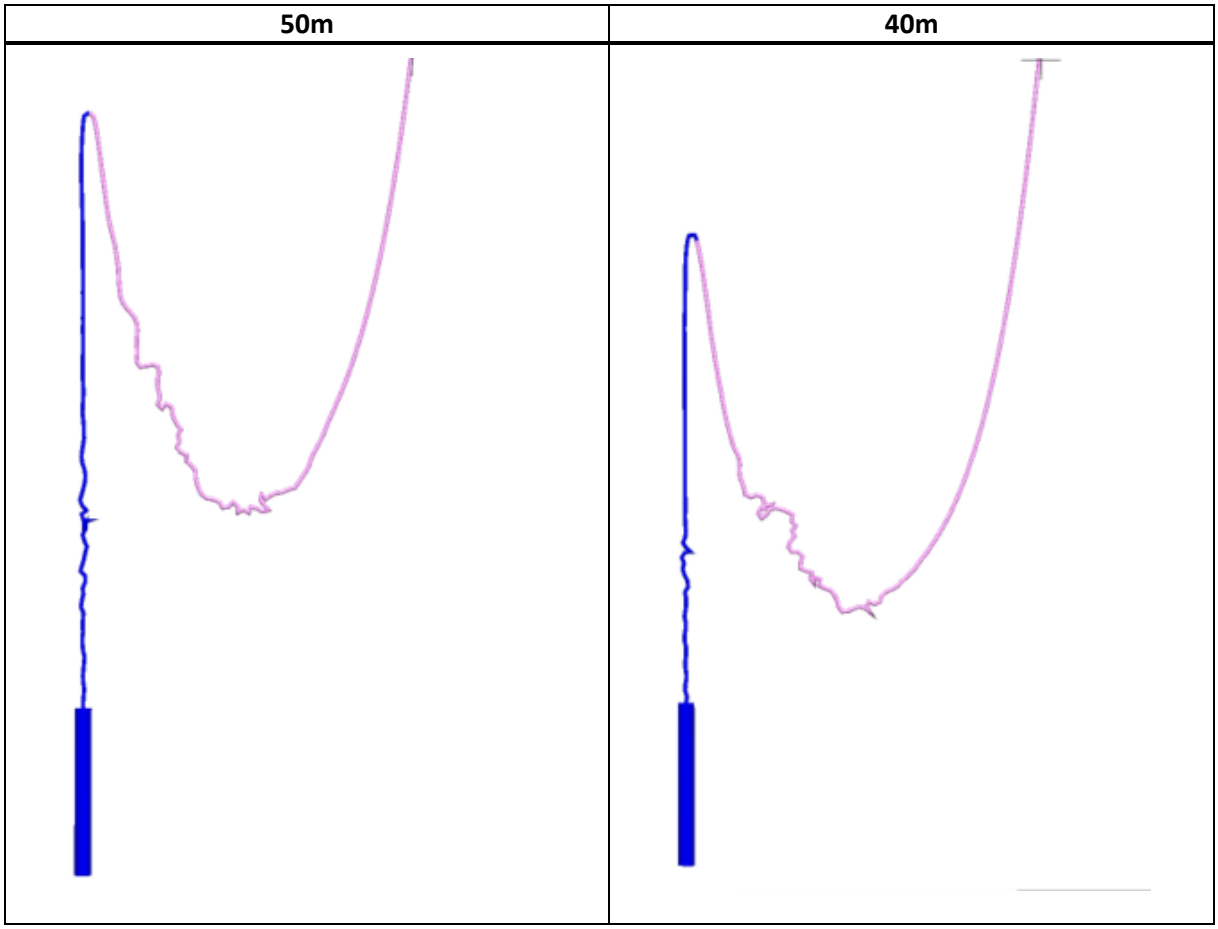

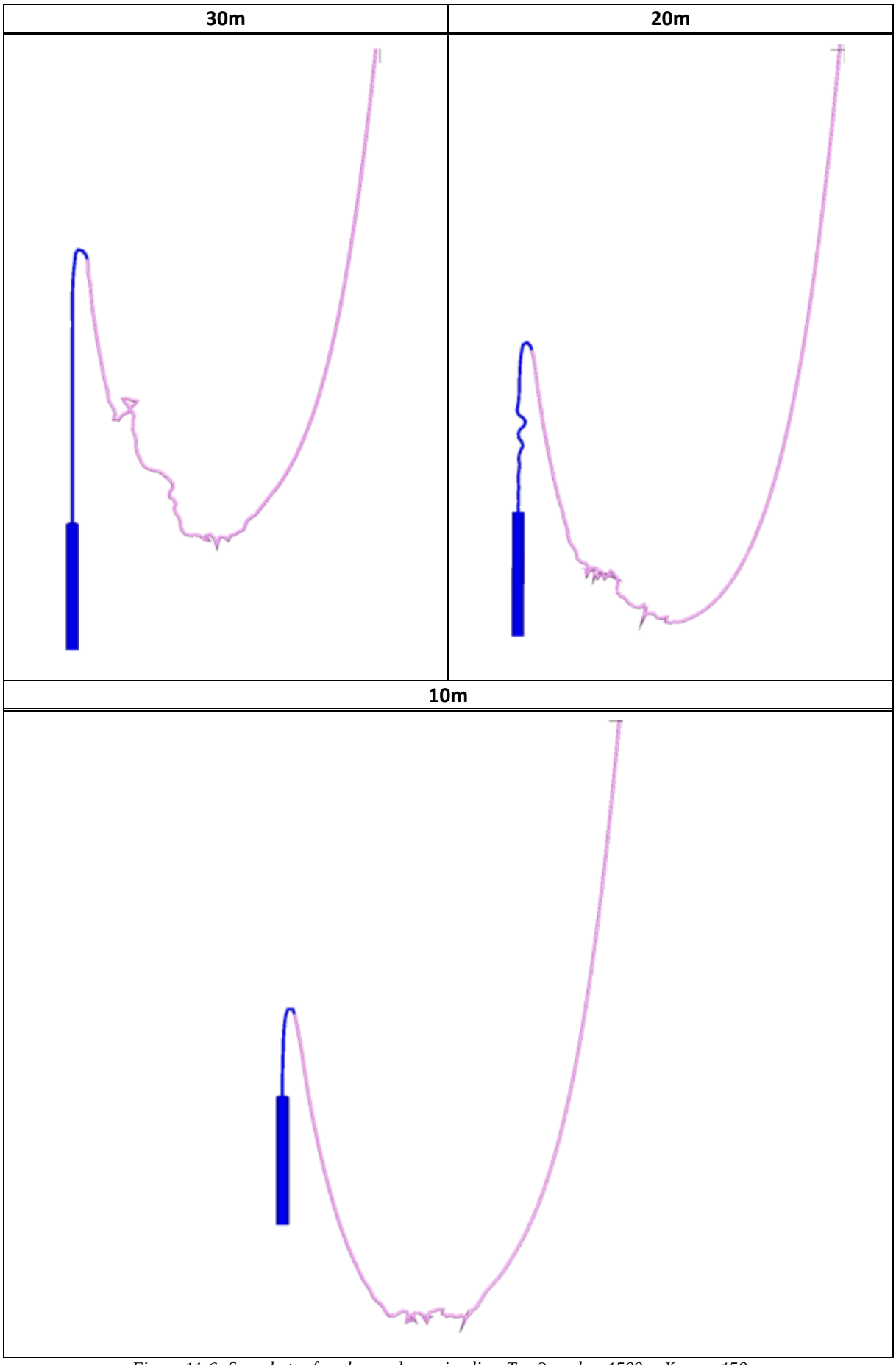

Figure 11-6: Snapshots of anchor and mooring line, T = 3sec, h = 1500m, X_{DIST} = 150m.

The mooring line becomes less curled for decreasing $L_{VERT.CHAIN}$. The configuration of the line is comparable to the snapshots in Section 11.2.2.

11.5 h=1500m, X_{DIST}=510m

X_{DIST} = 510m is selected based on X_{DIST} = 170m for h = 500m. A distance of 170m corresponds to 34% of the water depth of 500m. The same percentage is used for h = 1500m which gives X_{DIST} = 510m.

It is observed in RIFLEX that $L_{Mooring}$ = 1540m becomes too short in this analysis due to the significant distance between the upper nodes (X_{DIST}). The anchor barely touches the seabed before the mooring line is stretched to an almost straight angled line between the top node and the sea bottom. This is seen in Figure 11-7.

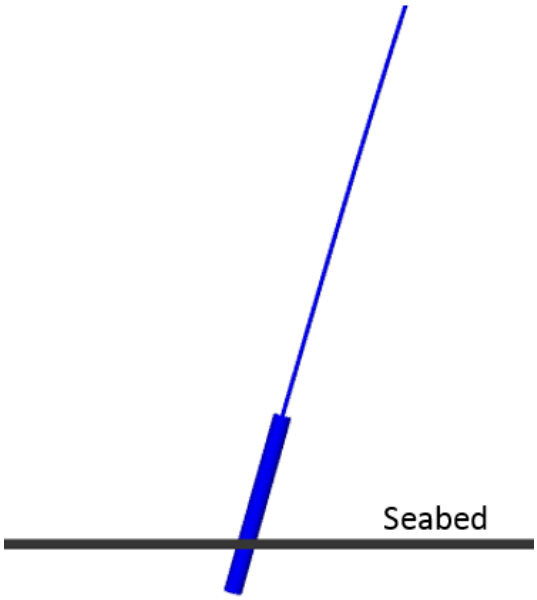

Figure 11-7: Illustration of touchdown with too short mooring line.

Based on the observed anchor touchdown shown in Figure 11-7 the length of the mooring line is increased to 1620m, which corresponds to $L_{Mooring}$=1.08h used in Section 11.2.

11.5.1 Touchdown Velocity and Tilt Angle

Table 11-5 shows the touchdown velocity and tilt angle of the anchor as a function of $L_{VERT.CHAIN}$.

Table 11-5: Velocity and tilt angle for h = 1500m, X_{DIST} =510m in vertical length variation analysis.

Parameter	Values					Unit
Chain Length	50	40	30	20	10	m
Touchdown Velocity	23.5	24.0	23.7	23.8	23.3	m/sec
Tilt Angle	0.10	0.23	-0.27	0.66	2.98	deg

The touchdown velocity is almost unaltered fort for all values of $L_{VERT.CHAIN}$.

The tilt angle becomes significant for the largest chain loop ($L_{VERT.CHAIN}$ = 10m). This is the same behavior as in Section 11.3.1. The maximum tilt angle observed here (approximately 3°) is equal to the one observed in Section 11.3.1.

11.5.2 Snapshots during free fall

Snapshots of the anchor and mooring line at T = 3sec are presented in Figure 11-8. The anchor tip is located around z=-1467m in all snapshots.

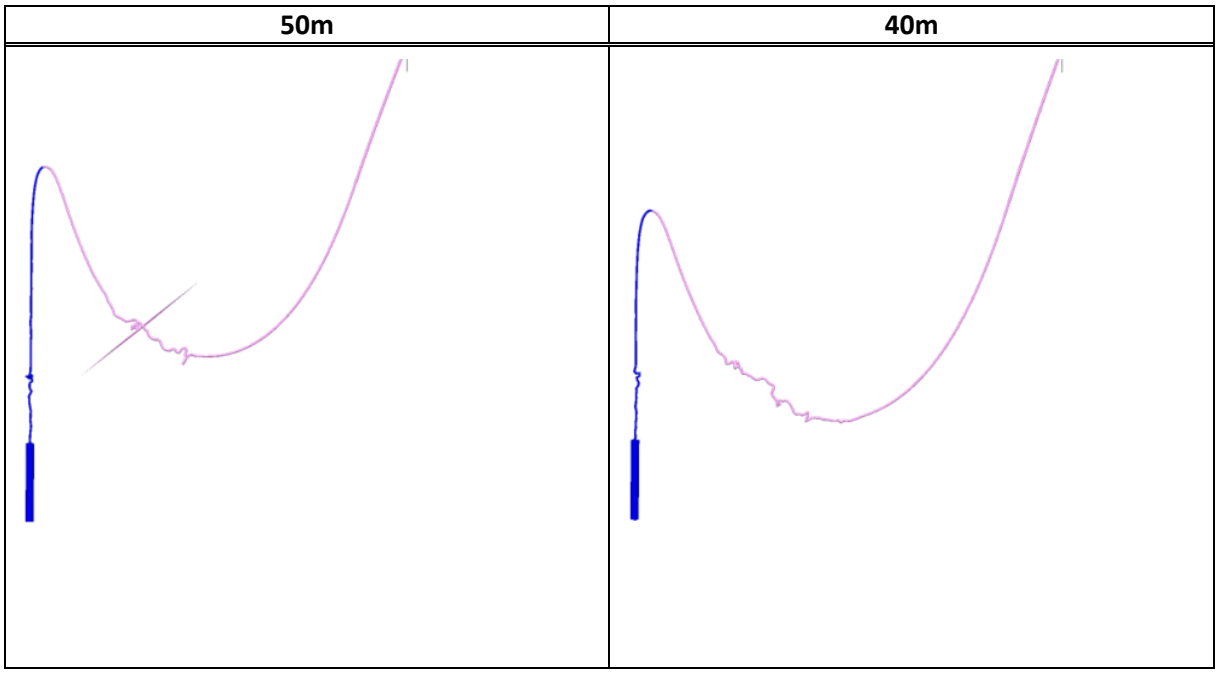

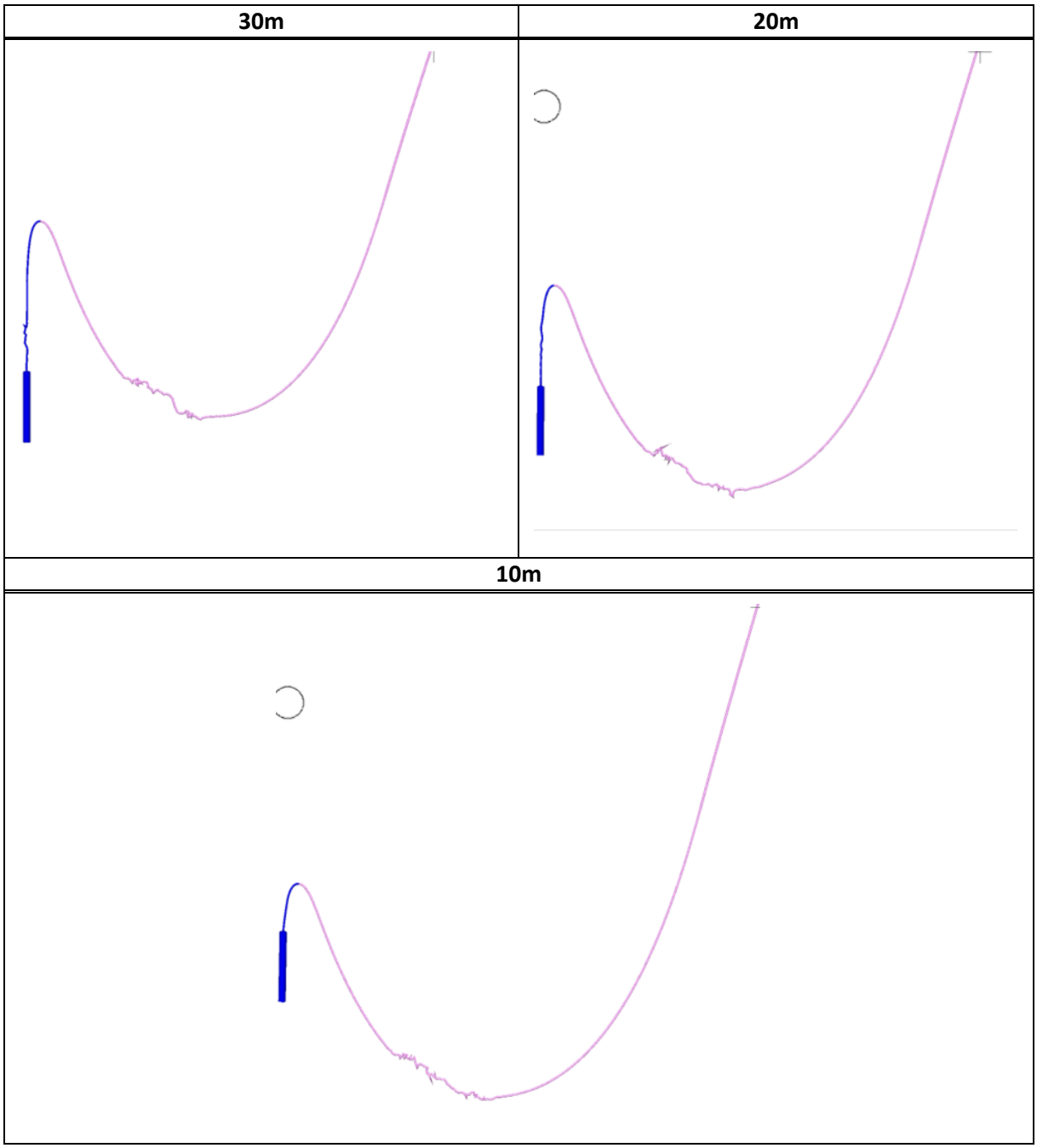

Figure 11-8: Snapshots of anchor and mooring line, T = 3sec, h = 1500m, X_{DIST} = 510m.

The chain configurations in the snapshots in Figure 11-8 are comparable to the configurations in Figure 11-4. However, one difference is observed. In the snapshots for $L_{VERT.CHAIN}$ = 10m, it is seen in Figure 11-8 that the bottom point of the chain loop is closer to the seabed than the anchor tip, while it is opposite in Figure 11-4. This means that the length of the mooring line for h = 1500m is probably too long and a pile up of chain may occur at the seabed. X_{DIST} and $L_{MOORING.CHAIN}$ is determined as a percentage of the water depth. Since the penetration depth of the anchor is assumed equal for the two depths, $L_{MOORING.CHAIN}$ should be determined by a lower percentage (<108%) for the highest water depth in order to give the same configuration

of the line when the anchor has reached full seabed penetration. The length should may have been determined as a function of both the water depth and X_{DIST}.

11.6 Comments to the results

It is observed that changing the vertical chain length has minor effect on the touchdown velocity. The variation in velocity for decreasing $L_{VERT.CHAIN}$ lies within +/- 1m/sec in all the cases.

It is observed that the tilt angle becomes significant for the largest X_{DIST} considered for each water depth. The maximum tilt angle occurs at $L_{VERT.CHAIN}$ = 10m. X_{DIST} = 170m and 510m corresponds to 34% of the water depth, and it can therefore be argued that tilt angles becomes significant for X_{DIST}>0.3h. This is where the chain loops are largest (depth and width). The tilt angle is observed to be 3° for $L_{VERT.CHAIN}$ = 10m for both water depths. This implies that the ratio between width and depth of the chain loop (w/d) is the governing parameter. The combination of large chain loop width and small chain loop depth causes anchor tilt.

Changing the element size of the vertical chain from 1m to 0.5m results in curls occurring close to the anchor. This is probably due to loss of axial stiffness. The lateral drag coefficient is much smaller than the resistance on the anchor, which may cause it to fall slightly faster than the chain. Doubling the number of elements, gives a higher number of degrees of freedom. The chain is therefore able to bend more.

12 Discussion

Velocity and drag coefficients

In Chapter 8 it is shown, that the anchor touchdown velocity from the dynamic RIFLEX model corresponds well with values from the Geotechnical Design report for the installation at Gjøa (Deep Sea Anchors, 2009).

As mentioned in Section 6.1.1, the pressure drag coefficient for the anchor ($C_{D,P}$ = 0.43) applied in this thesis is based on the report carried out by CFD Norway AS (1999). CFD Norway found a terminal anchor velocity of 43m/sec, which is approximately 10m/sec higher than observed in RIFLEX (See Section 8.3.1). The report from CFD Norway has used another element distribution and the analyses are based on CFD (computational fluid dynamics). It is therefore understandable that the results differ from each other. According to Jon T. Lieng (2015) the report from CFD Norway showed greater values for "velocity vs. distance" than what was observed during experimental tests (1:3 scale). $C_{D,P}$ was therefore increased to 0.63 in the Geotechnical Design Report for the installation at Gjøa (Deep Sea Anchors, 2009). For a drop height of 70m, $C_{D,P}$ = 0.63 and neglecting drag forces on the mooring chain, the touchdown velocity in the Gjøa report was calculated to 28.44m/sec, while in this thesis it is calculated to 26.2m/sec with $C_{D,P}$ = 0.43. The velocity in the RIFLEX model is then lower , even with a lower pressure drag coefficient. Based on this observation, a more detailed study of the selected drag coefficients on both the anchor elements and the chain should have been performed. In addition, a sensitivity study of the lateral chain drag coefficient and the different coefficients on the anchor should have been conducted.

Chain Element Size in RIFLEX

The chain elements should have been equal in all analyses conducted during the thesis work, in order to give the best overall comparison of the mooring line configuration. The element size is however kept constant for each individual parameter variation. This means that the results in chapter 8, 9, 0 and 11 are representative. The behavior of the mooring line observed in RIFLEX corresponds to expected behavior for all conducted parameter studies.

Chain Modulus of Elasticity

As mentioned in Section 5.4, the modulus of elasticity E for a stud chain of steel grade R3, R4 or R5 cannot be less than $5.6 \cdot 10^{10} Nm^{-2}$. In Section 8.2.2, it turns out that the modulus of elasticity found by Equation (8-3) (E = 5.49e+10 Nm^{-2}) is slightly lower than the criteria. This was discovered too late, because the modulus of elasticity is not given directly to RIFLEX. It is the cross-section area A_{CROSS} and stiffness $(EA)_{CHAIN}$ that are given as input values. The wrong value for E is therefore applied in Table 5-5 since this is the value used in RIFLEX.

The MBL for the selected chain is 18033kN. It is observed in the results of the static analysis in RIFLEX that maximum tension in the vertical chain segment (for $L_{VERT.CHAIN}$ = 50m) is only approximately 890kN (when the anchor is hanging in the drop position). The maximum operational design load of the mooring line, is approximately 5500kN on seabed (Deep Sea Anchors, 2009). This load can be considered as the design load for the 80tonne DPA. The fact that the observed max load during installation in RIFLEX and the design load from real life is not even close to the MBL for the chain, implies that yielding is far from reached. The slightly lower modulus of elasticity used in RIFLEX will therefore not affect the results. $(EA)_{CHAIN}$ is only a function of the diameter (Equation (5-10)), hence, the applied axial stiffness (EA) is correct.

Wire Cross-section Constant C

It should be mentioned, that an error is found in the excel spreadsheet for the wire calculations, at the end of the thesis work. The reduction factor C for the wire cross-section is set to 0.586 instead of 0.418 in all analyses. The wire cross-section is therefore reduced with 16,8% more than what was intended. This affects all parameters including the cross-sectional area in a conservative way, since the correct cross-section is larger. The wire elongation calculated in APPENDIX D is dependent on the axial stiffness in the wire. Decreasing the cross-section area, decreases the axial stiffness. This results in higher elongation for the same load. Hence, the values for the wire elongation becomes too large and are therefore on the conservative side.

Penetration Phase

According to Jon T. Lieng (2015) the penetration depth is estimated with an in-house program based on the method formulated by True (1975) (See Section 3.1.4). The required input is soil data, anchor size, mass and drop height. The program is not available to the public, and seabed penetration depth is therefore not calculated in this thesis. The touchdown velocity obtained

from RIFLEX and the corresponding kinetic energy of the anchor can be used as input to such a calculation.

Anchor model

Compared to real life, the anchor model is significantly simplified. The size hollow section of the model and real anchor differs in size. This is because the anchor model is assumed only to consist of one material (steel) while the real anchor consists of different materials. The anchor walls are steel, and the filling material can be e.g. steel grit or concrete. However, the calculated total weight of the anchor and COG corresponds to the data for the real anchor. Hence, the model should able to describe the behavior during free fall in a realistic manner.

Parameters for Describing the Shape of the Chain Loop

After investigating the influence of the vertical chain length variation on velocity and tilt angle, it seems like the tilt angle is dependent on the ratio between width and depth of the chain loop. Different values for this ratio should have been investigated further.

Vessel Motions and Dynamic Effects

The upper nodes of the installation wire and mooring line are fixed in all analyses. No wave motions are accounted for, meaning that the dynamics in the system are neglected. The vessel motions in waves create a time dependent force in the installation wire. The point in time where the anchor is released, is therefore not arbitrary. On extensive water depths, the dynamic system behavior will be complex since the weight of the wire itself becomes larger than the weight of the anchor hanging in the lower end. In addition, the response frequency of the wire will probably differ from the load frequency (vessel motion). For shallower waters, the dynamic effect will be small unless the weather conditions are harsh.

13 Concluding Remarks

13.1 Conclusion

A model of a torpedo anchor installation is created in RIFLEX, using data for an 80tonne DPA. The anchor, installation wire, chain segment and fiber rope are implemented using beam elements. The behavior of the anchor and mooring line during free fall are compared to earlier test results and calculations provided by Jon Tore Lieng. Parameters such as current, variation of node positions and vertical chain lengths are studies for several water depths.

It is shown that the anchor touchdown velocity is highly dependent on the tangential chain drag coefficient. Values obtained from the DNV standard DNV-OS-E301 "Position Mooring" gives too high resistance and can therefore not be used.

By comparing with previous experimental test results, The RIFLEX model proves to describe anchor and mooring line behavior in a good manner. The model is able to visualize that the tension in the mooring line disappears and the chain becomes curled after anchor drop.

The effect of current is investigated for a specific current profile. It is observed that current affects the static equilibrium position of the anchor relative to the top node of the wire. Displacements in the horizontal direction are significant, while vertical displacements are negligible. The current force is not sufficient to affect the anchor and mooring line during free fall.

The mooring line becomes significantly less curled for larger horizontal distances between the installation vessels (X_{DIST}). The geometric stiffness during free fall is therefore higher in a wide chain loop. With the drag coefficients applied in this thesis, the narrow chain loop next to the anchor falls with a significantly higher velocity towards the seabed compared to a wide chain loop.

The anchor tilt angle, measured when the anchor hits the seabed, becomes significant for X_{DIST} larger than 30% of the water depth and vertical chain lengths shorter or equal to 20m, when the length of the mooring line is determined as 108% of the water depth. A chain loop with the combination of a large width and small depth causes anchor tilt. This implies that the ratio (w/d) between width and depth of the chain loop is the governing parameter.

13.2 Recommendations for Further work

Suggestions for further work are listed in the following.

Investigation of the Seabed Penetration Phase

The penetration phase has not been investigated in this thesis. Simulation of this phase is required in order to build a complete simulation of the torpedo anchor installation. To investigate this phase, a FE model of the seabed using soil data for the specific location is required. The model must be capable of describing the resistance on the anchor when it hits the seabed, the side forces on the anchor during penetration and friction forces on the shaft and fins. RIFLEX may also be used for this purpose by utilizing nonlinear springs on the tip and sides of the anchor. However, it is difficult to model the soil separation around the anchor in a RIFLEX model.

Motions from Vessels and Waves

I could be of interest to investigate the dynamic effects from vessel motions and wave forces. Analyses with waves are therefore of interest for extensive water depths where the dynamic effects becomes complex. Keywords may be; eigenfrequencies, slack wire, snatch loads in wire, horizontal and vertical dynamic motions.

Drag Element on Installation Wire

In the project thesis, the "rubberband effect" (contraction in wire after anchor release) was investigated. In order to reduce this effect, an element which creates large amounts of drag forces during wire contraction can be installed in the lower end of the wire to provide additional damping. Designing and testing of such an element may be conducted.

Anchor model

Develop the anchor model with respect to resistance coefficients in order to give a closer fit to data from previous test results.

Drag Coefficient on Chain Segment

It can be recommended to investigate the value for the lateral drag coefficient of a vertical free falling chain in water.

Current Profiles

Current profiles are highly dependent on the geographical location, e.g. the Gulf of Mexico vs. the North Sea. It could therefore be interesting to investigate scenarios with different current profiles.

Limiting Water Depth

Investigation of the most shallow water depth the torpedo anchor can be used for, could be of interest.

14 References

American Petroleum Institute. (2011). API Specification 9A. Specification for Wire Rope (pp. 13). www.api.org: American Petroleum Institute.

API - American Petroleum Institute. (2011). API SPECIFICATION 9A - Specification for Wire Rope. 26 Edition (Vol. 9A, pp. 72). api.org: API - American Petroleum Institute.

API. (1993). Recommended Practice for Planning, Designing and Constructing Fixed Offshore Platforms *Fundation Design, Pile Fundations* (pp. 242).

Britannica.com. (2015). Stud-link chain. Retrieved 09.06, 2015, from http://global.britannica.com/EBchecked/topic/569873/stud-link-chain

CFD Norway AS, C. F. D. (1999). 'Hydrodynamic analysis of Deep Penetrating Anchor", Part 2 of feasibility study: " Development of New anchor Concept for Deep Water mooring in Soft Seabed Sediements". Trondheim, Norway.

Christophe, G., Kien H., T., & Samy, O. (2009). Keying of Plate Anchors in NC Clay Under Inclined Loading. *International Journal of Offshore and Polar Engineering (ISSN 1053-5381, 19*.

D. Hagen, E. Andenæs, G. M. Korstad, & Aker Marine Contractors AS. (1998). *Inovative Suction Anchor Design and Installation*. Paper presented at the Offshore Technology Conference, Huston, Texas, 4-7 May 1998. https://www.onepetro.org/download/conference-paper/OTC-8833-MS?id=conference-paper%2FOTC-8833-MS

Deep Sea Anchors. (2009). Installation of Two Permanent Deep Penetrating Anchors at the Gjøa Field in the North Sea - Geotechnical Design Report.

Deep Sea Anchors. (2010, 4. september 2014 15:07:44). DPA Concepts. from http://www.deepseaanchors.com

Deep Sea Anchors, & Statoil. (2009). Torpedo Anchor Installation (DPA). 40. http://www.ktf.no/fileadmin/Dokumenter/Kursdokumenter/2009/3_subsea_lifting_operations/13-torpedo-anchors-installation.pdf

Delmar Systems Inc. (2011). The OMNI-Max. In I. Delmar Systems (Ed.). www.delmarus.com.

DNV. (2004). Design of Offshore Steel Structures General (LRFD Method) *Offshore standard DNV-OS-C101*.

DNV. (2008). Offshore Standard DNV-OS-E302 Offshore Mooring Chain (pp. 30): Det norske Veritas.

DNV. (2010). Recommended Practice DNV-RP-C205 (pp. 124). www.dnv.no.

DNV. (2013a). DNV-OS-E303 - Offshore Fibre Ropes (Vol. DNV-OS-E303, pp. 42). http://www.dnv.no/: Det Norske Veritas - Germanischer Lloyd.

DNV. (2013b, October 2013). Offshore Standard DNV-OS-E301 Position Mooring. from http://exchange.dnv.com/publishing/downloadPDF.asp?url=http://exchange.dnv.com/publishing/codes/docs/2013-10/OS-E301.pdf

dredgingengineering.com. (2015). Catenary or Taut. Retrieved 19.02.2015, 2015, from http://www.dredgingengineering.com/moorings/overview/Tool%20Ibb.html

eFunda.com. (2015). General Properties of Steels. Retrieved 20.02.2015, 2015, from http://www.efunda.com/materials/alloys/alloy_home/steels_properties.cfm

Engineeringtoolbox. (2014). Modulus of Rigidity. Retrieved 14.11.2014, from http://www.engineeringtoolbox.com/modulus-rigidity-d_946.html

Faltinsen, O. M. (1990). *Sea Loads on Ships and Offshore Structures*: Cambrdge University Press.

Global Perspectives Deep & Ultra-deepwater Technology & Projects Report. (2008). Global Perspectives Deep & Ultra-deepwater Technology & Projects Report. Retrieved 13.12.2014, 2014, from http://www.infield.com/Deep-and_Ultra_deepwater_Technologies_and_Markets.htm

Goodfellow. (2015). Polyethylene terephthalate (Polyester, PET, PETP) Material Information. Retrieved 03.03.2015, 2015, from http://www.goodfellow.com/E/Polyethylene-terephthalate.html

Grande, L. O. (1976). Interaction between Pile and Soil *Doctorial Dissertation*. Geotechnical Division, NTH: NTH.

Hasselø, K. K., & Petrobras. (2005). Planlegging og gjennomføring - Torpedo oppankring i Brasil: Farstad.

IACS. (2011). Anchor Mooring Chain (pp. 23): IACS International Assosiation of Classification Societies LTD.

Inter Ocean Systems. (2014). Model 6500/6600 Rig Anchor Release. Retrieved 13.12.2014, 2014, from http://www.interoceansystems.com/rel_rar.htm

Janbu, N. (1973). *Pile fundation. Calculation of bearing capacity of piles, design analyses of pile groups.* NIF-couse (in Norwegian): Geotechnical Division, Norwegian Institute of Technology.

Kai-tung Ma, Chevron Energy Technology Company; Arun Duggal, SOFEC Inc; Philip Smedely, BP Exploration Operation Company Limited; Didier L'Hostis, TOTAL SA; Hongbo Shu, & Shell internation E&P Inc. (2013). *A Historical Review on Integrity Issues of Permanent Mooring Systems*. Paper presented at the Offshore Technology Conference, Houston, Texas, USA.

KTL Group. (2014). KTL Group. In K. O. P. L. A. s. o. K. G. Ltd (Ed.), *Wire Rope, Rigging and Mooring for Offshore Construction* (pp. 106). http://www.ktlgroup.com/.

Langen, I., & Sigbjörnsson, R. (1979). Dynamisk Analyse av Konstruksjoner. 295.

Larsen, C. M. (2014a) *Conversation and discussion/Interviewer: D. Landhaug*.

Larsen, C. M. (2014b). *TMR4182 Marin dynamikk*: Akademika forlag.

Larsen, C. M. (2015) *Conversation and discussion abot the master thesis/Interviewer: D. Landhaug*.

Larsen, K. (2015) *Questions Regarding Deepwater Mooring with DPA/Interviewer: D. Landhaug*. Phone call and meeting.

Lieng, J. T. (2014a). *Anchoring & Mooring of Deepwater Floating Structures*.

Lieng, J. T. (2014b) *Conversation by mail/Interviewer: D. Landhaug*. Outlook.com.

Lieng, J. T. (2015) *Conversation and Questions Regarding DPA/Interviewer: D. Landhaug*. Marine Technology Master, Outlook.com.

Lieng, J. T., Kavli, A., Hove, F., & Tjelta, T. I. (2000). *Deep Penetrating Anchor: Further Development, Optimization And Capacity Verification*. https://www.onepetro.org/conference-paper/ISOPE-I-00-171

Lieng, J. T., Tjelta, T. I., & Skaugset, K. (2010). *Installation of Two Prototype Deep Penetrating Anchors at the Gjoa Field in the North Sea*. Paper presented at the Offshore Technology Conference, 3-6 May, Houston, Texas, USA Houston, Texas, USA. https://www.onepetro.org/conference-paper/OTC-20758-MS

MARIN. (2003). Technical Specificatios Shuttle *Report No. 16656-3-CPO Final report* (pp. 123). 2, Haagsteeg, P.O. Box 28, 6700 AA Wageningen, The Netherlands: Maritime Research Institute Netherlands.

MARINTEK. (2003). MIMOSA User's Documentation. https://projects.dnv.com/sesam/manuals/Mimosa57_UM.pdf

MARINTEK. (2014a). RIFLEX Theory Manual. 144.

MARINTEK. (2014b). RIFLEX User Manual. 144.

MARINTEK. (2014c). SIMA - Simulation and Engineering Analysis of Marine Operations and Floating Systems. In MARINTEK (Ed.). www.sintef.no: MARINEK.

MARINTEK. (2014d). SIMA Help Contents.

MARINTEK, Huse, E., & Øritsland, O. (2000). Handbook of Hydrodynamic Coefficients of Flexible Risers. Report 2.1 -16: MARINTEK.

NASA. (2015). Terminal Velocity. Retrieved 03.06, 2015, from https://www.grc.nasa.gov/www/k-12/airplane/termv.html

Nestegård, A. (2015) *Mail correspondence with DNV regarding DNV-OS-E301 "Positioning Mooring"/Interviewer: D. Landhaug*. outlook.com.

NRK. (2015). Parker Scanrope solgt. Retrieved 05.02, 2015, from http://www.nrk.no/vestfold/parker-scanrope-solgt-1.12134624

Parker Scanrope. (2008). MoorLine - Polyester Mooring Ropes for Offshore Applications (pp. 12). http://parkerepd.com: Parker Parflex.

Raie, M. S., & Tassoulas, J. L. (2009). Installation of torpedo anchors: Numerical modeling. *Journal of Geotechnical and Geoenvironmental Engineering, 135*(12), 1805-1813.

Ramnäs Bruk AB. (2006). Ramnäs Quality Chains and Accessories (pp. 13). http://ramnas.com.

Rigzone.com. (2015). How do Mooring Systems Work? Retrieved 04.02.2015, 2015, from https://www.rigzone.com/training/insight.asp?insight_id=358&c_id=17

SAL Heavy Lift. (2013). *3D simulation: offshore penetration anchor installation*. www.youtube.com.

SAL Heavy Lift. (2014). Your partner for fast, safe delivery of your heavy cargo. Retrieved 12.12.2014, 2014, from http://sal-heavylift.com/home/

Shelton, J. T. (2007). *OMNI-Max Anchor Development and Technology*. Paper presented at the Oceans 2007 Conference, Vancouver. http://www.delmarus.com/uploads/MTSOceans2007TechnicalPapermodified.pdf

SIMA/RIFLEX. (2015). Sima 3.1.1.12020: MARINTEK.

Sotra Anchor & Chain. (2015). Stud Link Chain - Common link. 2015, from http://www.sotra.net/products/chains/studlink-common-link

Statoil, & Larsen, K. (2014). Calorfloat Cut-Resistant Jacket.

Statoil, & Moxnes, S. (2011). *SIMA – The new graphical interface for RIFLEX and SIMO*. Stavanger 2011: Statiol.

Total. (2014). Mooring Integrity Operator view.

True, D. G. (1975). Penetration of Projectiles into Seafloor Soils. Port Hueneme: Naval civil Engineering Laboratory.

Vryhof. (2010). Mooring systems.

Wilde, B. (2009). Torpedo Pile Anchors Enter the GoM. 2.

Appendix

APPENDIX A Technical Data for Wires

Table 14-1: Table of steel wire ropes. ISO 2403. (MARIN, 2003)

STEEL WIRE ROPES
ISO 2408 VALUES

DIAMETER mm	SIX-STRAND 6*26 WS / 6*31 WS / 6*36 WS / 6*41 WS						EIGHT-STRAND 8*26 WS / 8*31 WS / 8*36 WS / 8*41 WS			
	FIBER CORE GRADE 180 E = 80.0 kN/mm2 C = 0.497		STEEL CORE GRADE 180 E = 105.0 kN/mm2 C = 0.586		STEEL CORE GRADE 200 E = 105.0 kN/mm2 C = 0.586		STEEL CORE GRADE 180 E = 85.0 kN/mm2 C = 0.586		STEEL CORE GRADE 200 E = 85.0 kN/mm2 C = 0.586	
	BREAK STRENGTH kN	WEIGHT IN AIR N/m	BREAK STRENGTH kN	WEIGHT IN AIR N/m	BREAK STRENGTH kN	WEIGHT IN AIR N/m	BREAK STRENGTH kN	WEIGHT IN AIR N/m	BREAK STRENGTH kN	WEIGHT IN AIR N/m
20	234.00	14.911	252.00	16.383	279.00	16.383	256.00	16.383	283.00	16.383
22	283.00	18.050	305.00	19.816	338.00	19.816	309.00	19.816	343.00	19.816
24	336.00	21.484	363.00	23.642	402.00	23.642	368.00	23.642	408.00	23.642
26	395.00	25.212	426.00	27.762	472.00	27.762	432.00	27.762	479.00	27.762
28	458.00	29.234	494.00	32.177	548.00	32.177	501.00	32.177	555.00	32.177
32	598.00	38.161	646.00	41.987	715.00	41.987	655.00	41.987	725.00	41.987
36	757.00	48.363	817.00	53.170	905.00	53.170	829.00	53.170	918.00	53.170
40	934.00	59.645	1010.00	65.629	1120.00	65.629	1020.00	65.629	1130.00	65.629
44	1130.00	72.202	1220.00	79.461	1350.00	79.461	1240.00	79.461	1370.00	79.461
48	1350.00	85.936	1450.00	94.568	1610.00	94.568	1470.00	94.568	1630.00	94.568
52	1580.00	101.043	1710.00	110.853	1890.00	110.853	1730.00	110.853	1910.00	110.853
56	1830.00	116.739	1980.00	128.511	2190.00	128.511	2000.00	128.511	2220.00	128.511
60	2100.00	134.397	2270.00	148.131	2510.00	148.131	2300.00	148.131	2550.00	148.131
64	-	-	-	-	-	-	2620.00	167.751	2900.00	167.751
68	-	-	-	-	-	-	2960.00	189.333	3270.00	189.333
72	-	-	-	-	-	-	3310.00	212.877	3670.00	212.877
76	-	-	-	-	-	-	3690.00	237.402	4090.00	237.402
80	-	-	-	-	-	-	4090.00	262.908	4530.00	262.908
84	-	-	-	-	-	-	4510.00	289.395	5000.00	289.395

TENSILE GRADES:
GRADE 180 = 180 kgf/mm2 = 1.766 kN/mm2
GRADE 200 = 200 kgf/mm2 = 1.962 kN/mm2

Table 14-2: Available diameters and minimum breaking load (MBL) for steel wire rope standard 6-strand wire rope construction: bright ungalvanised) and drawn galvanised (KTL Group, 2014)

Nominal Diameter		Approximate Weight Per Metre		Minimum Breaking Load (metric tons)						
				ANSI/API 9A/ISO 10425 Specification		KISWIRE High Tensile Grades			USHA MARTIN High Tensile Grades	
(mm)	(inches)	(kg/m)	(lb/ft)	EIPS	EEIPS	Alpha	Delta	Omega	Super Titan	Titan Max
CLASS 6x19 & 6x37 Steel Core										
12.7	1/2	0.68	0.46	12.1	13.2	These grades are not available under 2" (52mm) diameter				
16	5/8	1.07	0.72	18.7	20.6					
19	3/4	1.55	1.04	26.7	29.4					
22	7/8	2.11	1.42	36.1	39.7					
26	1	2.75	1.85	46.9	51.6					
28	1-1-/8	3.48	2.34	59	64.8					
32	1-1/4	4.3	2.89	72.5	79.7					
35	1-3/8	5.21	3.50	87.1	96.1					
38	1-1/2	6.19	4.16	103	113.4					
42	1-5/8	7.26	4.88	120	132.5					
45	1-3/4	8.44	5.67	139	152.9					
48	1-7/8	9.67	6.50	158	174.3					
52	2	11.0	7.39	180	197	226	233	**	227	**
54	2-1/8	12.4	8.35	200	221	241	252	**	254	**
57	2-1/4	13.9	9.36	224	247	275	289	**	281	**
60	2-3/8	15.5	10.4	249	274	298	312	**	312	**
CLASS 6x37 Steel Core (API 9A - 1995)										
64	2-1/2	17.3	11.6	274	301	336	353	**	343	**
67	2-5/8	19.0	12.8	299	330	370	389	**	376	**
70	2-3/4	20.8	14.0	333	360	409	429	448	410	448
73	2-7/8	22.8	15.3	361	392	447	469	490	447	490
76	3	24.7	16.6	389	425	491	516	538	484	538
79	3-1/8	26.8	18.0	417	458	522	548	572	522	572
83	3-1/4	29.0	19.5	447	493	557	585	611	562	611
86	3-3/8	31.3	21.0	487	528	607	637	666	602	666
89	3-1/2	33.8	22.7	519	563	659	692	723	642	723
95	3-3/4	38.7	26.0	585	640	714	750	785	717	785
102	4	44.0	29.6	665	720	796	836	**	806	**
CLASS - Large Diameter Six Stranded Rope (ANSI/API 9A/ISO 10425 - August 2004)										
102	4	44.0	29.6	646		796	836	**	806	**
108	4-1/4	49.6	33.3	725		845	887	**	910	**
114	4-1/2	55.7	37.4	805		939	986	**	1004	**
121	4-3/4	62.1	41.7	890		1036	1088	**	**	**
127	5	68.8	46.2	978		1138	1195	**	1196	**
133	5-1/4	74.1	49.8	1015		1184	1243	**	**	**
140	5-1/2	81.1	54.5	1101		1288	1352	**	**	**
146	5-3/4	88.7	59.6	1193		1396	1466	**	**	**
152	6	96.7	65.0	1294		1508	1583	**	**	**

Table 14-3: Factors for stranded wire ropes for general lifting applications (API - American Petroleum Institute, 2011)

Type of Rope	Class	Ropes with Fiber Core or Fiber Center			Ropes with Steel Core or Wire Strand Center					
		Nominal Length Mass Factor (Approx.)	Nominal Metallic Cross-sectional Area Factor	Minimum Breaking Force Factor	Nominal Length Mass Factor		Nominal Metallic Cross-sectional Area Factor		Minimum Breaking Force Factor	
		W_1	C_1	K_1	W_2	W_3	C_2	C_3	K_2	K_3
Single-layer round strand rope	6 × 7	0.345	0.369	0.332	0.384	0.384	0.432	0.432	0.359	0.388
	6 × 19	0.359	0.384	0.330	0.400		0.449		0.356	
	8 × 19	0.340	0.349	0.293	0.407		0.457		0.356	
	6 × 36	0.367	0.393	0.330	0.409		0.460		0.356	
	8 × 36	0.348	0.357	0.293	0.417		0.468		0.356	
	6 × 19M	0.346	0.357	0.307		0.381		0.418	0.332	0.362
	6 × 37M	0.346	0.357	0.295	0.381	0.381	0.418	0.418	0.319	0.346
Rotation-resistant rope	18 × 7	0.382		0.328		0.401		0.433		0.328
	34 (M) × 7	0.390		0.318		0.401		0.428		0.318
	35 (W) × 7					0.454		0.480		0.360 [a] 0.350 [b]

NOTE 1 The nominal length mass factors and nominal cross-sectional area factors are only for information.

NOTE 2 See ISO 17893 for calculation of nominal length mass, nominal metallic cross-sectional area, and minimum breaking force using the factors in this table.

NOTE 3 Spinning loss factor, k, is obtained by dividing K by C.

[a] Up to and including rope grade 1960.

[b] Greater than rope grade 1960 up to and including rope grade 2160.

The Table 14-3 is used to find C=0.418, for Class 6x37M, Ropes with Steel Core or Wire Strand Center and Nominal Metallic cross-sectional Area Factor C_2.

APPENDIX B Ramnäs Bruk Mooring Chains

Table 14-4: Proof and break loads. Ramnäs Bruk Mooring chains. (Ramnäs Bruk AB, 2006)

LOAD (in kN) = $c \times d^2 \times (44 - 0.08 \times d)$ (d in mm)

Test Load	Break Load						Proof Load										Weight	
Grade	ORQ	R3	R3S	R4	R4S	R5	ORQ	R3	R3S Stud	R3S Stud-less	R4 Stud	R4 Stud-less	R4S Stud	R4S Stud-less	R5 Stud	R5 Stud-less		
C-factor	0,0211	0,0223	0,0249	0,0274	0,0304	0,032	0,014	0,0156	0,018	0,0174	0,0216	0,0192	0,024	0,0213	0,0251	0,0223	Stud	Stud-less
mm																	kg/m	
76	4621	4884	5454	6001	6658	7009	3066	3417	3942	3811	4731	4205	5257	4665	5498	4884	126	116
78	4847	5123	5720	6295	6984	7351	3216	3584	4135	3997	4962	4411	5514	4893	5766	5123	133	122
81	5194	5490	6130	6745	7484	7877	3446	3840	4431	4283	5317	4726	5908	5243	6179	5490	144	131
84	5550	5866	6550	7208	7997	8418	3683	4104	4735	4577	5682	5051	6313	5603	6602	5866	155	141
87	5916	6252	6981	7682	8523	8971	3925	4374	5046	4878	6056	5383	6729	5972	7037	6252	166	151
90	6289	6647	7422	8167	9062	9539	4173	4650	5365	5187	6439	5723	7154	6349	7482	6647	177	162
92	6544	6916	7722	8497	9428	9924	4342	4838	5582	5396	6699	5954	7443	6606	7784	6916	185	169
95	6932	7326	8180	9001	9987	10512	4599	5125	5913	5716	7096	6307	7884	6997	8246	7326	198	181
97	7195	7604	8490	9343	10366	10911	4774	5319	6138	5933	7365	6547	8184	7263	8559	7604	206	188
100	7596	8028	8964	9864	10944	11520	5040	5616	6480	6264	7776	6912	8640	7668	9036	8028	219	200
102	7868	8315	9285	10217	11336	11932	5220	5817	6712	6488	8054	7159	8949	7942	9359	8315	228	208
105	8282	8753	9773	10754	11932	12560	5495	6123	7065	6829	8478	7536	9420	8360	9851	8753	241	221
107	8561	9048	10103	11118	12335	12984	5681	6330	7304	7060	8764	7790	9738	8643	10184	9048	251	229
111	9130	9650	10775	11856	13154	13847	6058	6750	7789	7529	9347	8308	10385	9217	10861	9650	270	246
114	9565	10109	11287	12420	13780	14506	6346	7071	8159	7887	9791	8703	10879	9655	11378	10109	285	260
117	10005	10574	11807	12993	14415	15174	6639	7397	8535	8251	10242	9104	11380	10100	11902	10574	300	274
120	10452	11047	12334	13573	15059	15852	6935	7728	8916	8619	10700	9511	11889	10551	12434	11047	315	288
122	10753	11365	12690	13964	15493	16308	7135	7950	9173	8868	11008	9785	12231	10855	12792	11365	326	298
124	11057	11686	13048	14358	15930	16768	7336	8175	9432	9118	11319	10061	12576	11161	13153	11686	337	308
127	11516	12171	13591	14955	16592	17466	7641	8515	9824	9497	11789	10479	13099	11626	13700	12171	353	323
130	11981	12663	14139	15559	17262	18171	7950	8858	10221	9880	12265	10903	13628	12095	14253	12663	370	338
132	12294	12993	14508	15965	17713	18645	8157	9089	10488	10138	12585	11187	13984	12411	14625	12993	382	348
137	13085	13829	15441	16992	18852	19844	8682	9674	11162	10790	13395	11906	14883	13209	15565	13829	411	375
142	13887	14677	16388	18033	20008	21061	9214	10267	11847	11452	14216	12637	15796	14019	16520	14677	442	403
147	14700	15536	17347	19089	21179	22294	9753	10868	12540	12122	15048	13376	16720	14839	17487	15536	473	432
152	15522	16405	18317	20156	22363	23540	10299	11476	13241	12800	15890	14124	17655	15669	18464	16405	506	462
157	16352	17282	19297	21234	23559	24799	10850	12089	13949	13484	16739	14879	18599	16507	19452	17282	540	493
162	17188	18166	20284	22320	24764	26068	11405	12708	14663	14174	17596	15641	19551	17351	20447	18166	575	525
167	18030	19056	21278	23414	25977	27345	11963	13330	15381	14869	18458	16407	20508	18201	21448	19056	611	558
172	18876	19950	22276	24513	27196	28628	12525	13956	16103	15566	19324	17177	21471	19055	22455	19950	648	592
177	19725	20847	23278	25615	28420	29915	13088	14584	16827	16267	20193	17949	22437	19912	23465	20847	686	627

Table 14-5: Offshore mooring chain specifications. Ramnäs Bruk Mooring chains. (Ramnäs Bruk AB, 2006)

Classification Society	API Spec 2F		Ramnäs Inhouse	Offshore Mooring Chain (IACS W22)					DNV-OS-E302 October 2013	
Quality	ORQ		ORQ+20%	R3		R3S		R4	R4S	R5
Tensile test										
Yield strength Re (N/mm2)	-		-	410		490		580	700	760
Ultimate tensile strength Rm (N/mm2)	641		750	690		770		860	960	1000
Elongation A5 (%)	17		15	17		15		12	12	12
Reduction of area Z (%)	40		40	[2] 50		[2] 50		[3] 50	[3] 50	[3] 50
Impact strength										
Min average energy, parent material (J)	58	40	58	60	40	65	45	50	56	58
Min average energy, weld (J)	49	36	34	50	30	53	33	36	40	42
Test temperature 1) °C	0	-15	0	0	-20	0	-20	-20	-20	-20

[1] At the option of the Society the impact test of grade R3 and R3S may be carried out at 0°C or -20°C.
[2] For cast accessories, the minimum value shall be 40%.
[3] For cast accessories, the minimum value shall be 35%.

APPENDIX C Parker Scanrope Polyester Mooring Ropes

Table 14-6: Parker Scanrope polyester mooring ropes for offshore applications (Parker Scanrope, 2008)

MBL [TF]	MBL [kN]	Diameter [mm]	Mass in Air [kg/m]	Mass in Water [kg/m]	Maximum Length [m]
500	4905	138	12.2	3.1	8197
600	5886	149	14.3	3.7	6993
700	6867	160	16.4	4.2	6098
800	7848	169	18.4	4.7	5435
900	8829	178	20.4	5.3	4900
1000	9810	187	22.5	5.8	4450
1100	10791	195	24.4	6.3	4095
1200	11772	203	26.5	6.8	3776
1300	12753	213	29.4	7.6	3397
1400	13734	219	31.3	8.1	3195
1500	14715	226	33.4	8.6	2996
1600	15696	234	35.6	9.2	2809
1700	16677	240	37.5	9.7	2665
1800	17658	248	39.5	10.2	2532
1900	18639	254	42.5	10.9	2353
2000	19620	260	44.6	11.5	2242
2100	20601	266	46.5	12.0	2151
2200	21582	271	48.5	12.5	2062
2300	22563	277	50.7	13.0	1972
2400	23544	282	52.7	13.6	1898
2500	24525	290	55.8	14.4	1792
2600	25506	295	57.9	14.9	1727
2700	26487	300	59.9	15.4	1669
2800	27468	305	61.9	15.9	1616
2900	28449	310	64.0	16.5	1563
3000	29430	315	66.0	17.0	1515

APPENDIX D Stretching of Wire and Chain

In Table 14-7 the elongation of the wire, given in meters, is presented for water depths ranging from 500m to 3000m. The initial wire length in Equation (5-25) is determined based on a drop height of approximately 70m above seabed, a vertical chain segment of 50m and an anchor length of 13m. The chain length is constant and the elongation is calculated to 0.02 m with Equation (5-26) and the elongation of the wire is calculated with Equation (5-24).

Table 14-7: Stretching of installation wire.

Water depth	***Wire length****	***Calculated Wire Elongation***	***RIFLEX Wire Elongation*****	***Difference***
500	367	1.47	1.54	-0.07
1000	867	3.67	3.77	-0.10
1500	1367	6.09	6.16	-0.07
2000	1867	8.72	9.01	-0.29
2500	2367	11.58	11.8	-0.22
3000	2867	14.64	14.74	-0.10

* Un-stretched wire length (including release unit).

** Wire-end z-coordinate obtained from RIFLEX, minus un-stretched wire length. The wire is not pure vertical in RIFLEX.

It can be seen in Table 14-7 that the drop height is reduced by more than 10m if the stretch is not accounted for. For an optimized drop height, a lower height could result in insufficient seabed penetration and too low holding capacity. ROV inspection of the drop height is therefore necessary.

APPENDIX E Horizontal Variation of Mooring Line Top Node

The plotted section has the following coordinates (approximate values):

Upper end: z=-372m, Lower end z=-494m

X_{DIST} represents the horizontal distance between the top node of the wire and mooring line.

X_{DIST} = 50 m	***X_{DIST} = 170 m***
1 sec	
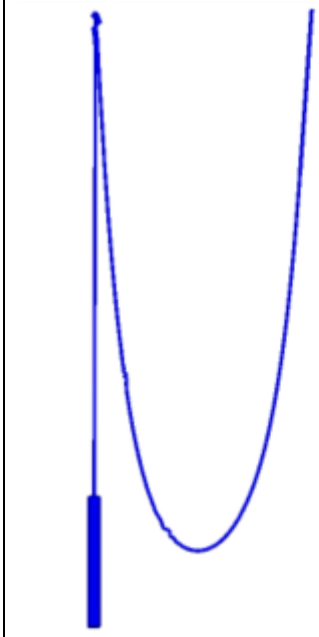	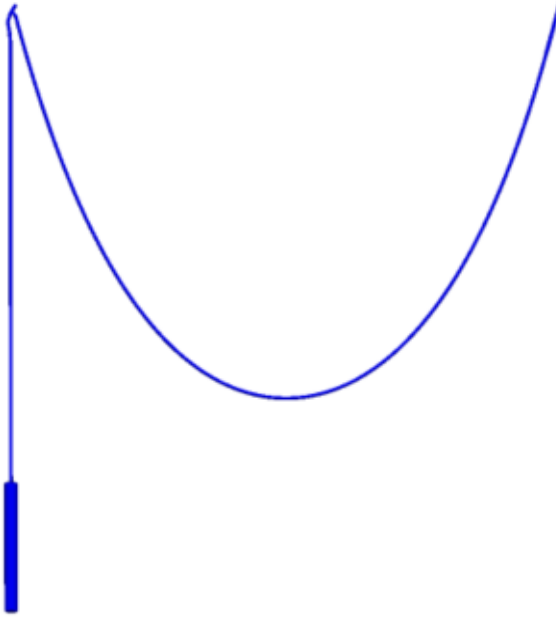
Sea bottom	

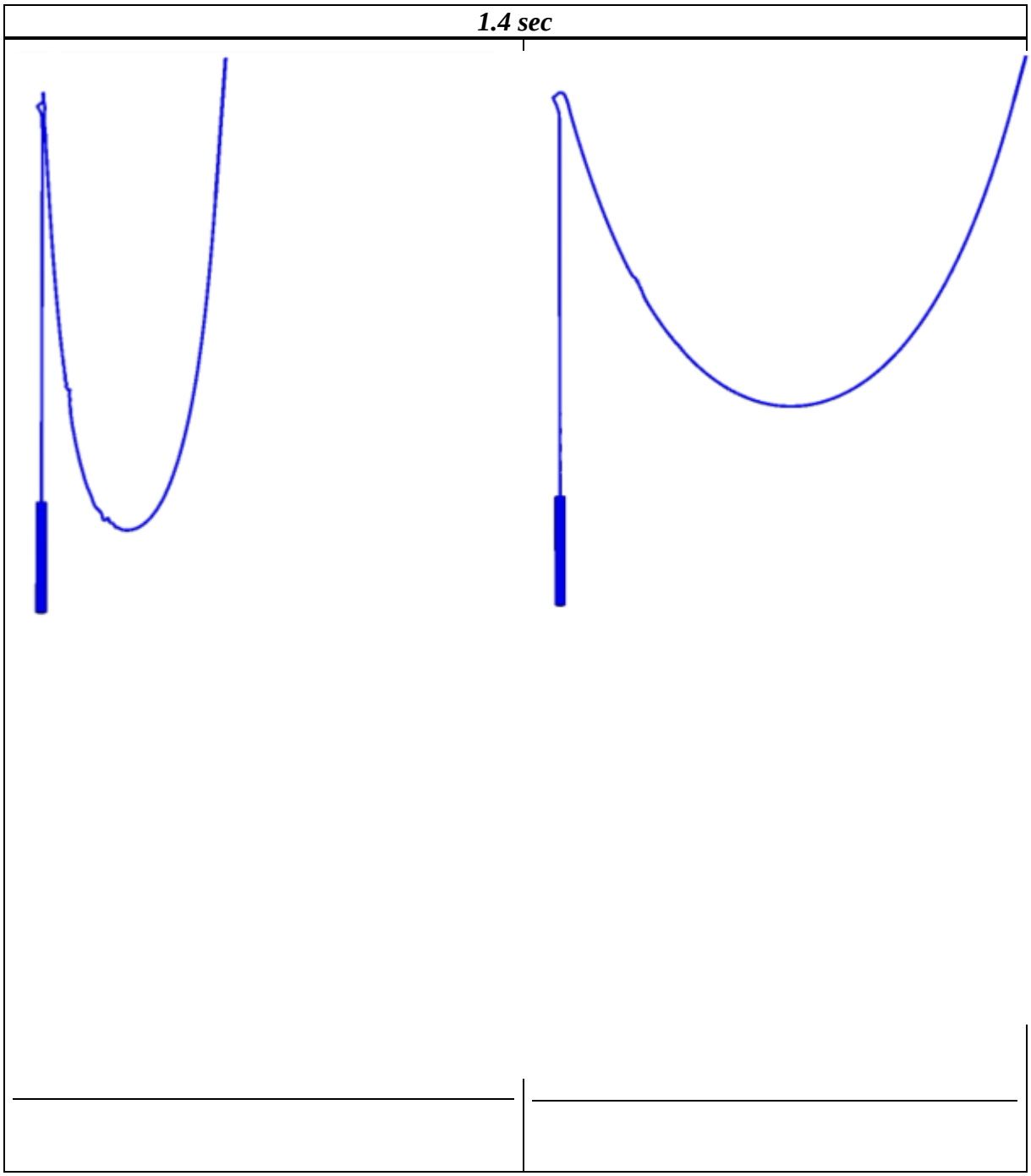
1.4 sec

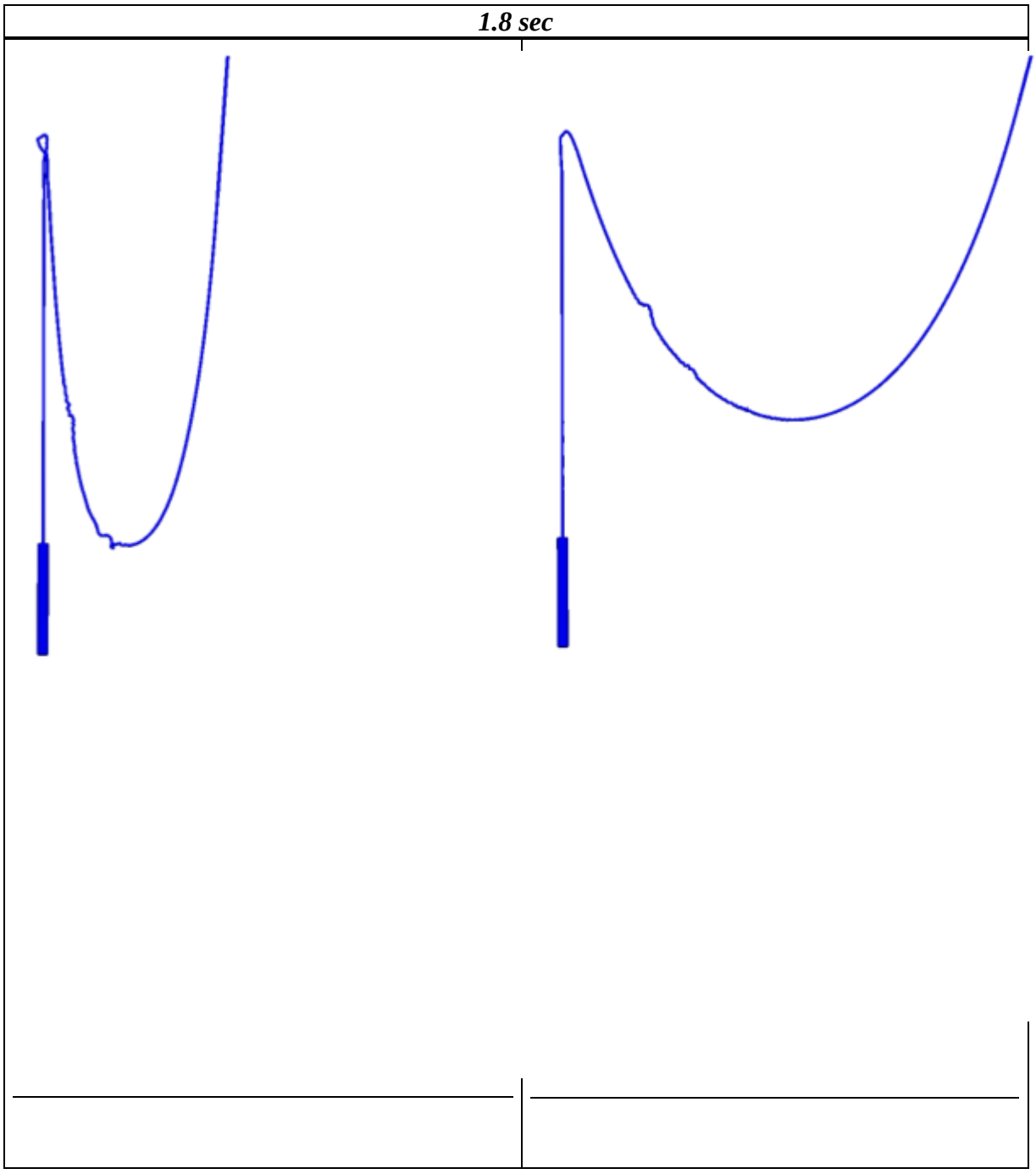
1.8 sec

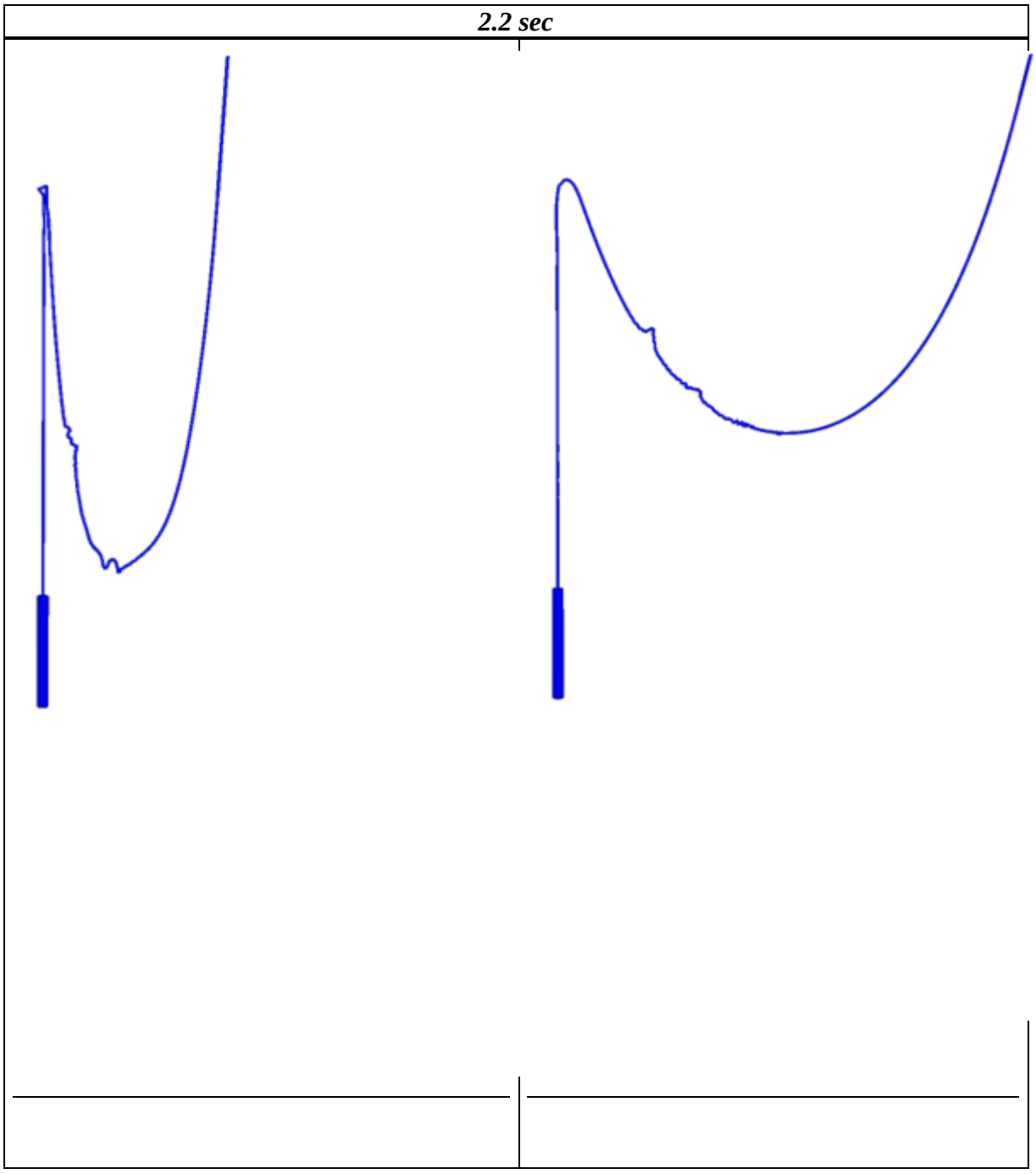
2.2 sec

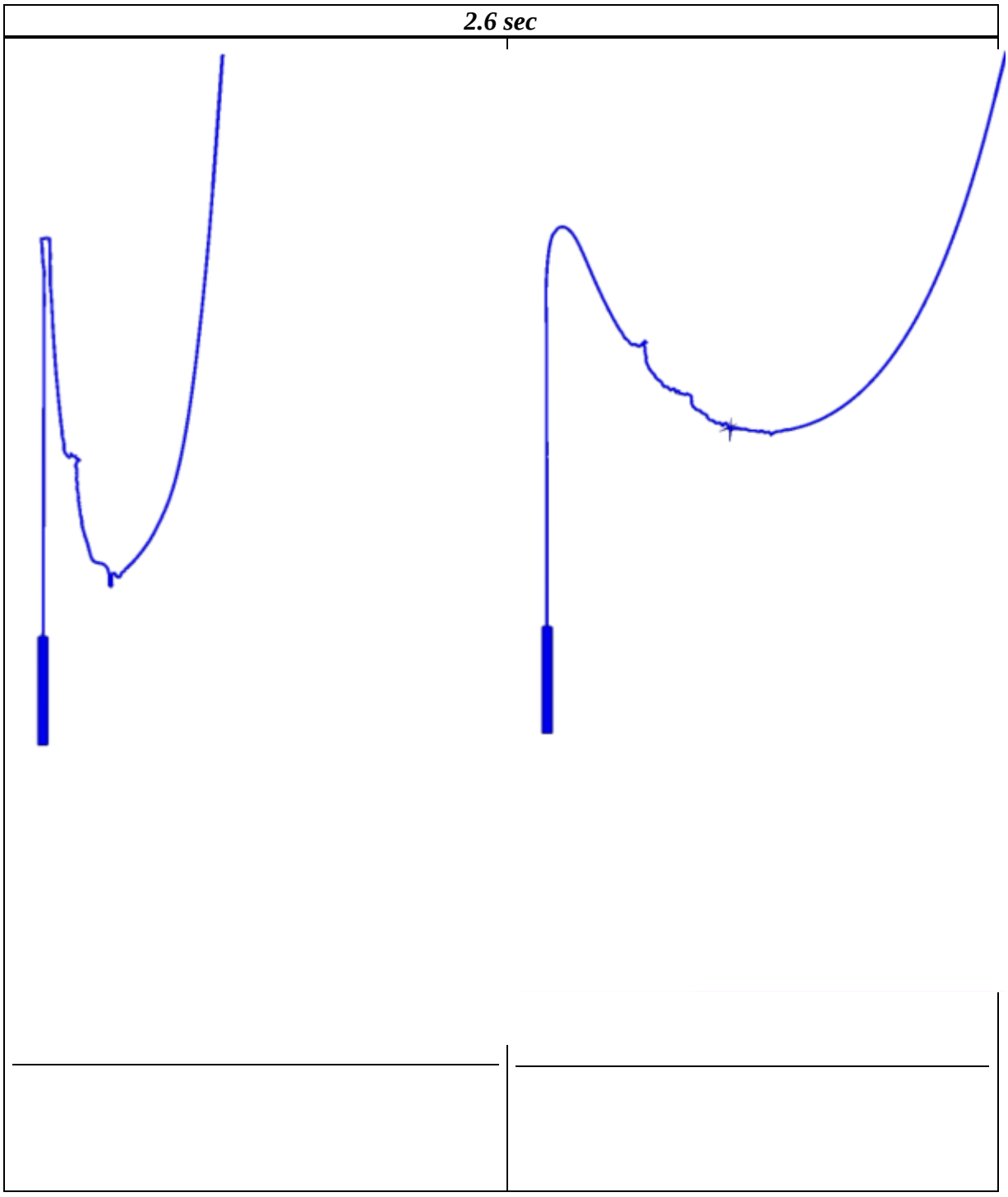
2.6 sec

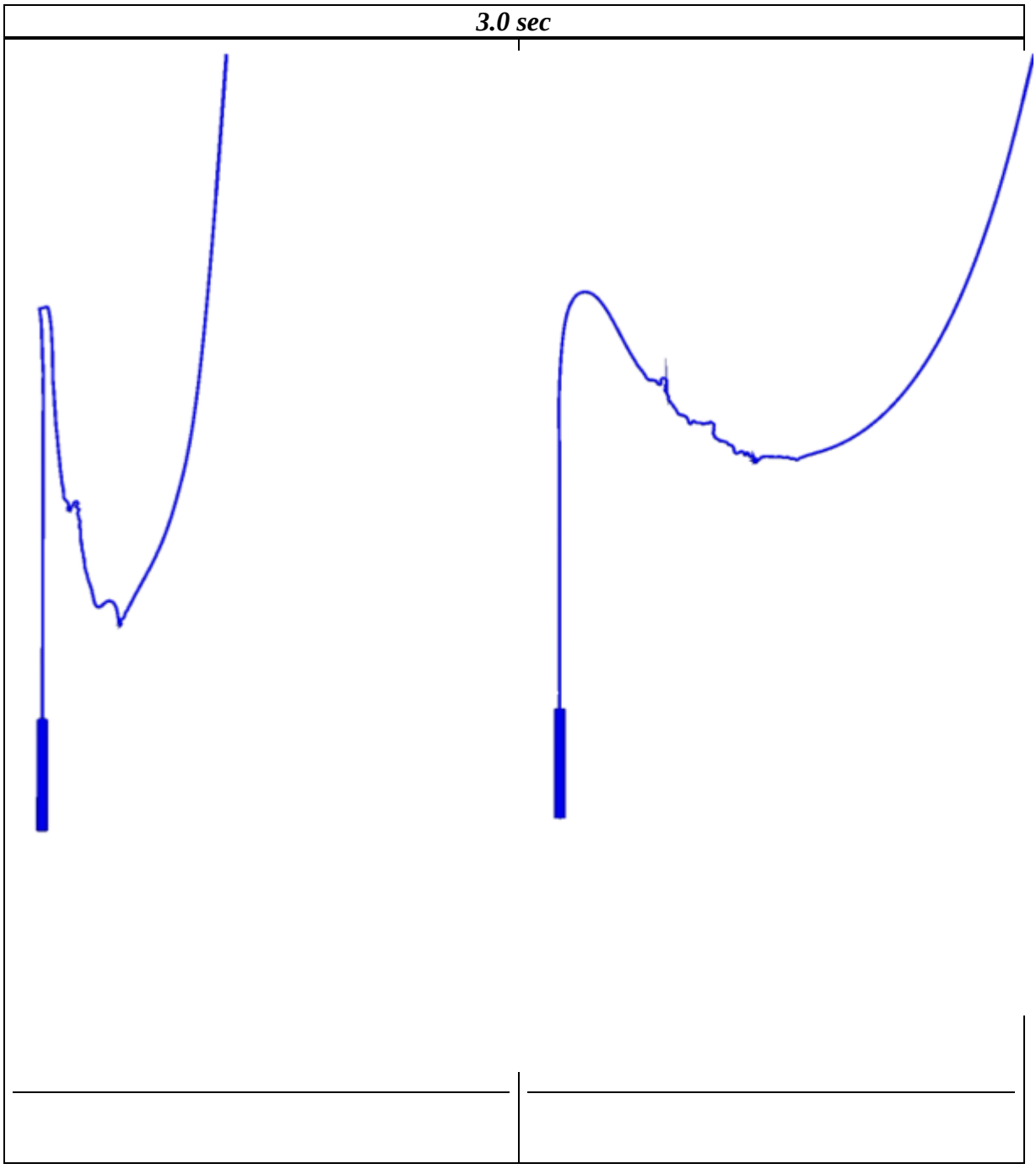
3.0 sec

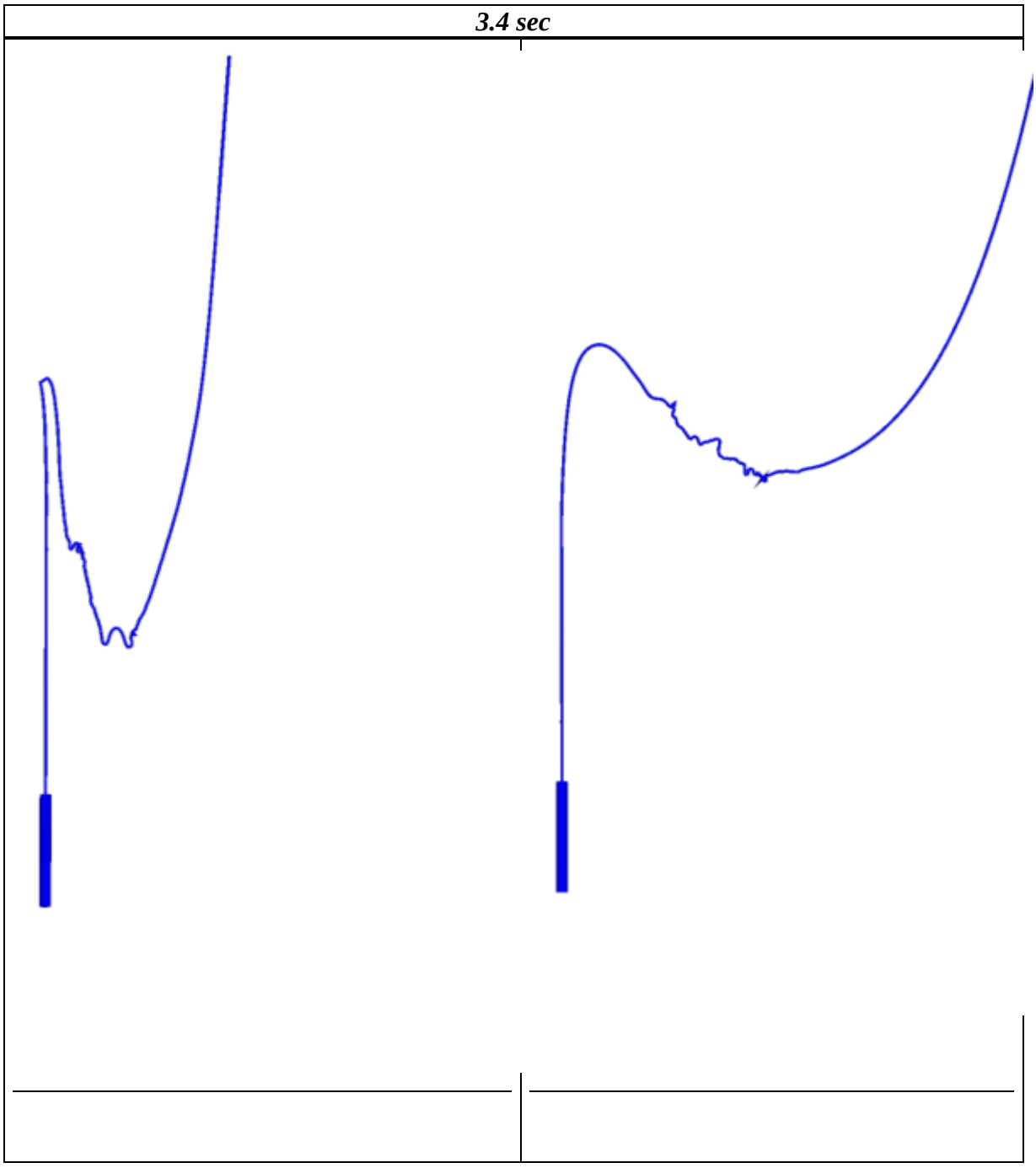
3.4 sec

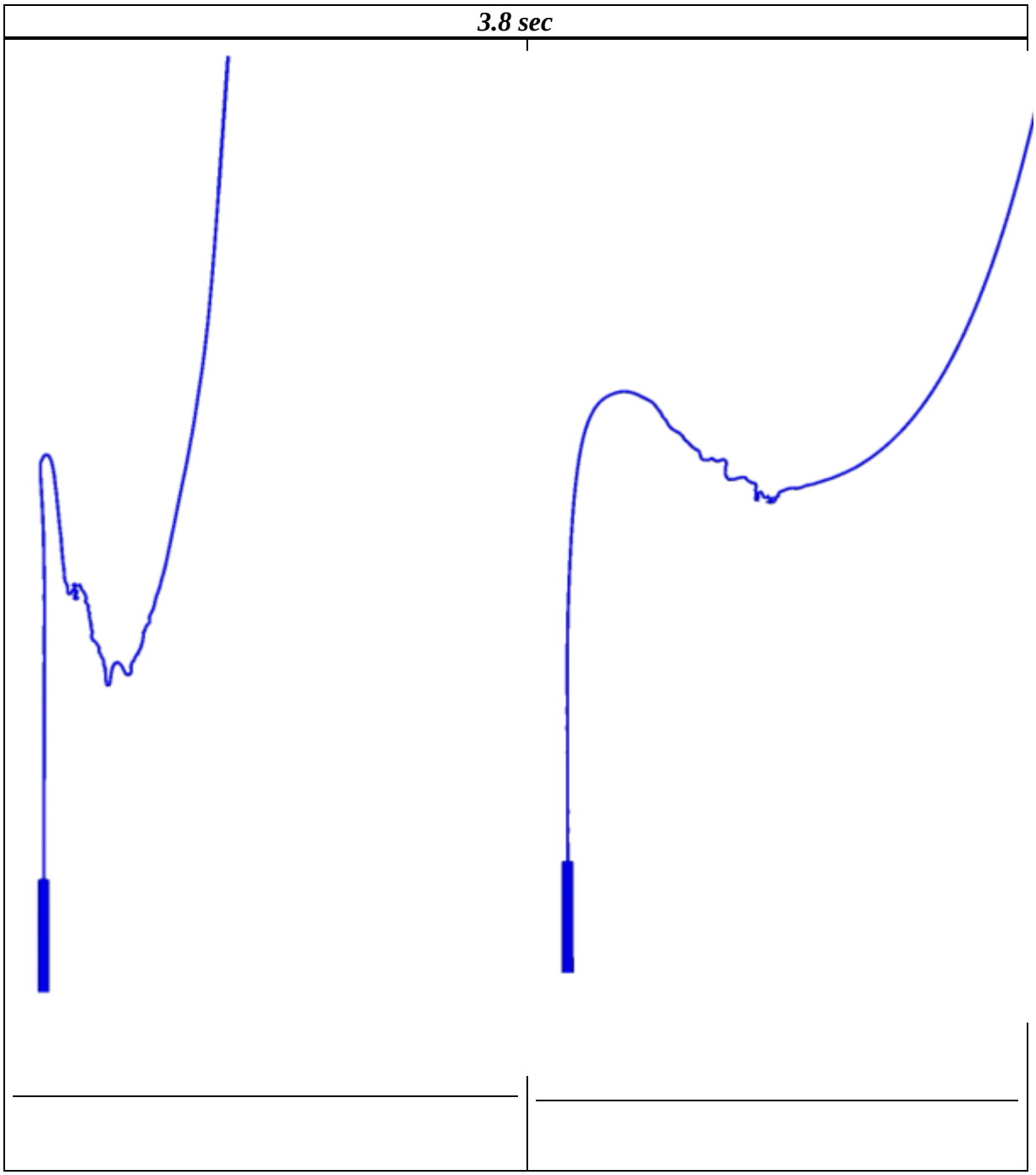
3.8 sec

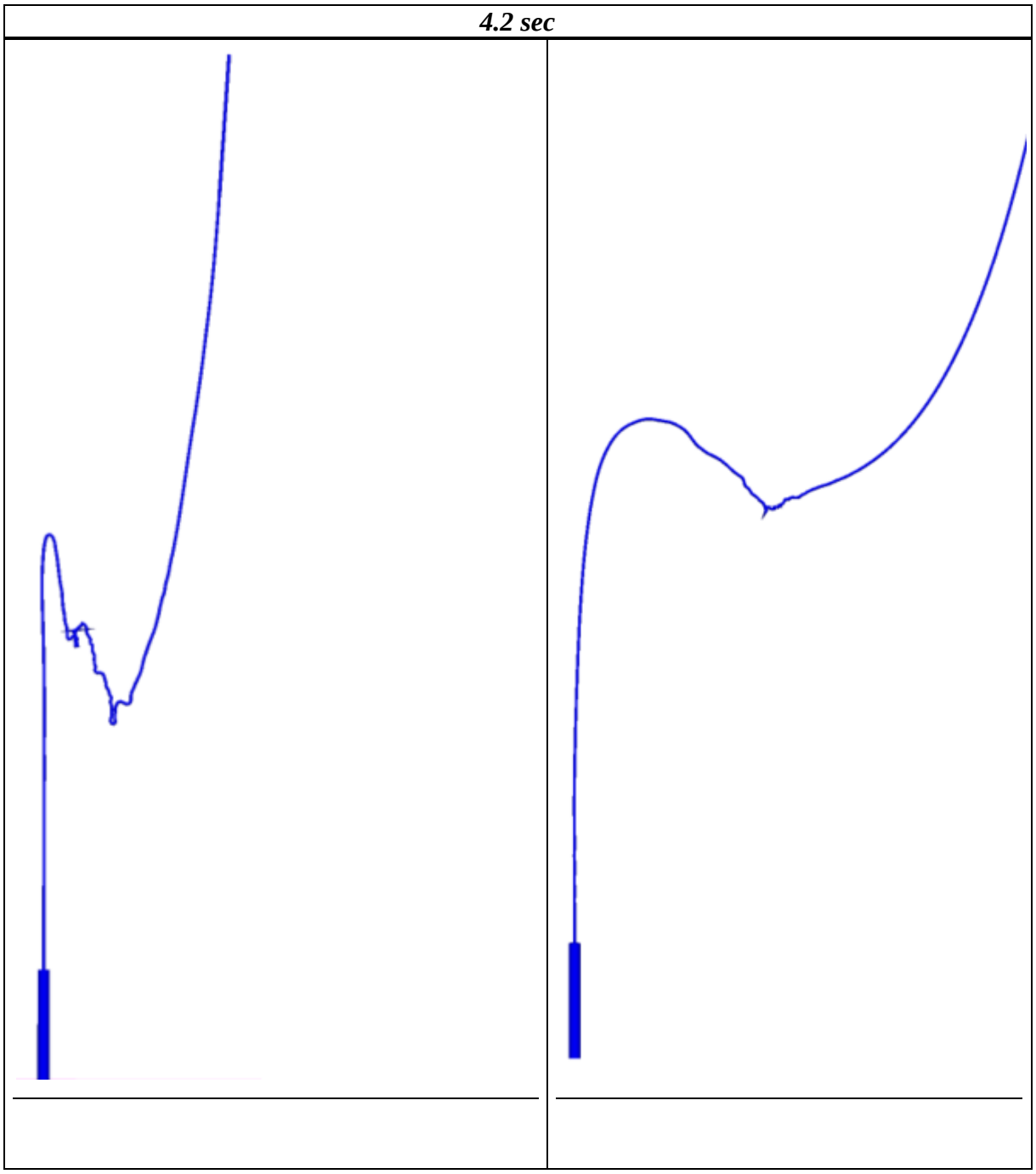

Figure 14-1: Snapshots during free fall for X_{DIST} equal to 50 and 170m (SIMA/RIFLEX, 2015)

APPENDIX F Bugs in SIMA 3.1.1

During the thesis work, some errors have been discovered in SIMA. This appendix presents these errors and a suggestion for improvement.

Error 1

In the dynamic analyses performed in this thesis, displacement response data for specific nodes are stored. Data that the user will store is selected in "*Calculation Parameters*" → "*Dynamic Calculation*". After running the static- and dynamic analysis, the displacement data and plots are obtained by clicking the following; *Conditions* → *Initial* → *Results* → *Dynamic* → *sima-noddis.bin*. A plot window opens, and the user can select different plots in the menu. By right-clicking in each plot, one should be able to copy the values that represent the curve. This is only possible for displacement in x- and y- direction. If the procedure is used for the z-direction, only one large unintelligible value comes out. This problem is passed on to Andreas Amundsen at MARINTEK.

Error 2

When results from more than one condition are calculated in a RIFLEX task, a bug occurs in the graphic window. In the top of the visualization window, there is a menu where the active condition is selected in the left corner, result type in the middle and a "video" of the system response can be shown by clicking the play button to the right. When the user click "Open 3D View", the "Initial" condition is defaulted in the menu. If the user wants to see the static results for another condition, he activates this condition in the upper, left corner. The play button is then inactive even though the correct condition is selected, the result type shows "Static" and the graphic window shows the stressfree state (modeled state). The user must click and choose "Static" result type again to activate the play button. This is bothersome. An example is given in Figure 15-1. It can be seen within the red circle that it not possible to click play and run the response visualization without selecting the condition one more time.

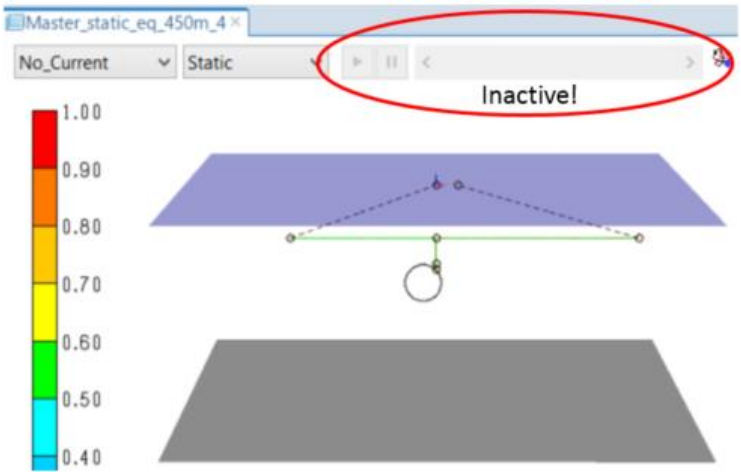

Figure 15-1: Bug in SIMA/RIFLEX. Error 2.

Suggestion for improvement

With regard to challenges met during the thesis work, a better zooming-tool would be appreciated. RIFLEX does not give the user the opportunity to decide the exact size and zoom of the visualization window. It should be possible to select or enter the following

- Front-, left- right- and bottom view
- Exact size of window
- Zoom (not only scroll-function, but enter values manually)
- View angle (enter values manually)

Without these options, simple tasks become time-consuming. If similar snapshots for several RIFLEX tasks are wanted, it becomes time-consuming to get similar views without the above-mentioned options. All snapshots presented in this thesis were difficult and time-consuming to create and only became approximately correct.